Analysis of upper tropospheric humidity measurements by microwave sounders and radiosondes

Vom Fachbereich für Physik und Elektrotechnik
der Universität Bremen
zur Erlangung des akademischen Grades eines
Doktor der Naturwissenschaften (Dr. rer. nat.)
genehmigte Dissertation

von
Viju Oommen John

April 2005

Berichte aus dem Institut für Umweltphysik – Band 27
herausgegeben von:

Dr. Georg Heygster
Universität Bremen, FB 1, Institut für Umweltphysik,
Postfach 33 04 40, D-28334 Bremen
URL http://www.iup.physik.uni-bremen.de
E-Mail iupsekr@uni-bremen.de

Die vorliegende Arbeit ist die inhaltlich unveränderte Fassung einer Dissertation, die im April 2005 dem Fachbereich Physik/Elektrotechnik der Universität Bremen vorgelegt und von Prof. Dr. Klaus Künzi sowie Prof. Dr. Justus Notholt begutachtet wurde. Das Promotionskolloquium fand am 30. Juni 2005 statt.

Bibliografische Information Der Deutschen Bibliothek
Die Deutsche Bibliothek verzeichnet diese Publikation in der Deutschen Nationalbibliografie; detaillierte bibliografische Daten sind im Internet über http://dnb.ddb.de abrufbar.

ISBN 3-8325-1010-9 ISSN 1615-6862

Logos Verlag Berlin
Comeniushof
Gubener Straße 47
D-10243 Berlin
Telefon (0 30) 42 85 10 90
URL http://www.logos-verlag.de

Layout: Lothar Meyer-Lerbs, Bremen

Contents

Abstract

This thesis describes results of several analyses of humidity measurements by microwave humidity sounders and radiosondes. The goal of this work is to pave the way for fully utilizing these measurements for climatological applications.

High resolution radiosonde data from the research vessel Polarstern are used to examine the variability of the clear-sky outgoing longwave radiation (OLR). The global variability (one standard deviation) of OLR is found to be $33\,\mathrm{W\,m^{-2}}$, of which a large part can be attributed to temperature variations. The variability after filtering the temperature part is associated with the humidity variability in the horizontal and the vertical. The impact of the vertical structures on the OLR calculations is also investigated in detail. It is observed that smoothed profiles in relative humidity are sufficient to obtain the mean value of OLR, even though the variability cannot be exactly reproduced.

Satellite sensors like HIRS and AMSU-B measure tropospheric humidity, but with low vertical resolution. It was decided to use the data from AMSU-B in this thesis because it operates in the microwave range so clouds have less impact on the data compared to the infrared HIRS data. A radiative transfer model, ARTS, is configured and validated to have it used as a tool for analyzing the satellite data. It is also demonstrated using ARTS calculations that the weak ozone lines in the AMSU-B frequency range have a non-negligible impact on the instrument's measurements, Channel 18 being the most affected.

AMSU-B Channel 18 brightness temperatures are sensitive to upper tropospheric humidity (UTH). A simple method is developed to transform the brightness temperatures to UTH. This method is validated with high quality radiosonde data. An initial attempt to make

a UTH climatology and the usefulness of a robust estimator such as the median in climatological studies are discussed.

Finally, a robust method was developed to compare the humidity measurements from satellite humidity sounders and radiosondes. The method is developed and tested using the high quality radiosonde data from the Lindenberg radiosonde station. A case study using different versions of the data shows that the method is sensitive to humidity differences in the different versions. The main result from the case study is that the corrected radiosonde data still have a slight dry bias in the upper troposphere. The method is then applied to assess the performance of different radiosonde sensors and stations. It is found to be useful for monitoring the global radiosonde network, using the microwave satellite data as a benchmark.

Publications

The work described in this thesis has given rise to a number of publications, all of which can be downloaded from http://www.sat.uni-bremen.de/publications/.

Journal Articles

Published

1. The results of the development of a satellite-radiosonde humidity comparison method and a case study using the Lindenberg radiosonde data are published in the following paper. The first half of Chapter 5 is based on this article.

   Buehler, S. A., M. Kuvatov, V. O. John, U. Leiterer and H. Dier (2004), **Comparison of microwave satellite humidity data and radiosonde profiles: A case study**, *J. Geophys. Res.*, 109, D13103, doi:10.1029/2004JD004605.

2. The following paper describes the impact of the weak Ozone lines on AMSU-B radiances. This paper also discusses the effect of the exclusion of Ozone and stratosphere in satellite–radiosonde humidity comparisons. The last section of Chapter 3 and a small section of Chapter 5 are from this paper.

   John, V. O. and S. A. Buehler (2004), **The impact of ozone lines on AMSU-B radiances**, *Geophys. Res. Lett.*, 31, L21108, doi:10.1029/2004GL021214.

3. The results of the brightness temperature transformation method (transforming T_B^{18} to UTH) is published in the following paper. Chapter 4 is mainly from this article.

   Buehler, S. A. and V. O. John (2005), **A simple method to relate microwave radiances to upper tropospheric humidity**, *J. Geophys. Res.*, 110, D02110, doi:10.1029/2004JD005111.

4. The results of a study to investigate the retrieval precision of UTH from AMSU data are published in the following article.

   Jimenez, C., P. Eriksson, V. O. John and S. A. Buehler (2005), **A practical demonstration on AMSU retrieval precision for upper tropospheric humidity by a non-linear multi-channel regression method**, *Atmos. Chem. Phys.*, 5, 451-459, SRef-ID:1680-7324/acp/2005-5-451.

5. The clear-sky version of ARTS model was intercompared with several radiative transfer models. The results are published in the following paper. A separate section of the paper is dedicated to the simulations of the AMSU-B instrument, these calculations are based on the setup described in Chapter 3.

   Melsheimer C., C. Verdes, S. A. Buehler, C. Emde, P. Eriksson, D. G. Feist, S. Ichizawa, V. O. John, Y. Kasai, G. Kopp, N. Koulev, T. Kuhn, O. Lemke, S. Ochiai, F. Schreier, T. R. Sreerekha, M. Suzuki, C. Takahashi, S. Tsujimaru and J. Urban, (2005), **Intercomparison of general purpose clear sky atmospheric radiative transfer models for the millimeter/submillimeter spectral range**, *Radio Sci.*, RS1007, doi:10.1029/2004RS003110.

6. A detailed discussion of the application of the satellite-radiosonde humidity comparison method to assess the performance of different radiosonde stations over Europe is described in the following paper. The second half of Chapter 5 is based on this article.

   John, V. O. and S. A. Buehler (2005), **Comparison of microwave satellite humidity data and radiosonde profiles: A survey of European stations**, *Atmos. Chem. Phys.*, 5, 1843–1853, SRef-ID:1680-7324/acp/2005-5-1843.

7. A detailed description of the retrieval of upper tropospheric humidity and upper tropospheric water vapor can be found in:

   Houshangpour, A., V. O. John and S. A. Buehler (2005), **Retrieval of upper tropospheric water vapor and upper tropospheric humidity from AMSU radiances**, *Atmos. Chem. Phys.*, 5, 2019–2028, SRef-ID:1680-7324/acp/2005-5-2019.

8. A cautionary note on the assumption of Gaussian statistics in the development of UTH climatology is discussed In the following article. The last part of Chapter 4 is based on this article.

   John, V. O., S. A. Buehler and N. Courcoux (2005), **A cautionary note on the use of Gaussian statistics in satellite based UTH climatologies**, *IEEE Geosci. Remote Sens. Lett.*, in press.

Under Revision or Submitted

9. A description of the variability of the clear-sky OLR can be found in the following manuscript. Chapter 2 is mostly based on this manuscript.

   Buehler, S. A., V. O. John, A. von Engeln, E. Brocard, T. Kuhn and P. Eriksson (Submitted 2005), **Understanding the global variability of clear-sky outgoing longwave radiation**, *Q. J. R. Meteorol. Soc.*.

10. A detailed discussion on the the modeling OLR using ARTS can be found in

    Buehler, S. A., A. von Engeln, E. Brocard, V. O. John, T. Kuhn and P. Eriksson (Submitted 2005), **Recent developments in the line-by-line modeling of outgoing longwave radiation**, *J. Quant. Spectrosc. Radiat. Transfer*.

11. Asymmetry of AMSU-B scanning and its time evolution are discussed in:

    Buehler, S. A., M. Kuvatov, and V. O. John (Submitted 2005) **Scan asymmetries in AMSU-B data**, *Geophys. Res. Lett.*.

12. The fast radiative transfer model RTTOV-7 is compared against ARTS for AMSU-B simulations and the results of spatial biases found in the comparison are described in the following manuscript.

    Buehler, S. A., N. Courcoux, and V. O. John (Submitted 2005) **Spatial biases in fast radiative transfer calculations for a passive microwave satellite sensor**, *J. Geophys. Res.*.

Technical Reports

13. The modeling of OLR and its variability was done as part of an ESA study. A very detailed description of the work can be found in the following technical report.

    von Engeln, Axel, E. Brocard, S. A. Buehler, P. Eriksson, V. O. John and T. Kuhn (2004), **ACE+ Climate Impact Study: Radiation Part**, Final Report, ESTEC *Contract No 17479/03/NL/FF*.

14. A summary of the aforesaid ESA study report is the following report.

    von Engeln, Axel, E. Brocard, S. A. Buehler, P. Eriksson, V. O. John and T. Kuhn (2004), **ACE+ Climate Impact Study: Radiation Part**, Executive Summary, ESTEC *Contract No 17479/03/NL/FF*.

Articles in Conference Proceedings

15. Preliminary results of the brightness temperature transformation method are given in:

    John, V. O. and S. A. Buehler (2004), **Scaling of microwave radiances to layer averaged relative humidity**, IASTA *Bulletin*, 16, 293–296.

16. Preliminary results of the humidity comparison method and comparison of different sensors are shown in:

    John, V. O., S. A. Buehler and M. Kuvatov (2003), **Comparison of AMSU-B brightness temperature with simulated brightness temperature using global radiosonde data**, In: *Thir-*

teenth International TOVS *Study Conference (*ITSC*–XIII)*, St. Adele, Montreal, Canada.

17. A discussion on the configuration of ARTS for the use of simulating AMSU radiances and its validation by comparing against a reference model is given in:

    John, V. O., M. Kuvatov and S. A. Buehler (2002), **ARTS - A new radiative transfer model for AMSU**, In: *Twelfth International* TOVS *Study Conference (*ITSC*–XII)*, Lorne, Australia, February 2002.

1 Introduction

Water makes the Earth unique. Life exists as it does because gaseous, liquid and solid phases of water can co-exist on the planet (SPARC, 2000). For instance, water vapor is the most abundant and the most radiatively important greenhouse gas in the Earth's atmosphere, keeping our planet's surface temperature above the freezing level. Unlike other greenhouse gases like CO_2, water vapor is distributed unevenly over the globe. The precipitable water, which is the height integrated water vapor content (or in other words if all the water vapor in the air were condensed and fell as rain), is about 50 mm near the equator and less than one-tenth as much near the poles (Seidel, 2002). The uneven distribution of water vapor is even more pronounced in the vertical. The volume mixing ratio of water vapor, which is the ratio of water vapor partial pressure to the total pressure of the air, decreases rapidly with height, varying over four orders of magnitude, from a few percent near the surface to a few parts per million in the lower stratosphere. About half of the water vapor in the air resides below an altitude of 1.5 km, less than 5% in the upper troposphere, and less than 1% in the stratosphere. This wide range of concentrations presents challenges in designing instruments for atmospheric water vapor measurements (Seidel, 2002). Thus, a large variety of technologies exist, from balloon borne measurements to satellite based measurements.

The Earth's internal sources of energy are small compared to the energy provided by the Sun. The climate system is therefore in equilibrium when the solar energy absorbed by the Earth is balanced by the thermal infrared energy emitted to space by the Earth. The infrared radiation emitted to space by the Earth is often referred to as the outgoing longwave radiation (OLR). Any change in the amount of water vapor changes the emission of the OLR. An increase in water

vapor decreases the OLR and a decrease in the water vapor increases the OLR. The variability of the clear-sky OLR depends mainly on two parameters, the surface temperature and the amount of water vapor. At high latitudes, the changes in OLR are mostly coupled with the variations in the surface temperature, whereas in the tropics, the changes are mostly coupled with changes in water vapor. An increase in water vapor reduces the OLR only if it occurs at an altitude where the temperature is less than the surface temperature. The impact of water vapor on the OLR increases sharply as the temperature difference increases.

Recently, studies by Chen et al. (2002) and Wielicki et al. (2002) reported surprisingly large decadal variations in the energy budgets of the tropics. Over the period 1985–2000, thermal radiation emitted by the Earth to space increased by more than $5\,\mathrm{W\,m^{-2}}$, while reflected sun light decreased by less than $2\,\mathrm{W\,m^{-2}}$. Yet only very small changes in the average tropical surface temperature were observed during this time period. Although the causes remain unclear, the changes are thought to be due to a decadal-time-scale strengthening of the tropical Hadley and Walker circulations, that is, a redistribution of water vapor and clouds. Equatorial convective regions have intensified in upward motion and moistened, while both the equatorial and subtropical subsidence regions have become drier and less cloudy (Hartmann, 2002; Chen et al., 2002).

As discussed above, any increase in the amount of a greenhouse gas would reduce the OLR, if the temperature of the atmosphere and the surface are held fixed. Then, the climate achieves a new equilibrium by warming until the OLR increases enough to re-establish the balance, thus, leading to the so called global warming. Determination of the new balance is complicated by the fact that water vapor is itself a greenhouse gas, and the amount and the distribution of water vapor changes as the climate changes. The atmospheric water vapor content responds to changes in temperature, micro-physical processes, and the atmospheric circulation (Stocker et al., 2001). The saturation water vapor pressure increases rapidly with temperature, in accordance with the Clausius-Clapeyron relation. Thus, warming the atmosphere by increasing anthropogenic greenhouse gases such as the CO_2 would cause

absolute water vapor concentration to increase with the assumption that the relative humidity remains the same, which would further increase the greenhouse effect, amplifying the initial warming. This is referred to as the positive water vapor feedback in climate studies.

The issue of water vapor feedback has been subjected to a long term debate. A very detailed discussion of this issue can be seen in a review article by Held and Soden (2000) and also in Stocker et al. (2001). The argument of a positive feedback started more than one hundred years ago (Arrhenius, 1896; Chamberlin, 1899). Results from the calculations of a radiative-convective model with a constant relative humidity suggested that the exponential increase of absolute humidity due to the surface temperature increase would exert a strong positive feedback (Manabe and Wetherald, 1967). The positive feedback is one of the main causes of the large warming predicted by general circulation models in response to a doubling of CO_2. The water vapor feedback approximately doubles the warming from what it would be for a fixed water vapor (Held and Soden, 2000). However, other scientists have argued a negative feedback on the basis that an increase in the strength of convection in the tropics could lead to drying rather than a moistening of the upper troposphere (Ellsaesser, 1984; Lindzen, 1990).

Soden et al. (2002) investigated the observed water vapor response to a global climate change due to the eruption of Mt. Pinatubo. In a comparison of observations with simulations of a general circulation model, they found that the time series of globally averaged total column water vapor and the upper tropospheric water vapor were well simulated by the model when the water vapor feedback was included. A version of their model that excluded water vapor changes in the radiative calculation underestimated the tropospheric temperature changes, whereas the full model was able to reproduce the observed temperature changes. An examination of the sensitivity of water vapor in the tropical upper troposphere to changes in surface temperature by Minschwaner and Dessler (2004) showed that as the surface warms, changes in the vertical distribution and temperature of detraining air from tropical convection lead to higher water vapor mixing ratios in the upper troposphere. However, their calculation suggested that this

increase in mixing ratio is not as large as to keep the relative humidity constant and therefore maintaining a fixed relative humidity above 250 hPa may overestimate the contribution made by these levels to the water vapor feedback. Although the argument of a positive water vapor feedback has an upper hand in the issue, uncertainties prevail due to the unavailability of good long-term measurements of water vapor (Forster and Collins, 2004). Moreover, all these studies highlight the importance of upper tropospheric humidity which plays a vital role in the water vapor feedback.

Measurements of upper tropospheric water vapor are mainly from two sources: (1) global radiosonde data and (2) geostationary and polar-orbiting satellite data. Radiosondes have been measuring the Earth's atmosphere for more than half a century, thus, providing the longest available data set of water vapor in the upper troposphere. Another good point about radiosonde data is that they have high vertical resolution, therefore the data are rich with vertical structures in the water vapor profile. Unfortunately, there are also several demerits associated with the radiosonde data. The first one is that the radiosonde network is limited only to the land areas and most stations are found in the northern hemisphere. This introduces the so called land bias in the radiosonde data set. Secondly, the large dynamic range needed for an instrument to measure water vapor concentrations, varying four or five orders of magnitude throughout the sounding, makes the humidity measurements difficult. For this reason, the quality of humidity data from radiosondes is generally found to be decreasing with decreasing water vapor content, temperature, and pressure (Elliot and Gaffen, 1991; SPARC, 2000). The third reason is that the radiosonde stations across the world use a large variety of humidity sensors. This introduces spatial inhomogeneities in the global data record. Moreover, instrument or methodology changes at any particular station introduce a temporal inhomogeneity in the data record. The simultaneous use of different radiosonde types within the global network has led to differences in upper tropospheric humidity across geopolitical boundaries (Soden and Lanzante, 1996). Also, for long-term climate studies, changes in radiosonde instrumentation and methods can introduce spurious signals in the data record (Ross and Gaffen, 1998;

SPARC, 2000). However, there are a lot of efforts in correcting and homogenizing the radiosonde humidity record in order to properly utilize the wealth of global radiosonde data (Wang et al., 2002; Lesht and Richardson, 2002; Leiterer et al., 1997). Satellite based methods for monitoring the radiosonde network are also found to be useful in identifying the changes in instrumentation or method (Soden and Lanzante, 1996) and also in correcting the data (Soden et al., 2004).

Satellite measurements of upper tropospheric water vapor come mainly from two sources: (1) infrared measurements in the 6.3 μm water vapor absorption band and (2) microwave measurements in the 183.31 GHz water vapor line. The infrared channels are the GOES 6.7 μm channel and the METEOSAT 6.3 μm channel on geostationary satellites and the HIRS 6.7 μm channel on the polar-orbiting satellites. These channels are sensitive primarily to vertically averaged water vapor over a depth of a few hundred hPa, centered in the upper troposphere. A simple method exists to transform these measurements to upper tropospheric humidity (UTH), which is the Jacobian weighted relative humidity in the upper troposphere (Soden and Bretherton, 1993, 1996). As the temporal coverage of geostationary measurements is good, UTH data from GOES and METEOSAT have been used, for example, to study the evolution of UTH associated with convective activities (Soden, 1998, 2004; Tian et al., 2004). As HIRS instruments are in orbit since 1978, there has been a long term global data record from these sensors. This allows one to study the average state, the variability, and the trend of upper tropospheric water vapor. Bates et al. (2001) investigated the variability of UTH using the long term record from HIRS measurements and found large variability in the tropical UTH which is hypothesized due to Rossby wave activities. A trend analysis by Bates and Jackson (2001) using HIRS measurements of 20 years found that decadal trends are strongly positive in the deep tropics, negative in the southern hemisphere subtropics and mid-latitudes, and of mixed sign in the northern hemisphere subtropics and mid-latitudes. The UTH data derived from GOES and HIRS have also been used for the evaluation of upper tropospheric moisture in general circulation models (Spangenberg et al., 1997; Allan et al., 2003). However, clouds are opaque to infrared radiation. Therefore

these data cannot be used in the presence of clouds. There exists a clear-sky bias in the UTH data sets derived from infrared measurements (Lanzante and Gahrs, 2000).

Microwave measurements of UTH are mainly from two instruments: SSM/T2 and AMSU-B on-board polar-orbiting satellites. The channel at 183.31 ± 1.00 GHz on these instruments is similar to the 6.7 μm channel and sensitive to the upper troposphere. Since microwave radiation can penetrate most of the clouds except strong convective clouds and thick cirrus clouds, UTH data derived from microwave measurements should be almost free of sampling biases. AMSU-B data have so far been mainly used to be assimilated into numerical weather prediction models, but not much used for deriving UTH. The work described in this thesis is an attempt to fully utilize these data for climate applications.

The thesis is organized into five chapters. Chapter 2 investigates the variability and the dependence of clear-sky OLR. The impact of vertical structures of humidity profiles on the OLR calculations is also examined. Chapter 3 introduces the radiative transfer theory, the radiative transfer model, ARTS, which is used as a tool for the analysis of satellite and radiosonde data, and the AMSU-B instrument. The configuration and validation of ARTS for AMSU-B is also discussed. Furthermore, the impact of weak ozone lines in the AMSU-B frequency range on the measurements is examined. Chapter 4 discusses a simple method to transform the AMSU-B measurements to UTH. A discussion of an initial attempt to create a UTH climatology is also given. Chapter 5 describes the development, a case study, and the application of a method to compare humidity measurements from microwave sounders and radiosondes. Finally, Chapter 6 presents the overall summary, conclusions, and some points for future work.

2 The Variability of Clear-Sky Outgoing Longwave Radiation

The Earth and its atmosphere absorb the shortwave (SW) radiation coming from the sun and emit the thermal longwave (LW) radiation to space. These two radiation streams can be represented approximately by blackbody radiation of 6000 K for the solar SW and 290 K for the terrestrial LW. The balance between the incoming SW radiation and the outgoing LW radiation (OLR) determines the temperature of the atmosphere and of the Earth's surface (Salby, 1996; Harries, 1996, 1997).

The OLR originates partly from the surface but to a significant part from higher levels of the atmosphere. Because of the lower temperature at these levels, the OLR is reduced compared to a hypothetical Earth without atmosphere. Figure 2.1 shows a high resolution radiative transfer model simulation of clear-sky monochromatic radiance at the top of the atmosphere (TOA), which illustrates this. Besides the calculated spectrum, it shows Planck curves for different temperatures. An integration over all frequencies and directions yields the OLR. The reduction of OLR compared to a hypothetical Earth without a atmosphere is of course nothing else than the atmospheric 'greenhouse' effect. From the known incoming solar SW radiation we can easily infer the global average OLR to be close to 240 $\mathrm{W\,m^{-2}}$, because the incoming and outgoing radiation fluxes must balance (Harries, 1996). However, there is considerable variability for different latitudes and weather conditions, so the local OLR values vary between about 160 $\mathrm{W\,m^{-2}}$ and 320 $\mathrm{W\,m^{-2}}$. Allan et al. (1999) showed that the clear-sky OLR variability is mostly due to temperature variability at high latitudes and due to humidity variability at low latitudes. Clouds also

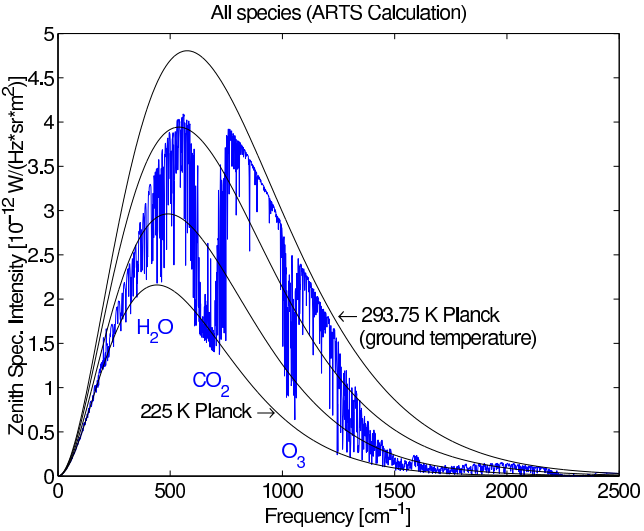

Figure 2.1: A radiative transfer model simulation of the TOA zenith monochromatic radiance for a mid-latitude summer atmosphere. Smooth solid lines indicate Planck curves for different temperatures: 225 K, 250 K, 275 K, and 293.75 K. The latter was the assumed surface temperature. The calculated quantity has to be integrated over frequency and direction to obtain the total OLR. Note that in this chapter, the frequencies are expressed in the wavenumber units (cm^{-1}) because it is the conventional unit of frequency in the thermal infrared range. (Figure adapted from von Engeln et al. (2004b))

have an important impact on OLR, but this study focuses only on the clear-sky case.

The considerable interest in the sensitivity of OLR to humidity variations at different altitudes is mainly due to the debate about the humidity feedback in the climate system that was started by Lindzen (1990). A very good overview on this debate is given by Held and Soden (2000). The broad consensus now seems to be that the feedback is indeed positive, not negative as conjectured by Lindzen (see for example Shine and Sinha (1991), Sinha and Allen (1994), Colman (2001), and Minschwaner and Dessler (2004)). However, the exact magnitude of the feedback is still somewhat uncertain, not the least because of our

insufficient knowledge of the absolute amount of upper tropospheric humidity, due to the limitations of the current global observing system. For example, there are large differences between the humidity measured by radiosondes and by infrared sensors as documented by Soden and Lanzante (1996) and Soden et al. (2004). Another limitation is that typical atmospheric humidity profiles are rich in vertical structure, as documented by radiosondes, while current remote sensing methods usually yield only vertically smoothed measurements with a smoothing height of 2.5 to 6.0 km, depending on the technique.

The present study had two main objectives. The first objective was to understand the day-to-day variability of clear-sky OLR and its dependence on variations in atmospheric temperature and humidity. The second objective was to assess the impact of vertical structure in the humidity field on OLR, and to assess to what extent humidity measurements with coarse vertical resolution can be used to predict OLR. It has to be pointed out that understanding the day-to-day variability of OLR is not sufficient to predict its response to a large scale forcing, such as a CO_2 increase. A better strategy for that application is to look at the impact of other large scale forcings, for example, a large volcano eruption, as done by Soden et al. (2002). However, understanding the day-to-day variability can give important insights on the relevant factors controlling OLR and can help to identify deficiencies in our observational capabilities. Most of the results presented in this chapter are described in Buehler et al. (2005a,c); von Engeln et al. (2004a,b).

The chapter is organized as follows: Section 2.1 presents the modeling background and the model setup, including the atmospheric scenarios investigated, Section 2.2 presents results and discussion, and Section 2.3 gives summary and conclusions.

2.1 Modeling of OLR

2.1.1 A Retrospect

Climate models contain fast approximate models for calculating OLR. However, in order to directly assess the strength of the forcing or feedback of different gases under different atmospheric conditions, a preferred approach is to make high resolution radiative transfer (RT) calculations with a precise line-by-line radiative transfer model. This was first done by Shine and Sinha (1991), using a model with $10\,\mathrm{cm}^{-1}$ frequency resolution (note that in this chapter, the frequencies are expressed in the wavenumber units (cm^{-1}) because it is the conventional unit of frequency in the thermal infrared range), corresponding to 250 frequency grid points from 0 to $2500\,\mathrm{cm}^{-1}$. These calculations were considerably refined, firstly by Ridgway et al. (1991), then by Clough et al. (1992) and Clough and Iacomo (1995), who used an adaptive frequency grid to achieve 0.2% computational accuracy. Such high resolution calculations can be used to study the sensitivity of the OLR in different frequency regions to perturbations in the humidity concentration at different altitudes. A broad band of sensitivity to water vapor perturbations is observed throughout the thermal infrared, interrupted only by the CO_2 feature near $650\,\mathrm{cm}^{-1}$ (von Engeln et al., 2004b).

The calculations by Clough and coworkers included a better model of the water vapor continuum than earlier calculations. Due to the continuum, water vapor has a significant effect on OLR not only in the pure rotational band from approximately 0 to $600\,\mathrm{cm}^{-1}$ and the vibrational-rotational band from approximately 1400 to $2100\,\mathrm{cm}^{-1}$, but also in the continuum region between the bands (von Engeln et al., 2004b). These different frequency regions of water vapor absorption are responsible for OLR sensitivity to water vapor perturbations at different altitudes, a fact first pointed out by Sinha and Harries (1995), who particularly stressed the importance of the 0 to $500\,\mathrm{cm}^{-1}$ frequency region, where OLR is sensitive to perturbations in the middle and upper troposphere.

2.1.2 Basic Assumptions and Considered Species

For this study, detailed line-by-line radiative transfer calculations were performed with the Atmospheric Radiative Transfer Simulator (ARTS), described in Buehler et al. (2005b). More details of ARTS can be seen in Chapter 3. The model assumes a realistic spherical geometry for the atmosphere, which is an important difference to older models which assume a plane parallel atmosphere. A mathematical derivation of the flux calculation is given in Section 2.1.3.

The considered spectral range is from 0 to 2500 cm^{-1}, similar to Clough and Iacomo (1995). The most important radiatively active species in this spectral region are water vapor, carbon dioxide, methane, nitrous oxide, and ozone, with water vapor being by far the most important one. In addition to the line spectra, various continua have to be taken into account. Only the clear-sky case was considered. Clouds are known to have a very important impact on both the SW and the LW radiation, but, as stated above, are not taken into account in this study. The surface emissivity was set to unity, following Clough et al. (1992). This should be a good approximation at infrared frequencies. The top of the atmosphere was assumed to be at 100 hPa where nothing else is stated.

As described in Buehler et al. (2005b) the radiative transfer model ARTS can use different spectroscopic databases, for example, HITRAN (Rothman et al., 2003) and JPL (Pickett et al., 1992). For this study HITRAN was used. It lists about 1 million lines for 38 species between 0 and 2500 cm^{-1}. For the calculations presented here, a reduced species list of only H_2O, CO_2, O_3, N_2O, and CH_4 was used to minimize the computational burden.

To validate the ARTS absorption model, we participated in the AIRS RT model intercomparison organized by the International TOVS Study Group (ITWG), a follow up activity of the TOVS RT model intercomparison described by Garand et al. (2001). Compared were simulated Atmospheric Infrared Sounder (AIRS) radiances in the 650–2700 cm^{-1} wavenumber range. Averaged over the 52 different intercomparison scenarios, ARTS has a mean bias of only -0.11 K and mean standard deviation of 0.37 K against the Reference Forward Model RFM which

is based on the GENLN2 model (Edwards, 1992). The agreement is much better in the spectral regions dominated by water vapor (bias $< 0.02\,\mathrm{K}$), differences here are caused primarily by different continuum implementations. In the spectral regions dominated by O_3 and CO_2 ARTS has a slight cold bias of about $-0.2\,\mathrm{K}$.

2.1.3 OLR Calculation

Following the notation of Clough et al. (1992), the upwelling monochromatic radiative flux F_ν^+ and downwelling monochromatic radiative flux F_ν^- at a given atmospheric level can be calculated from the monochromatic radiance I_ν integrated over all relevant propagation angles at that level as

$$F_\nu^+(z) = \int_{\phi=0}^{2\pi} \int_{\mu=0}^{1} I_\nu(z,\mu)\,\mu\,\mathrm{d}\mu\,\mathrm{d}\phi\,, \tag{2.1}$$

$$F_\nu^-(z) = \int_{\phi=0}^{2\pi} \int_{\mu=-1}^{0} I_\nu(z,\mu)\,\mu\,\mathrm{d}\mu\,\mathrm{d}\phi\,, \tag{2.2}$$

where μ is the zenith angle cosine, ϕ the azimuth angle, and ν the frequency. The unit of the monochromatic radiative flux is F_ν is $\mathrm{W\,m^{-2}\,Hz^{-1}}$ and of monochromatic radiance I_ν is $\mathrm{W\,m^{-2}\,Hz^{-1}\,sr^{-1}}$. The integration over $\mu\,\mathrm{d}\mu$ and $\cos(\theta)\,\sin(\theta)\,\mathrm{d}\theta$ are equivalent, where θ is the zenith angle. The term $\cos(\theta)$ is a result of the projection onto the zenith direction, since only the radiance component perpendicular to the azimuthal plane contributes to the flux. The remaining parts result from the azimuthal integration. Since radiances are assumed to be azimuthally independent the azimuthal integration is trivial and can be carried out directly, leading to

$$F_\nu^+(z) = 2\pi \int_0^1 I_\nu(z,\mu)\,\mu\,\mathrm{d}\mu \tag{2.3}$$

and a similar equation for the downwelling monochromatic radiative flux.

The total upwelling radiative flux F^+ can be calculated easily by

integrating Equation (2.3) over frequency, leading to

$$\begin{aligned} F^+(z) &= \int_0^\infty F_\nu^+(z)\,\mathrm{d}\nu \\ &= 2\pi \int_0^\infty \int_0^1 I_\nu(z,\mu)\,\mu\,\mathrm{d}\mu\,\mathrm{d}\nu \\ &= 2\pi \int_0^1 I(z,\mu)\,\mu\,\mathrm{d}\mu\,, \end{aligned} \tag{2.4}$$

where I is the (total) radiance in $\mathrm{W\,m^{-2}\,sr^{-1}}$. Finally, the net radiative flux is obtained by taking the difference between upwelling and downwelling contributions,

$$F(z) = F_\nu^+(z) - F_\nu^-(z)\,. \tag{2.5}$$

Note that the direction of positive fluxes is upwards.

2.1.4 Atmospheric Profiles

The atmospheric profile data set used for this study consists of radiosonde data collected by the research vessel Polarstern of the Alfred Wegener Institute for Polar and Marine Research (AWI) during 27 expeditions in the years 1982 to 2003 (Koenig-Langlo and Marx, 1997). The data set comprises 6189 individual profiles. It has a fairly good latitudinal and seasonal coverage, as demonstrated by Figure 2.2, although high latitudes and the summer season are over-represented. The data allow the generation of five different classes, corresponding to seasons and latitude ranges: tropical (TRO), midlatitude summer (MLS), midlatitude winter (MLW), subarctic summer (SAS), and subarctic winter (SAW). Table 2.1 gives the definitions of these classes and the number of profiles in each class. Note that the number of profiles in each class varies from over 1200 for SAS to about 50 for MLW.

To have an equal number of profiles for each class, 50 profiles for each class were randomly selected. Figure 2.3 shows the temperature statistics for the TRO and MLS classes. As expected, the variability for the TRO class is much lower than the variability for the MLS class. Figure 2.4 shows the humidity statistics for the same two classes,

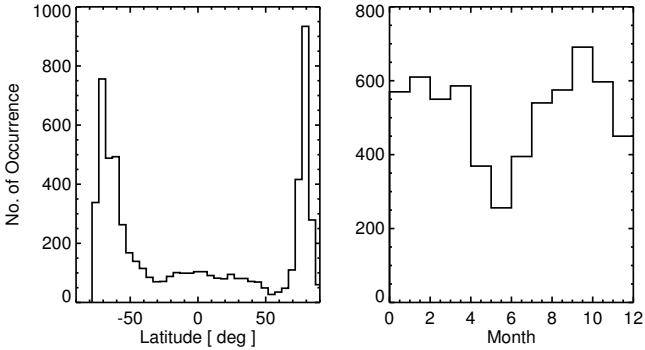

Figure 2.2: Latitudinal (left) and temporal (right) coverage of the Polarstern radiosonde data.

Table 2.1: Definition of radiosonde classes and number of profiles in each class. NH and SH means Northern hemisphere and Southern hemisphere. For an explanation of the class acronyms see text.

Scenario	Latitude Range [°]		Month Range		No. of Profiles
	NH	SH	NH	SH	
TRO	0 – 20	−20 – 0	5 – 9	5 – 9	150
MLS	35 – 50	−35 – −50	6 – 8	12 – 2	139
MLW	35 – 50	−35 – −50	12 – 2	6 – 8	52
SAS	55 – 75	−55 – −75	6 – 8	12 – 2	1279
SAW	55 – 75	−55 – −75	12 – 2	6 – 8	69

showing that, in spite of the more homogeneous temperature in the tropics, humidity variability there is as high as at midlatitude. This is true for both the absolute and the relative humidity.

The profiles normally reach up to an altitude of 18 – 30 km. As each profile reaches a different altitude, all the profiles were cut at 100 hPa. This corresponds to an altitude of approximately 16.5 km for the TRO class, 15.5 km for the MLS and MLW classes, 15.0 km for the SAS class, and 14.5 km for the SAW class, which is above the tropopause in all cases. Since the radiosonde data contain only temperature and humidity information, concentrations of CO_2, O_3, N_2O, and CH_4 were taken from the corresponding FASCOD (Anderson et al., 1986) scenarios.

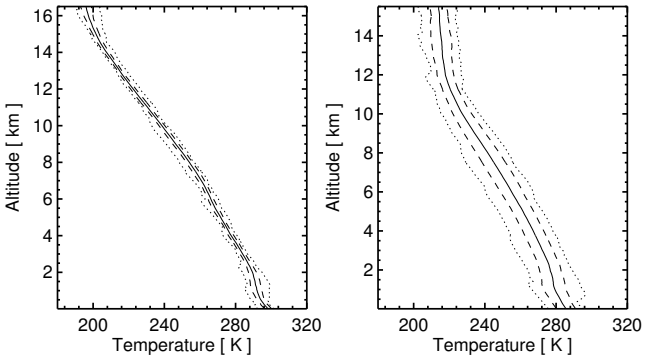

Figure 2.3: Temperature statistics for the TRO class (left) and the MLS class (right). Shown are the mean profile (solid), the mean ± one standard deviation profiles (dashed), and the maximum/minimum profiles (dotted). The maximum and minimum were determined separately for each altitude.

To investigate the role of fine vertical structures in the humidity profiles, various smoothed profiles were generated taking running means of the high resolution profiles over a certain altitude range (boxcar smoothing). Smoothing heights applied were 500 m, 1000 m, 2000 m, and 4000 m. The larger the smoothing height, the more vertical structure is lost, as demonstrated by Figure 2.5. It is crucial to note that the result of the smoothing strongly depends on the humidity unit. Figure 2.6 shows how large the differences are between smoothing in VMR, smoothing in log(VMR), and smoothing in relative humidity (RH). Smoothing in VMR increases the total column water vapor (TWV), while smoothing in log(VMR) reduces TWV. Smoothing in RH does either of these, depending on the profile. Two additional options investigated were smoothing in RH or VMR, but rescaling the smoothed profile so that TWV is conserved (called RH_c and VMR_c smoothing).

To analyze the results, two integrated measures of the tropospheric humidity content were used. The first one is the Total Water Vapor (TWV), defined here as the integrated water vapor content of the entire atmosphere. The second one is the Total Tropospheric Humidity (TTH), defined here as the average relative humidity between the surface and 200 hPa.

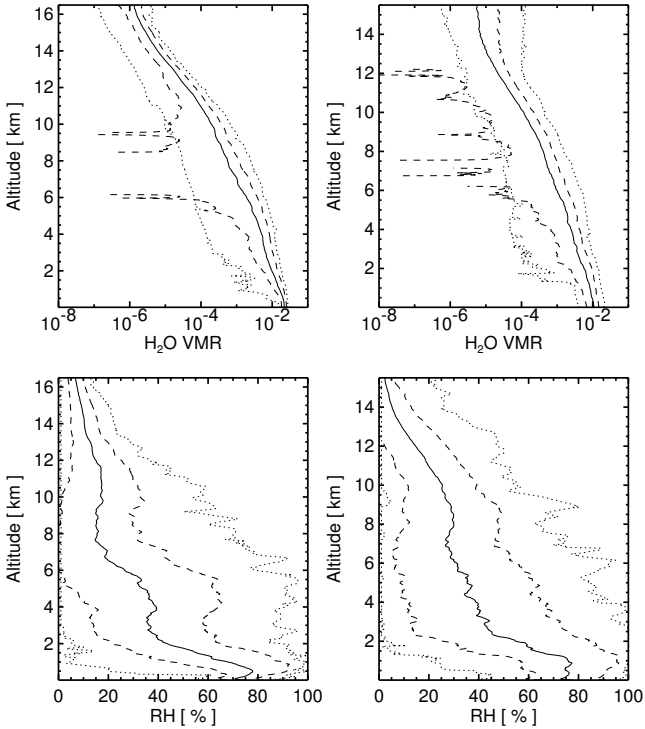

Figure 2.4: Humidity statistics for the TRO class (left column) and the MLS class (right column). Shown are mean (solid), mean ± one standard deviation (dashed), and maximum/minimum (dotted) in volume mixing ratio (VMR, top row) and relative humidity (RH, bottom row). The VMR profiles are plotted in logarithmic scale. This explains the breaks in the mean minus one standard deviation curve when the standard deviation is greater than the mean value at certain altitudes.

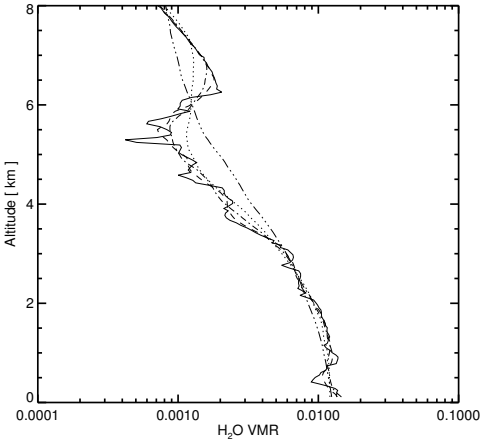

Figure 2.5: A typical radiosonde profile and smoothed profiles (VMR smoothing) with different smoothing heights (SH). Shown are the original profile (solid), 500 m SH (dashed), 1000 m SH (dash-dotted), 2000 m SH (dotted), and 4000 m SH (dash-dot-dotted).

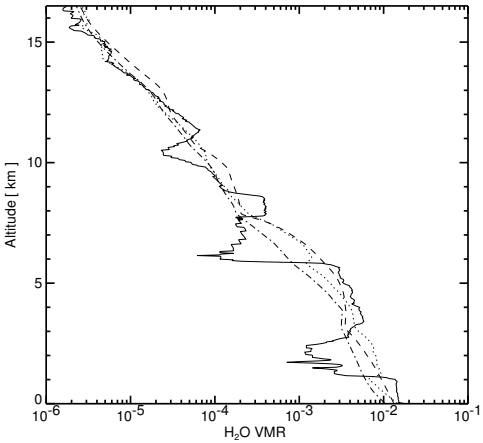

Figure 2.6: A high resolution radiosonde profile (solid) and different smoothed profiles, all with 4000 m smoothing height. The smoothed profiles were calculated in VMR (dashed), log(VMR) (dash-dotted), and RH (dotted). This is the profile that showed the largest difference in OLR for the different smoothing methods.

2.2 Results and Discussion

This section illustrates the variability of the OLR and its dependence on surface temperature and tropospheric humidity parameters. Moreover, the impact of vertical structure on the OLR variability is also discussed.

2.2.1 Mean and Variability of OLR

To study the variability of OLR, one has to use either data from a general circulation model, as done by Allan et al. (1999), or direct measurements of humidity and temperature. The AWI Polarstern radiosonde data, which were described in Section 2.1.4, were used here. Figure 2.7 shows the mean $\overline{F^+}$ and standard deviation σ_{F^+} for the OLR at 100 hPa for the different radiosonde classes. Extreme values are also indicated. The exact numbers are given in Table 2.2. The one standard deviation variability of F^+ is close to $10\,\mathrm{W\,m^{-2}}$, except for the SAW case where it is significantly higher. The global variability of OLR is $33\,\mathrm{W\,m^{-2}}$, which is estimated from the standard deviation of all the OLR values.

Table 2.2: The statistics of F^+ at 100 hPa for the different radiosonde classes. Shown are mean, standard deviation, minimum, and maximum. The unit of all four columns is $\mathrm{W\,m^{-2}}$. The sample size is 50 randomly selected profiles for each class, as described in Section 2.1.4.

Class	$\overline{F^+}$	σ_{F^+}	$\min(F^+)$	$\max(F^+)$
TRO	294.66	12.43	268.33	326.10
MLS	261.94	12.87	239.59	287.62
MLW	255.81	8.96	232.65	275.38
SAS	233.68	8.39	219.94	262.44
SAW	201.24	16.25	178.38	240.91

As discussed above, clear-sky OLR is sensitive to both temperature and humidity changes. It is therefore interesting to assess which factor is dominating the day-to-day OLR variability. Because temperature is highly correlated throughout the troposphere, it makes sense to

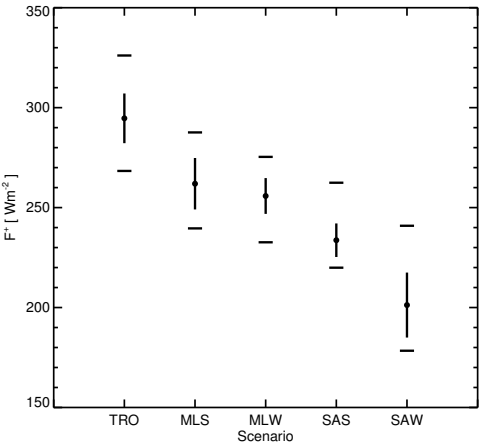

Figure 2.7: The statistics of OLR for the different radiosonde classes. Dots with error bars mark mean $\overline{F^+}$ and standard deviation σ_{F^+}, the horizontal bars above and below mark the maximum and minimum. The x-axis marks the different climatological classes from tropical (TRO) on the left side to subarctic winter (SAW) on the right side.

take the surface temperature as a proxy for tropospheric temperature, and to make a scatter plot of OLR (F^+ at 100 hPa) versus surface temperature. Figure 2.8 shows this for the AWI radiosonde data and the calculated OLR. Different symbols mark the different climatological classes.

To validate the calculations one can use data from the Clouds and the Earth's Radiant Energy System (CERES) instrument on board the Tropical Rainfall Measuring Mission (TRMM) satellite. The grey shaded area in Figure 2.8 shows the plus/minus one standard deviation variability of CERES/TRMM clear-sky OLR data from Inamdar et al. (2004). Due to the TRMM orbit, CERES/TRMM data is not available for surface temperatures below 280 K. The simulated OLR values presented here are consistent with the CERES data, although at the lower end of the CERES variability.

Figure 2.8 shows that there generally is a very good correlation between surface temperature and OLR. The parameters obtained by a

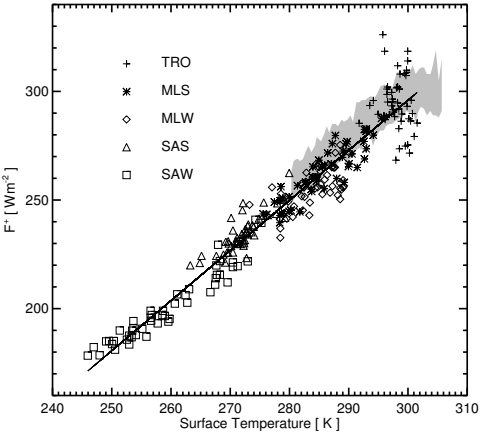

Figure 2.8: Calculated OLR (F^+ at 100 hPa) as a function of surface temperature for the five different radiosonde classes. The solid line is a linear fit to the data from all five classes. The grey shaded area shows the one standard deviation variability of CERES/TRMM data taken from Inamdar et al. (2004). Unfortunately, this data is only available for surface temperatures above 280 K.

linear fit are

$$F^+_{\mathrm{Tfit}} = 2.306\, T_{\mathrm{surface}} - 395.984\,. \tag{2.6}$$

The standard deviation of

$$F^+_{\mathrm{Tcorr}} = F^+ - F^+_{\mathrm{Tfit}} \tag{2.7}$$

is 8.5 W m^{-2}. The only notable exception is the TRO class, for which there is considerably more scatter than for the other classes. The reason for this can be understood from Figure 2.9, which displays OLR as a function of total column water vapor. It shows that for the TRO class the variability in OLR is dominated by humidity changes, not temperature changes. Only for the TRO class does OLR decrease with increasing humidity, showing the water vapor signal. For the other classes OLR increases with increasing column water vapor, which means that one sees here again the temperature signal, not the humidity signal (higher column water vapor usually implies higher tropospheric tem-

perature). This confirms the result of Allan et al. (1999) derived from OLR simulations based on ECMWF ERA-40 data.

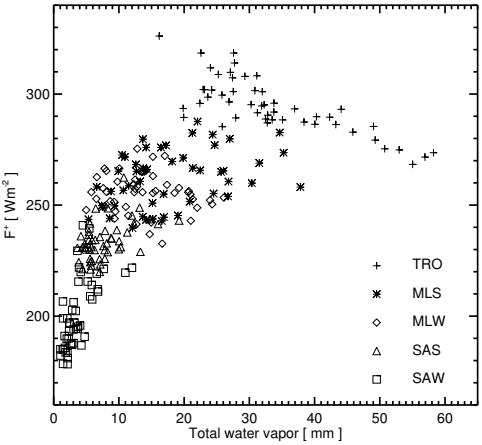

Figure 2.9: Calculated OLR (F^+ at 100 hPa) as a function of total column water vapor for the five radiosonde classes. Only the TRO class shows the expected negative humidity signal, for the other classes it is outweighed by the stronger positive temperature signal.

The reason for the different behavior of the tropics is that there simply are not as big surface temperature changes in the tropics. Or, put differently, the sensitivity to humidity changes is also present for the other classes, but masked by the large temperature variability. This can be demonstrated by plotting F^+_{Tcorr} versus Total Tropospheric Humidity (TTH, as defined in Section 2.1.4), as shown in Figure 2.10 for the TRO and SAW class. The figure confirms that for a given surface temperature the OLR variability is indeed to a large extent due to humidity changes. Moreover, there is a simple exponential relationship between TTH and F^+_{Tcorr} (note that TTH is plotted in a logarithmic scale). A fit to these data was made, according to

$$\Delta F^+_{\mathrm{Hfit}} = a\,\ln(\mathrm{TTH}) + b\,. \tag{2.8}$$

The two fit examples show that this relationship is fulfilled quite well. The other classes show a similarly good fit quality, but were omitted

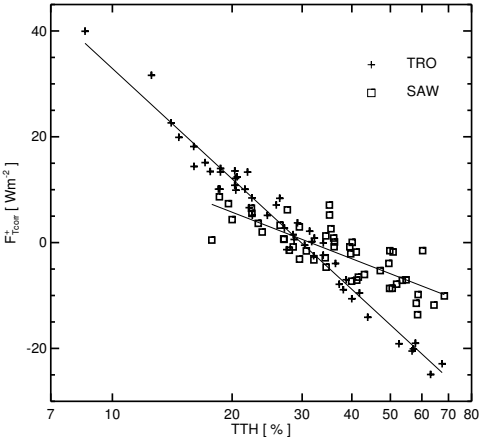

Figure 2.10: Temperature corrected OLR (F^{+}_{Tcorr}) versus Total Tropospheric Humidity (TTH). Only the TRO and SAW classes are shown to avoid clutter.

for clarity. Table 2.3 summarizes for all classes the fit parameters, as well as the residual variability, defined as the standard deviation of the difference of the data and the fitted line. The residual variability is only 2.3 to 3.4 $\mathrm{W\,m^{-2}}$, depending on the radiosonde class.

Table 2.3: Fit parameters and residual variability for an exponential fit according to Equation (2.8) to the temperature corrected OLR F^{+}_{Tcorr} versus TTH. All quantities are in $\mathrm{W\,m^{-2}}$, the parameter a is for TTH in fractional RH, not in %RH.

Class	a	b	σ_{res}
TRO	−30.108	102.232	2.368
MLS	−14.800	52.294	2.945
MLW	−17.915	59.431	2.294
SAS	−12.216	47.677	3.352
SAW	−12.691	43.763	3.261

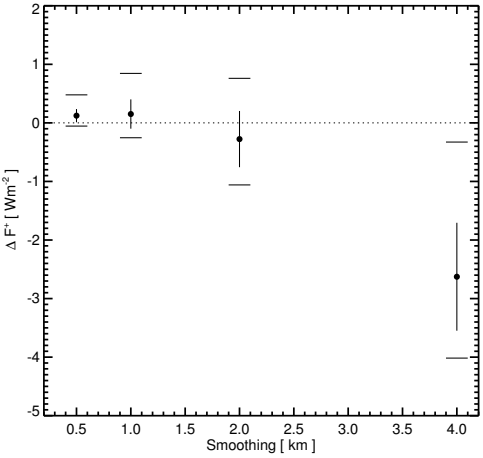

Figure 2.11: The statistics of the deviation of OLR for smoothed profiles from the high resolution reference. Shown are the mean difference and its standard deviation, together with maximum and minimum values. This is for the TRO class with VMR smoothing.

2.2.2 Impact of Vertical Structure

The residual variability after surface temperature and TTH correction must be due to the vertical distribution of temperature and humidity. This brings up the problem that vertical structure is measured only with a coarse resolution by typical remote sensing instruments. To assess this, simulations with smoothed versions of the radiosonde data were carried out.

Figure 2.11 shows for the TRO class the statistics of the change in OLR if the humidity profiles are smoothed in VMR with different smoothing heights. The mean difference for a 4 km smoothing of the TRO class is approximately 2.6 $\mathrm{W\,m^{-2}}$. Thus, VMR smoothing leads to a significant bias in OLR for smoothing heights above 2 km (compare the number to the 1.6–3.0 $\mathrm{W\,m^{-2}}$ for CO_2 doubling (von Engeln et al., 2004b)). Fortunately, limb sounding instruments, for which the retrieval should do something close to a VMR smoothing, typically have smoothing heights of approximately 2.5 km or slightly better.

Down looking passive instruments like the High Resolution Infrared

Radiation Sounder (HIRS) or the Advanced Microwave Sounding Unit (AMSU) have an intrinsic smoothing height as large as 4 km. However, these instruments are in good approximation sensitive to vertically averaged relative humidity, as shown for example by Soden and Bretherton (1996) for HIRS and by Buehler and John (2005) for AMSU, so that RH smoothing is more appropriate than VMR smoothing. For RH smoothing there is practically no bias, as shown by Figure 2.12, which compares the different investigated smoothing methods for 4 km smoothing altitude.

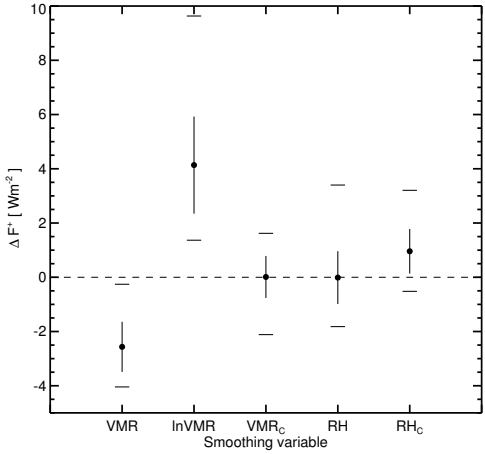

Figure 2.12: Impact of different smoothing methods on OLR for the TRO class. The smoothing height is 4 km. Shown are mean, standard deviation, and maximum/minimum values of the deviation, as in Figure 2.11.

Of all investigated smoothing methods, RH smoothing and VMR_c smoothing are the methods that introduces the smallest bias. The conclusion for RH smoothing holds for all investigated atmospheric classes, as shown by Figure 2.13. Thus, OLR calculated from measurements of sensors with such coarse vertical resolutions can indeed have the correct mean values. However, it should not be forgotten that the deviations for individual profiles can be quite high, the standard deviation for the TRO case with 4 km smoothing height is $1\,\text{W}\,\text{m}^{-2}$.

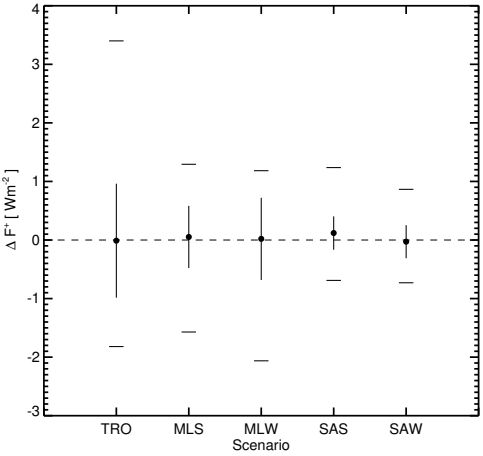

Figure 2.13: Effect of RH smoothing with 4 km smoothing height for all atmospheric classes. Shown are mean, standard deviation, and maximum/minimum values of the deviation, as in Figure 2.11 and Figure 2.12.

2.3 Summary and Conclusions

A line-by-line radiative transfer model was used to simulate the clear-sky outgoing longwave radiation flux. High resolution radiosonde data from the research vessel Polarstern of the Alfred Wegener Institute for Polar and Marine Research (AWI) were used to investigate the variability of OLR and the impact of vertical structure in the humidity profiles on the OLR variability.

The global variability in clear-sky OLR is approximately 33 $\mathrm{W\,m^{-2}}$, estimated by the standard deviation of all OLR values calculated from AWI radiosondes. This large variability can be explained to a large extent by variations in the effective tropospheric temperature, or in the surface temperature as a proxy. That component of the variability can be removed by making a linear fit of OLR versus surface temperature. The then remaining variability is approximately 8.5 $\mathrm{W\,m^{-2}}$. Of this remaining variability a significant part can be explained by variations in the Total Tropospheric Humidity (TTH). Making a linear fit of the temperature independent OLR variations against the logarithm of TTH reduces the remaining variability to only approximately 3 $\mathrm{W\,m^{-2}}$.

This remaining variability must be due to vertical structure. It was shown that humidity structures on a vertical scale smaller than 4 km contribute a variability of approximately $1\,\mathrm{W\,m^{-2}}$, but no significant bias if the smoothing is done in the right way. The right way to smooth is in relative humidity, if the smoothing is done for example in VMR it leads to a substantial bias. This result means that measurements from sensors with coarse vertical resolution may be used to predict OLR with the correct mean values, but will not be able to fully reproduce the variability due to vertical structure, as almost half of that can come from structures on a scale smaller than 4 km. This calls for sensors that can sound the troposphere, including the upper troposphere, with good vertical resolution.

3 ARTS – A Radiative Transfer Model for AMSU

In Chapter 2, we have already seen the application of a radiative transfer (RT) model to study the variability of the outgoing longwave radiation. One of the main tools for the understanding and the utilization of satellite data is also an RT model. An RT model is a set of computer codes, which solves the radiative transfer equation. The radiative transfer equation describes the interaction of radiation with the medium of propagation. In the context of this thesis, it is the interaction of microwave radiation with the Earth's atmosphere. In the realm of satellite data analysis, an RT model is often called a forward model, which describes the physics of the measurement process. Thus, a forward model simulates measurements as observed by a remote sensing instrument (for which the model is configured) for a given atmospheric state. The reverse of this process, i.e., obtaining the atmospheric state given a set of measurements is called an inverse problem (Rodgers, 2000).

The concept of the RT theory and definition of terms, which are often used in the thesis, are discussed in Section 3.1. The description of a forward model, the Atmospheric Radiative Transfer Simulator (ARTS), which is used for all radiative transfer calculations presented in this thesis is given in Section 3.2.

Another aim of this chapter is to describe how ARTS can be used as a forward model for the Advanced Microwave Sounding Unit (AMSU), which is mainly used for measuring water vapor and temperature of the Earth's atmosphere. Section 3.3 introduces the AMSU instrument and Section 3.3.2 discusses how ARTS is configured as a forward model for AMSU. The validation of the ARTS model is also discussed in this section.

The last section of this chapter explains how the weak ozone lines in the AMSU frequency range can influence the instrument's measurements (John and Buehler, 2004a).

3.1 The Radiative Transfer Theory

Radiation propagating through the Earth's atmosphere undergoes two major interactions with its matter: extinction and emission. The extinction is manifested by absorption and scattering. In the microwave frequency range, the scattering is negligible under normal atmospheric conditions, except in the presence of precipitating clouds and thick ice clouds. Therefore the discussion of the RT theory here is limited to a non-scattering atmosphere. A detailed discussion of RT theory in the presence of clouds can be seen, for example, in Sreerekha (2005).

The radiation field can be described in terms of the specific intensity I_ν, which is defined as the radiant power propagating in a given direction per unit area, per unit solid angle, and per unit frequency interval (Janssen, 1993). The change in I_ν for a given frequency ν at a point along its direction of propagation can be written as:

$$\frac{\mathrm{d}I_v}{\mathrm{d}s} = -\alpha I_v + S\,, \tag{3.1}$$

where α is the absorption coefficient. The first term (in the right hand side) of the above equation describes the loss and the second term describes the gain (source) of energy into the given direction. Equation (3.1) is the differential form of the radiative transfer equation.

In the absence of scattering, the source term S represents only the local contribution to the radiation. If one assumes local thermodynamic equilibrium, which means that each point of the medium can be characterized by a single thermodynamic temperature, the source function S is given by the absorption coefficient times the Planck function:

$$S = \alpha B_v(T)\,, \tag{3.2}$$

where B_ν is the Planck function,

$$B_v(T) = \frac{2h\nu^3}{c^2} \frac{1}{\mathrm{e}^{\frac{h\nu}{kT}} - 1}\,. \tag{3.3}$$

Here, h is Planck's constant, k is Boltzmann's constant, and c is the speed of light. The Planck function describes the radiance emitted by a black body. Substituting Equation (3.2) in Equation (3.1) and solving gives

$$I_\nu(0) = I_\nu(s_0)\, e^{-\tau(s_0)} + \int_0^{s_0} B_\nu(T)\, e^{-\tau(s)}\, \alpha\, \mathrm{d}s\,. \tag{3.4}$$

Here, τ is the optical depth which is defined as:

$$\tau(s) = \int_0^s \alpha(s')\, \mathrm{d}s'. \tag{3.5}$$

The optical depth (which is also called opacity) describes how opaque the atmosphere is, for a given frequency.

The unit of intensity is $\mathrm{W\,m^{-2}\,Hz^{-1}\,sr^{-1}}$, but in microwave radiometry the measured intensity is normally represented in terms of the brightness temperature, T_B, which is expressed in Kelvin (K). The brightness temperature is the temperature a black body shall have to emit the same intensity as measured. The concept of brightness temperature is broadly used in microwave radiometry as it gives a more intuitive understanding of measured radiances. The brightness temperature can be obtained by inverting the Planck function,

$$T_\mathrm{B} = B_\nu^{-1}(I_\nu)\,, \tag{3.6}$$

where B_ν^{-1} is the inverse of the Planck function applied to the observed radiance, I_ν**.** The exact formula of the Planck brightness temperature can be derived from Equation (3.3):

$$T_\mathrm{B}(\nu) = \frac{h\nu}{k \ln(1 + \frac{2h\nu^3}{c^2 I_\nu})}\,. \tag{3.7}$$

At longer wavelengths and lower temperatures, i.e., $h\nu \ll kT$, the Planck function can be approximated to:

$$B_\nu(T) \approx \frac{2\nu^2 kT}{c^2}, \tag{3.8}$$

which is called the Rayleigh-Jeans (RJ) approximation. The Rayleigh-Jeans brightness temperature is defined as:

$$T_{\mathrm{B}}^{\mathrm{RJ}}(\nu) = \frac{c^2 I_\nu}{2\nu^2 k}. \tag{3.9}$$

Since this approximation can introduce non-negligible errors in the frequency range of interest, it was decided to use the Planck brightness temperature as described by Equation (3.7) throughout this thesis.

3.2 Atmospheric Radiative Transfer Simulator

The Atmospheric Radiative Transfer System (ARTS) is a radiative transfer model which can simulate measurements of remote sensing instruments measuring thermal emission by the Earth and its atmosphere. It can be used for all viewing geometries: down (or nadir), up, and limb. ARTS has two versions. One is a clear sky version (Buehler et al., 2005b) which is stable and validated against other models (Melsheimer et al., 2005) and with observation (Buehler et al., 2004; Kuvatov, 2002). The other is a scattering version (Emde et al., 2004) which can take into account the effect of ice and liquid clouds. This is a recent activity and validations are being done. The main features of the program are modularity, extendability, and generality. Besides producing spectra, ARTS calculates Jacobians for temperature, trace gas concentrations, continuum absorption, ground emission, and pointing off-sets. ARTS is publicly available on the website: http://www.sat.uni-bremen.de/arts/.

Before solving the RT equation, it is necessary to calculate the absorption coefficient α. In ARTS, the absorption coefficient can be computed in two ways. One is by explicit line-by-line calculations using standard spectral line catalogs and then adding a continuum term. The other is by using complete absorption models such as the one by Liebe (1989) and the one by Rosenkranz (1993). These full absorption models internally contain a collection of spectral lines, as well as the

matching continua. Details of the absorption implementation in ARTS can be seen in Kuhn (2004).

Another important quantity to calculate in the retrieval process is the derivative of the forward model which is generally called the Jacobian or the weighting function. It can be mathematically expressed as:

$$\mathbf{K} = \frac{\partial F}{\partial \mathbf{x}}, \tag{3.10}$$

where F represents the forward model and $\mathbf{x}$ represents atmospheric parameters, for example, the temperature or the concentration of a trace gas.

The general and straightforward way to calculate Jacobians is the perturbation method, but this method is not computationally efficient. Therefore Jacobians are calculated analytically or semi-analytically in ARTS. The ARTS provides Jacobians for atmospheric species concentration in three units: number density, volume mixing ratio and relative changes with respect to the normalization state (fractional unit). When the Jacobian is calculated in fractional units, it corresponds to a 100% increase in species abundance. The Jacobians for water vapor in this thesis are expressed in fractional units, unless other units are stated.

3.3 Advanced Microwave Sounding Unit

A big step forward in the history of the sounding of the Earth's atmosphere from space was the introduction of microwave sounders on board polar orbiting satellites. The Advanced Microwave Sounding Unit (AMSU) is a new generation microwave radiometer meant for the temperature and the water vapor sounding of the atmosphere. The AMSU has 20 channels. Positions of these channels are shown in Figure 3.1. The AMSU consists of two instruments, the AMSU-A (Mo, 1996) and the AMSU-B (Saunders et al., 1995). The AMSU is on-board the NOAA-15, 16, and 17 satellites, thus sampling a particular point on the Earth six times a day.

These instruments are cross-track scanning microwave sensors with a swath width of approximately 2300 km. They measure microwave thermal emission emitted by the Earth and its atmosphere in the oxygen band of 50–58 GHz (AMSU-A), the two water vapor lines at 22 GHz (AMSU-A) and 183 GHz (AMSU-B), and window regions (both). The AMSU has 20 channels, where Channels 1–15 are part of AMSU-A and Channels 16–20 are part of AMSU-B. The temperature information of the atmosphere can be obtained from Channels 4–14 of AMSU-A. Three Channels 18, 19, and 20 of AMSU-B which are centered around the 183.31 GHz water vapor line can give humidity information on the upper, the middle, and the lower troposphere, respectively. Note that the Channel 15 on AMSU-A and the Channel 16 on AMSU-B are both located at 89 GHz, the difference is only in the horizontal resolution.

AMSU-A and AMSU-B scan the atmosphere with different footprints. AMSU-A samples the atmosphere in 30 scan positions across the track with a footprint size of $50 \times 50\,\mathrm{km}^2$ for the innermost scan position. This size increases to $150 \times 80\,\mathrm{km}^2$ for the outermost position from nadir. AMSU-B samples the atmosphere in 90 scan positions with footprint size varying from $20 \times 16\,\mathrm{km}^2$ at the innermost scan position to $64 \times 27\,\mathrm{km}^2$ at the outermost scan position.

Since the work described in this thesis is based only on AMSU-B data, the rest of this chapter discusses the details of the AMSU-B instrument.

3.3.1 AMSU-B

The AMSU-B is a 5 channel microwave radiometer. The purpose of the instrument is to receive and measure radiation from different layers of the atmosphere in order to obtain global data on tropospheric humidity. AMSU-B channel positions are shown in Figure 3.2 and the radiometric characteristics are given in Table 3.1. Note that all five channels are double sideband channels. Double sideband operation improves the instrument's temperature sensitivity by reducing its effective noise temperature.

Figure 3.2 shows the zenith opacity of a midlatitude summer atmosphere for the AMSU-B frequency range. The zenith opacity is the

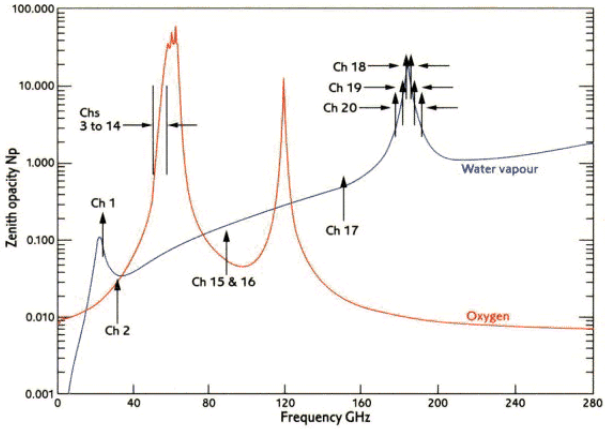

Figure 3.1: Atmospheric zenith opacity due to oxygen and water vapor for the microwave frequency range. The zenith opacity is the vertically integrated absorption coefficient. The zenith opacity is higher close to spectral lines. AMSU channel positions are also shown. (Figure from the UK Met Office)

Table 3.1: AMSU-B channel characteristics.

Channel number	Central frequency [GHz]	No. of passbands	Bandwidth per passband [MHz]	$NE\Delta T$ [K]
16	89.00 ± 0.90	2	1000	0.37
17	150.00 ± 0.90	2	1000	0.84
18	183.31 ± 1.00	2	500	1.06
19	183.31 ± 3.00	2	1000	0.70
20	183.31 ± 7.00	2	2000	0.60

vertically integrated absorption coefficient and it can be calculated using Equation (3.5). The opacity in this frequency range is mainly due to three gaseous species: water vapor, oxygen, and nitrogen. Nitrogen does not have any spectral line here, but water vapor and oxygen have one line each. A frequency range where no spectral line is present is called a window region. Channels 16 and 17 are located at such regions where the opacity is close to one.

As explained in Petty (2004), if the integration in Equation (3.5) is

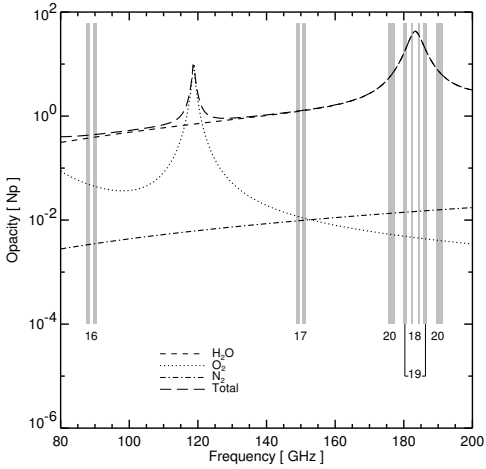

Figure 3.2: AMSU-B channel positions. The total zenith opacity and individual zenith opacities for water vapor, oxygen, and nitrogen, calculated by ARTS, are also shown for a midlatitude-summer atmosphere (Anderson et al., 1986). The zenith opacity is the vertically integrated absorption coefficient. The shaded bands denote the passbands of AMSU-B channels. The channel numbers are marked below the passbands.

started from the top of the atmosphere, a channel gets saturated or the atmosphere becomes opaque to that channel at that layer of the atmosphere where the opacity becomes one ($\tau = 1$), a rule sometimes referred to as Chapman's rule. To put it in other words, the Jacobian of a channel peaks where the opacity becomes one. Thus, Channels 16 and 17 can see through the atmosphere and are sensitive mostly to the Earth's surface. Therefore these channels are called surface channels. The sensitive altitudes of these channels can also be seen from the Jacobian.

Water vapor Jacobians for Channels 16 and 17 are shown in Figure 3.3 for two different atmospheres. Upper panels are for a moist tropical atmosphere and lower panels are for a dry midlatitude winter atmosphere. The solid curve represents a nadir view (looking exactly down) and the dashed curve represents the maximum off-nadir view (48.95° in the case of AMSU-B) of the instrument. In the off-nadir po-

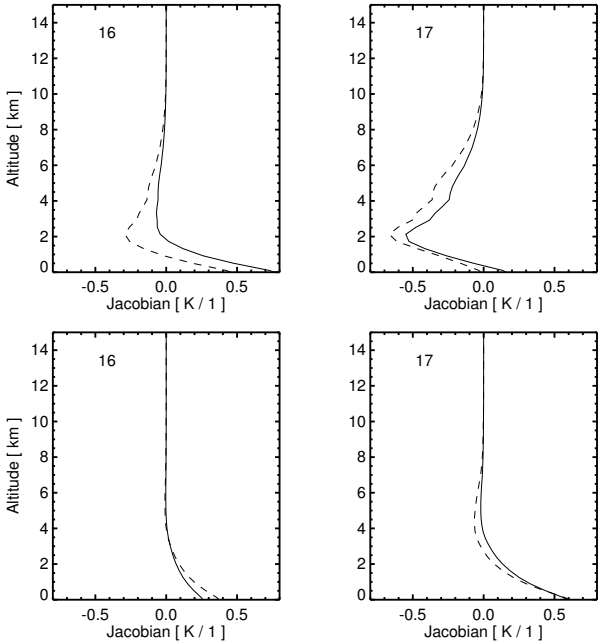

Figure 3.3: Water vapor Jacobians for AMSU-B Channels 16 and 17. The upper panels show Jacobians for a moist tropical atmosphere while the lower panels are for a dry midlatitude winter atmosphere. Two viewing geometries are also shown, the solid curve represents the nadir view and the dashed curve represents the maximum off-nadir view.

sition, radiation has to travel in a slanted path, therefore the path length will be longer (about 50% more for the most off-nadir view compared to the nadir view), resulting in a larger opacity.

Jacobians are calculated by increasing the amount of water vapor at each vertical grid point. Therefore a positive value implies that adding water vapor will increase the radiance observed by the instrument and vice versa. Channel 16 behaves as surface channels in both atmospheric scenarios for any viewing angle. But Channel 17 acts as a sounding channel in the moist tropical atmosphere with a maximum sensitivity at 2 km.

It is clear from Figure 3.2 that Channels 18–20 are located on the

wings of the water vapor line at 183.31 GHz. The atmospheric opacity for these channels differs significantly, which makes these channels sensitive to different layers of the atmosphere. Therefore these channels are referred to as sounding channels. The band width of these channels increases with the channel numbers, Channel 18 being the narrowest and Channel 20 being the broadest. The bandwidth is adjusted in such a way that each channel is sensitive to a specific layer of the atmosphere and the noise equivalent temperature ($NE\Delta T$, see Table 3.1) is as low as possible. The $NE\Delta T$ is connected to the bandwidth through the radiometric formula,

$$NE\Delta T = \frac{T_{\text{sys}}}{\sqrt{B\, t_{\text{int}}}}\,, \tag{3.11}$$

where T_{sys} is the system temperature, B is the bandwidth, and t_{int} is the integration time. This is the reason why $NE\Delta T$ decreases with increasing bandwidths for Channels 18–20, given T_{sys} and t_{int} are the same for all channels.

Water vapor Jacobians for Channels 18–20 are shown in Figure 3.4. Here also, Jacobians are given for a tropical and a midlatitude winter atmospheres and for the nadir and the maximum off-nadir viewing angles. It is clear from the figure that the channels are sensitive to different layers of the atmosphere. The channels are sensitive to broad layers of the atmosphere, which is a drawback of nadir sounding instruments. In the moist tropical atmosphere, the Channel 18 Jacobian is centered around 8 km, but in the dry midlatitude winter atmosphere it is centered around 6 km. This is due to the fact that the opacity is larger for the tropical atmosphere. Jacobians corresponding to off-nadir angles (dashed lines) peak at slightly higher altitudes because of the longer path length the radiation has to travel. Therefore the humidity information provided by these channels is coming from different layers of the atmosphere depending on the type of the atmosphere and the viewing geometry of the instrument.

The change in brightness temperature with viewing angle is called limb effect. The limb effect can be different for surface channels and sounding channels. For surface channels, the radiation has to travel longer path lengths, thus, increasing the brightness temperature mea-

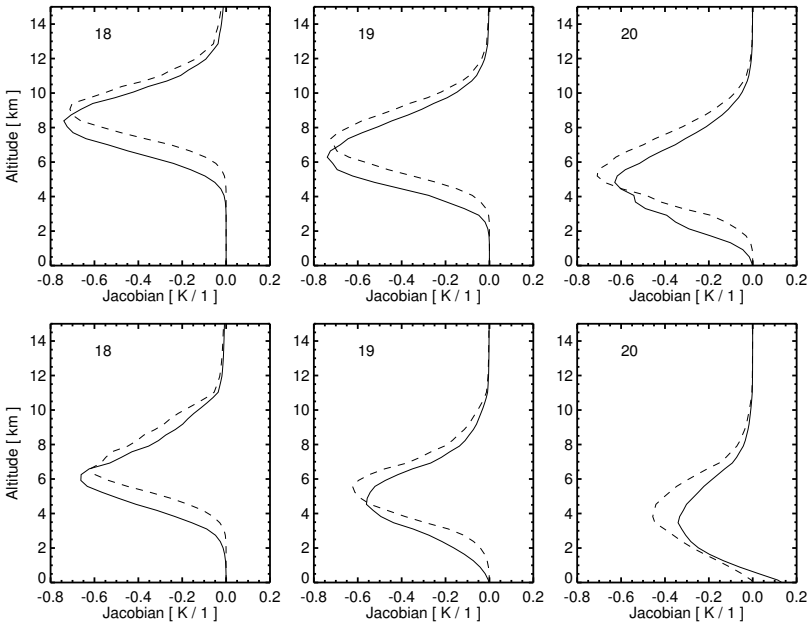

Figure 3.4: Same as Figure 3.3 but for AMSU-B Channels 18–20.

sured by the instrument. This is due to the emission from the atmosphere against a radio-metrically colder surface (surface emissivity is much less than one for ocean surface). This is called limb brightening. But for sounding channels, a longer path length implies that the channels peak higher in the atmosphere, thus, producing a lower brightness temperature due to a positive temperature lapse rate in the troposphere. This is called limb darkening. The magnitude of the limb brightening for Channels 16 and 17 can be very much varying with the surface emissivity, from about 1 K for an emissivity of 0.95 to about 25 K for an emissivity of 0.6, but the magnitude of the limb darkening for the sounding channels can be as large as 7 K as shown in Buehler et al. (2004).

The AMSU data (level 1b) which are used in this thesis were obtained from the Comprehensive Large Array-data Stewardship System (CLASS) of the US National Oceanic and Atmospheric Administration

(NOAA). We used the ATOVS and AVHRR Processing Package (AAPP) to convert the data from level 1b to level 1c.

3.3.2 Configuring ARTS for AMSU

The ARTS is a general purpose model with many options and free parameters. This section describes some choices of these parameters made for the special case of simulating AMSU measurements. The species considered were water vapor, oxygen, and nitrogen as they are believed to be the major atmospheric constituents which can contribute to the radiance measured by AMSU channels as shown in Figure 3.2.

Since full absorption models are computationally faster, the absorption coefficients for AMSU frequencies were calculated according to Rosenkranz (1998) for water vapor and Rosenkranz (1993) for oxygen and nitrogen. The details of the absorption calculation can be seen in (Buehler et al., 2003, 2005b).

In ARTS, absorption coefficients are computed on a fixed pressure grid specified by the user. For the radiative transfer integration the step length along the line of sight was taken to be 50 m, unless other values are stated. Atmospheric refraction was turned off, since it has negligible impact for AMSU viewing angles. Cosmic background radiance was set to a value corresponding to an equivalent brightness temperature of 2.735 K and the satellite altitude was taken to be 850 km. Monochromatic calculations were performed for 11 frequencies inside the passbands, and the results are convolved with the sensor passband response, which was assumed to be rectangular. It was also tested whether a Gaussian passband response would lead to significant differences, but brightness temperature differences were well below 0.1 K. It would be preferable to use measured passband responses, but unfortunately no such measurements are currently available for AMSU-B (Nigel Atkinson, personal communication). Radiances were calculated and converted to Planck brightness temperatures.

3.3.3 Validation

Under the initiative of the International TOVS Working Group (ITWG), a model intercomparison was done for infrared and microwave radiative transfer models (Garand et al., 2001). Since this intercomparison was done before ARTS was fully developed, it did not participate in the comparison. However, the intercomparison input data and results of the other models are still available so that ARTS calculations could be compared with the other models.

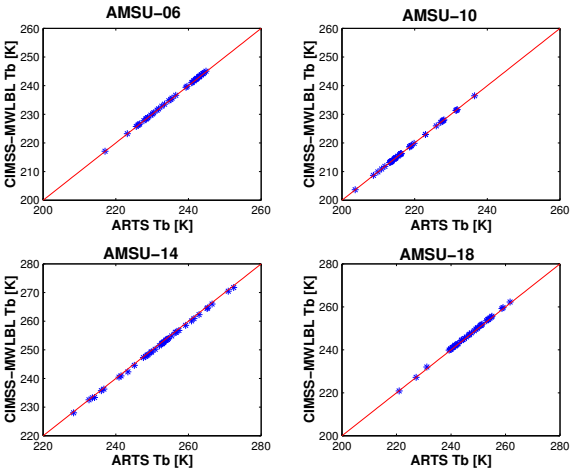

Figure 3.5: CIMSS-MWLBL brightness temperatures versus ARTS brightness temperatures for AMSU Channels 6, 10, 14, and 18.

In the microwave case CIMSS-MWLBL (Rosenkranz, 1995) was taken as the reference model and comparisons were done for AMSU Channels 6, 10, 14, and 18. The corresponding frequencies are 54.4, 57.29 ± 0.217, $57.29 \pm 0.3222 \pm 0.0045$, and 183.31 ± 1.00 GHz, respectively. There were 42 atmospheric profiles given for radiative transfer calculation in 43 pressure levels. Ground emissivity was taken as 0.6, ground temperature was set to the temperature of the lowermost grid point of each profile, and calculations were done for the nadir viewing geometry. Figure 3.5 illustrates that ARTS shows good agreement with

the CIMSS-MWLBL. The standard deviations for all the four channels are below 0.2 K and no significant bias was found between the models. Some results of this comparison are also presented in John et al. (2002).

3.4 The Impact of Ozone Lines on AMSU-B Radiances

The use of satellite data for numerical weather prediction (NWP) or climate research is based directly or indirectly on radiative transfer models. Therefore, accurate and fast radiative transfer models are a pre-requisite for proper utilization of satellite data. As mentioned in Section 3.3.1, water vapor, oxygen, and nitrogen are considered to be spectroscopically active atmospheric gases in the AMSU-B frequency range while performing RT calculations. But, there is a large number of weak ozone lines in this frequency range as shown in Figure 3.6. These lines are not yet considered in the RT models for AMSU-B, for example, the RTTOV (Saunders et al., 1999) which is a fast RT model used by most of the meteorological agencies to assimilate AMSU-B radiances in their NWP models (R. Saunders, personal communication, 2004). Radiative transfer calculations excluding these lines can introduce systematic biases and random errors in the simulated brightness temperature of AMSU-B channels. The aim of this section is to evaluate the impact of these ozone lines on AMSU-B brightness temperature. The results presented in this section are published in John and Buehler (2004a).

3.4.1 Data and Methodology

Atmospheric Data Sets

Two data sets were used to study this impact: the FASCOD and the ECMWF profiles. The FASCOD (Anderson et al., 1986) profiles consist of pressure, temperature and volume mixing ratio profiles of atmospheric trace gases for five climate zones: the tropical (TRO), the midlatitude

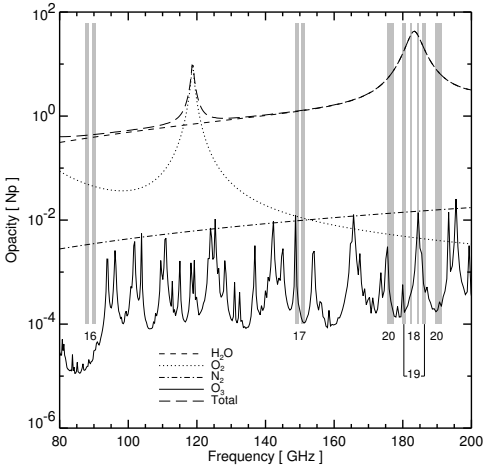

Figure 3.6: Simulated atmospheric zenith opacity for the FASCOD midlatitude summer scenario for H_2O (dashed), O_2 (dotted), N_2 (dash dotted), and O_3 (solid). The long dashed line represents the total opacity. Shaded regions represent the passband positions of AMSU-B channels. The channel numbers are also printed near the passbands.

summer (MLS), the midlatitude winter (MLW), the subarctic summer (SAS), and the subarctic winter (SAW). These climatological profiles are used to study the impact for different atmospheric scenarios.

The 60-level sampled ECMWF data set (Chevallier, 2001) consists of 13495 atmospheric profiles of temperature, water vapor, and ozone. The profiles are sampled in such a way that the atmospheric variability is covered as much as possible. The profiles reach up to 0.1 hPa. The high variability and large sample size of this data set allow us to make a statistics of the ozone impact on AMSU-B channels.

Radiative Transfer Setup

The RT model setup for this study was as described in Section 3.3.2. In the case of O_3, absorption coefficients were calculated using the HITRAN-2000 spectroscopic data base (Rothman et al., 2003). The lineshape was a hybrid, which behaves as a Van Vleck-Weisskopf lineshape in the high pressure limit and as a Voigt lineshape in the low

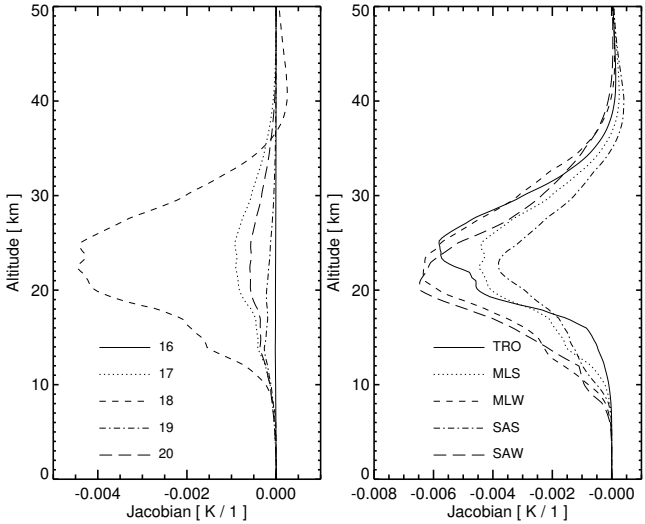

Figure 3.7: O_3 Jacobians of AMSU-B channels. The Jacobians are in fractional units, so that the values correspond to the change in brightness temperature for a doubling of the volume mixing ratio at one vertical grid point (Buehler et al., 2005b; Buehler and John, 2005). The left panel shows Jacobians of all channels for the MLS scenario and the right panel shows Jacobians of Channel 18 for all scenarios.

pressure limit, as described in Buehler et al. (2005b). In order to make accurate RT calculations, 110 monochromatic frequencies were used in each passband of each AMSU channel and radiances were convoluted with a rectangular passband response.

3.4.2 Impact of Ozone

Figure 3.6 displays atmospheric zenith opacity for the FASCOD MLS scenario for H_2O, O_2, N_2, and O_3. Passband positions of AMSU-B channels are also shown. There is a relatively strong O_3 line at the upper passband of Channel 18. This line locally contributes to the opacity more than O_2 or N_2 does. There are two other relevant O_3 lines, one at the lower passband of Channel 17 and the other at the lower passband of Channel 20, which make these channels sensitive to

O_3. There are no O_3 lines at the passband positions of Channels 16 and 19.

AMSU-B channel Jacobians, i.e., the changes in brightness temperature with respect to changes in ozone concentration, show qualitatively whether these ozone lines have any influence on the channel brightness temperature and if so, which altitude is sensitive. The Jacobians are displayed in Figure 3.7. It can be seen from the left panel, which displays O_3 Jacobians for the MLS scenario, that Channel 18 is the most affected and Channel 16 is the least affected by O_3. Channels 17 and 20 are also affected to a certain extent. The right panel shows Channel 18 O_3 Jacobians for different scenarios. The two winter scenarios show the maximum sensitivity and the summer scenarios the least. The values of the Jacobians are negative which indicates a decrease in brightness temperature due to O_3.

The brightness temperature difference, ΔT_B, is defined as the difference between brightness temperatures calculated with and without ozone. A negative ΔT_B means brightness temperature is reduced when ozone is included in the RT calculation. Results are presented for the nadir viewing geometry, unless the viewing geometry is explicitly stated.

The ΔT_B values for all FASCOD climatological scenarios are shown in Table 3.2 and are negative for all channels and scenarios, the largest for Channel 18 and the smallest for Channel 16. The ΔT_B is less than or equal to a mK for all scenarios for Channel 16. It varies from -0.026 to -0.053 K for Channel 17, from -0.14 to -0.32 K for Channel 18, from -0.009 to -0.016 K for Channel 19, and from -0.027 to -0.037 K for Channel 20. Though the ozone line at the lower passband of Channel 17 is as strong as the line at the upper passband of Channel 18, the effect is less for Channel 17 due to the larger bandwidth. The ΔT_B values were calculated for the most off-nadir AMSU-B viewing angle also and the values are higher than those of the nadir calculations, for example, ΔT_B for Channel 18 is -0.479 K for the MLS scenario. This is due to the longer path length that the radiation travels for off-nadir viewing angles.

Total water vapor (TWV) and total ozone (TOZ) values of the scenarios are also given in Table 3.2. ΔT_B does not exhibit any clear

Table 3.2: Difference in mK between simulated brightness temperatures for all FASCOD profiles excluding and including O_3. In all cases, inclusion of O_3 decreases the brightness temperature. Total ozone (in Dobson units) and total water vapor (in mm) are also given.

	TRO	MLS	MLW	SAS	SAW
16	−0.7	−0.9	−0.7	−0.7	−0.4
17	−53.0	−50.0	−40.7	−38.8	−25.5
18	−234.0	−196.0	−320.9	−143.1	−308.8
19	−9.0	−12.2	−16.2	−10.9	−15.0
20	−31.2	−33.8	−37.1	−28.7	−27.4
TOZ	285.64	337.71	381.42	350.64	378.19
TWV	41.99	29.82	8.65	21.18	4.22

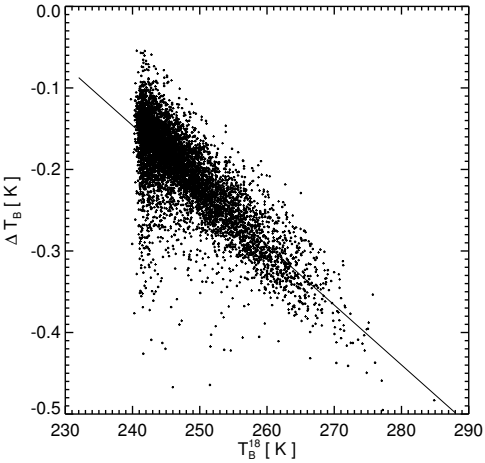

Figure 3.8: ΔT_B versus AMSU-B Channel 18 simulated brightness temperature. In this case ΔT_B is calculated as the difference between brightness temperature with ozone and brightness temperature without ozone.

dependence on either of these quantities. It is not possible to make any statistics of ΔT_B using climatological profiles. Therefore, we used the ECMWF data set, which is described in Section 3.4.1, to derive the statistics and profile dependence of ΔT_B.

The statistics of ΔT_B computed using ECMWF data are given in Table 3.3. As expected, Channel 18 shows the maximum brightness temperature difference with a mean of about -0.20 ± 0.06 K due to

ozone. Channels 17 and 20 show brightness temperature difference of −0.03 K and Channels 16 and 19 show negligible differences due to ozone. Any explicit relationship of ΔT_B with total ozone or total water vapor is not observed. However, interestingly, a good correlation of -0.79 can be observed between the Channel 18 brightness temperature and the ΔT_B as shown in Figure 3.8. The solid straight line shows a linear fit between the two quantities which has a slope of 0.007 K/ K and an offset of 1.62 K.

Table 3.3: The mean ± the standard deviation of ΔT_B in Kelvin for AMSU-B channels calculated using ECMWF profiles.

Channel	16	17	18	19	20
mean	0.0004	−0.0348	−0.2031	−0.0075	−0.0268
± std.	±0.0009	±0.0142	±0.0590	±0.0017	±0.0036

3.4.3 Summary of the Ozone Impact

This section describes the results of the study to check whether the weak ozone lines present in the AMSU-B frequency range have any impact on the measured brightness temperatures. Accurate line-by-line radiative transfer calculations are performed using climatological, and re-analysis data to check this impact.

The results indicate that AMSU-B Channel 18 is the most affected, with brightness temperature differences of about 0.5 K. This is a significant difference, equal to the estimated noise equivalent temperature of this channel on the NOAA-16 satellite (Buehler et al., 2004). The difference is not just an offset, but shows a dependence on the channel brightness temperature, the differences being smaller for colder brightness temperatures and larger for warmer brightness temperatures. Therefore bias correction schemes used in NWP will not be able to successfully eliminate the ozone effect by a constant. Channels 17 and 20 are also marginally affected by the ozone lines. Including the ozone lines in RT calculations can give better results while using AMSU-B radiances for NWP or climate applications.

4 A simple method to relate microwave radiances to upper tropospheric humidity

It is shown in Chapter 3 that AMSU-B Channel 18 is sensitive to the upper tropospheric water vapor. In this chapter, a simple method is described to transform the Channel 18 brightness temperature to upper tropospheric humidity (UTH).

The goals of this study are to demonstrate how this method can be applied to AMSU-B data, to explicitly document the transformation coefficients to use, to discuss the method's performance, and to point out limitations. Although the analysis is carried out for microwave data, some of the new findings can also be applied to the more traditionally used infrared data. To keep things simple, only the clear sky case is considered, although the impact of clouds is an important issue for climatological applications (Greenwald and Christopher, 2002), even though the impact of clouds is much less dramatic than in the infrared. Most of the results presented in this chapter are published in John and Buehler (2004b) and Buehler and John (2005).

The results from an initial attempt to derive UTH climatology from AMSU-B data are also briefly explained at the end of this chapter (Section 4.4). This section contains a qualitative comparison of the derived climatology to another UTH climatology derived from infrared data (Soden and Bretherton, 1996). Often, UTH climatologies are made under the assumption that the UTH is normally distributed. A cautionary note on the use of this assumption is also given in this section. This is described in the article by John et al. (2005).

The structure of the chapter is as follows: Section 4.1 introduces the previous work done in this area, Section 4.2 introduces the retrieval

methodology, Section 4.3 presents results and discussion, Section 4.4 describes the initial attempts of deriving UTH climatology, and Section 4.5 includes a summary and conclusions.

4.1 Background

Infrared data at the 6.7 µm channel from geostationary and polar orbiting satellites have been used extensively for deriving UTH. This channel has similar water vapor Jacobian to that of AMSU-B Channel 18. Soden and Bretherton (1993), henceforth referred to as SB, derived a simple relation between infrared radiances and upper tropospheric humidity:

$$\ln(\text{UTH}) = a + b\,T_B\ , \tag{4.1}$$

where ln(UTH) is the natural logarithm of Jacobian weighted mean of the fractional relative humidity in the upper troposphere, T_B is the radiance expressed in brightness temperature, and a and b are constants. The original relation by SB contains also a $\cos(\theta)$ term, where θ is the zenith angle, which was omitted here for simplicity. SB used the radiance Jacobian with respect to relative humidity for the weights in the calculation of UTH.

In the derivation of Equation (4.1), SB made use of a reference pressure and a dimensionless lapse rate parameter. Various later studies made explicit use of these parameters to improve upon the simple relation. An overview on the different variants of the relation used over the years is given by Jackson and Bates (2001). The method of using Equation (4.1) to transform radiances (expressed as brightness temperatures) to UTH will be henceforth referred to as the BT transformation method.

The coefficients a and b are typically determined by linear regression, using a training data set of atmospheric temperature and humidity profiles. To get valid coefficients the data set should capture the atmospheric variability as best as possible. To derive Equation (4.1), SB assumed that the relative humidity and the temperature lapse rate are constant in the upper troposphere, which is not true for realistic pro-

files. Vertical structure will thus lead to violations of Equation (4.1), but the resulting errors will be included in the error analysis, if the error analysis is based on realistic profiles.

The great advantage of the BT transformation method is that radiances and radiance differences can be easily transformed to a more intuitive quantity. It is thus very well suited for climatological studies. A disadvantage at first sight is that the UTH defined as the weighted mean relative humidity of the upper troposphere can not be directly compared to other humidity measurements. In particular, the weights in the definition of UTH depend on the atmospheric state, so a drier atmosphere is sampled at lower altitudes. Retrieved UTH spatial fields are thus not defined strictly at a specific level or layer of the atmosphere. While most UTH observations will lie within a roughly 6–8 km layer or 500–200 hPa layer, this is not guaranteed for all cases. This is illustrated in Figure 4.1 which compares the Jacobian weighted relative humidity and the averaged humidity between 500–200 hPa. The left panel is for profiles from 60° S to 60° N and the right panel is for the tropics, where the two definitions of UTH match fairly well. In the left panel, there are a lot of cases in which the Jacobian weighted UTH is larger than the averaged UTH for the 500–200 hPa layer. This is because, in the mid-latitudes the Jacobian peaks in the lower layer of the atmosphere, where the relative humidity is higher. Note that some authors defined UTH as the 500–200 hPa averaged relative humidity (Houshangpour et al., 2005; Jimenez et al., 2005).

The difficulty of comparing the Jacobian weighted UTH with other humidity data sets can be overcome by doing the comparison in the proper way, which is to use a radiative transfer model to simulate radiances for all humidity data sets to be compared, and then use the transformation of Equation (4.1) to map the radiance differences back to UTH differences.

Quite a number of studies have used the BT transformation method to transform infrared radiances into UTH (Escoffier et al., 2001; Tian et al., 2004; Bates and Jackson, 2001; Soden et al., 2004), including a recent study on humidity supersaturation with respect to ice as seen by the High Resolution Infrared Sounder (HIRS) (Gierens et al., 2004). For microwave sensors, on the other hand, the method has not

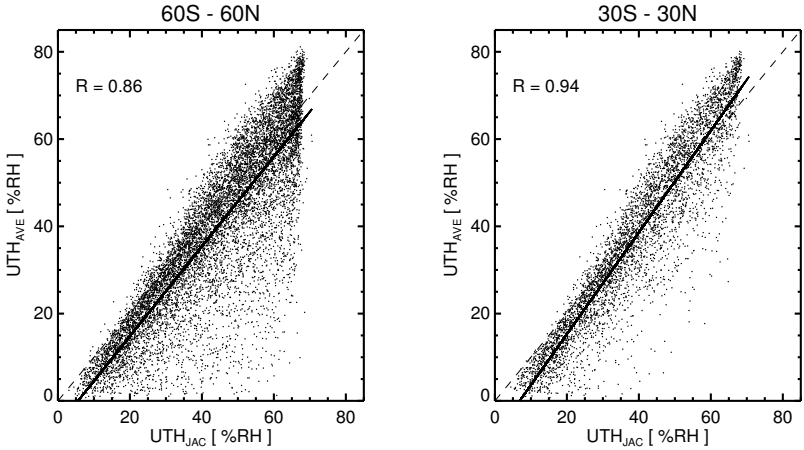

Figure 4.1: Averaged relative humidity between 500–200 hPa versus the Jacobian weighted relative humidity. The left panel shows this comparison for profiles from 60°S–60°N and the right panel shows it only for the tropics. The ECMWF data which is used here is described in Section 4.2.1. The sharp cutoff in UTH at 70 %RH is due to the simple cloud microphysics in the ECMWF model, which does not allow any supersaturation with respect to ice. A 70 %RH with respect to water corresponds approximately to 100 %RH with respect to ice for typical upper tropospheric temperatures.

been much used. While there are many publications about microwave humidity profile retrieval, for example, (Wilheit, 1990; Engelen and Stephens, 1999; Rosenkranz, 2001; Sohn et al., 2001), there appear to be only three publications using the BT transformation method.

The first to have used it for microwave data appears to be Spencer and Braswell (1997), who applied the method to data from the Special Sensor Microwave humidity sounder (SSM/T2) in order to study the UTH in the subtropical subsidence zones. They used simulated radiances for radiosonde data from one tropical station to determine the parameters a and b in Equation (4.1), but neither give the values of a and b, nor a detailed error analysis for the derived UTH, since the focus of the article is on the application rather than on the methodology. Engelen and Stephens (1998) published a study comparing HIRS and SSM/T2 UTH derived by the BT transformation method. They used a

regression on radiances generated for the TOVS Initial Guess Retrieval (TIGR-3) data set (Chaboureau et al., 1998) to determine a and b. Compared to Spencer and Braswell (1997) there is a more detailed error analysis, but also no explicit values for a and b. Finally, Greenwald and Christopher (2002) used the BT transformation method in their analysis of the effect of cold clouds on UTH derived from the AMSU-B. Since their main focus is on clouds, there is not much discussion on the BT transformation method, but at least the values $a = 20.95$ and $b = -0.089\,\mathrm{K}^{-1}$ are given for the transformation coefficients.

4.2 Methodology

This section describes the atmospheric data sets used for determining regression coefficients and for validation, the radiative transfer model setup and the regression method.

4.2.1 Atmospheric Data Sets

Two different data sets of atmospheric temperature and humidity vertical profiles were used in this study to determine the transformation parameters a and b: the TOVS Initial Guess Retrieval (TIGR-3) data set and the 60-level sampled ECMWF data set.

The TIGR-3 data set (Chaboureau et al., 1998) consists of approximately 2000 radiosonde profiles from all climate zones and seasons, selected to cover as much as possible the range of atmospheric temperature and humidity variability. The 60-level sampled ECMWF data set (Chevallier, 2001) consists of 13495 atmospheric profiles of temperature, water vapor, and ozone. The profiles are sampled in such a way that the atmospheric variability is covered as much as possible, making the data set suitable for regression applications. Some profiles which have water vapor volume mixing ratio values less than 10 ppb were excluded from the calculation.

A third independent data set, consisting of 2 years (2001–2002) of quality controlled radiosonde data (Leiterer et al., 1997) from station Lindenberg, was used for validation. For this data set co-located AMSU

measurements were identified with the procedure described in detail in Buehler et al. (2004), hereafter referred to as BKJ.

4.2.2 Radiative Transfer Model

The ARTS model was used to simulate radiances for all profiles in the TIGR-3 and ECMWF data sets. Not only nadir radiances were simulated, but also off-nadir radiances corresponding to all AMSU-B viewing angles. Required geophysical inputs of the model in this case are humidity and temperature profiles, the surface skin temperature, and the surface emissivity. Humidity and temperature profiles were taken from the data sets. The skin temperature was assumed to be equal to the lowest atmospheric temperature. For the TIGR-3 data set the surface emissivity was set to 0.95, for the ECMWF data set it was set to 0.95 for land and to 0.6 for sea. The surface emissivity influences mainly the window Channels 16 and 17, but under extremely dry conditions also the sounding Channels 18 to 20.

As a rough filter against such extreme conditions, for which Equation (4.1) is not valid, profiles were discarded if the brightness temperature of Channel 20 (T_B^{20}) was not warmer than that of Channel 18 (T_B^{18}). For the simulated clear-sky radiances this occurs only when both channels see the surface, mostly at high latitudes or for high mountains. For all other cases T_B^{20} is warmer than T_B^{18} because its emission comes from lower altitudes in the troposphere. (For real AMSU data the condition $T_B^{20} < T_B^{18}$ can also be used as an indicator of strong convective cirrus clouds, as described by Burns et al. (1997).)

The ARTS model was not only used to calculate radiances, but also to calculate the associated Jacobians

$$K_j^{18}(\theta) = \frac{\partial T_B^{18}(\theta)}{\partial x_j} \,, \tag{4.2}$$

where j is the vertical grid index, ∂ indicates a partial derivative, and x_j is the water vapor volume mixing ratio (VMR) in fractional units

$$x_j = \frac{\mathrm{VMR}_j^{\mathrm{H_2O}}}{\mathrm{VMR}_j^{\mathrm{Ref}}} \,. \tag{4.3}$$

The $\mathrm{VMR}_j^{\mathrm{Ref}}$ are identical to the profile for which the Jacobian is calculated. This type of Jacobian shows the sensitivity of T_B to relative changes in the humidity VMR at each vertical gridpoint. The profile is assumed to be piecewise linear between the gridpoints. The grid used is equidistant in the logarithm of the pressure, hence approximately equidistant in altitude. Some example Jacobians for AMSU Channels 18 to 20 are shown in Figure 3.4. Because the Jacobians depend strongly on the atmospheric conditions, the figure shows them separately for a tropical atmosphere and a midlatitude winter atmosphere. Channel 18 peaks around 8.5 km for the tropical atmosphere and around 6 km for the midlatitude winter atmosphere. Channels 19 and 20 peak at lower altitudes.

4.2.3 Regression Method

UTH is defined as

$$\mathrm{UTH}(\theta) = \frac{\sum_j K_j^{18}(\theta)\,\mathrm{RH}_j}{\sum_j K_j^{18}(\theta)} \,, \tag{4.4}$$

where RH_j is the relative humidity at altitude level j. The relative humidity is with respect to liquid water where nothing else is explicitly stated. All altitudes between the surface and 10 hPa are used, although only upper tropospheric altitudes contribute significantly. Note that the UTH defined in this way depends not only on the atmospheric state, but also on the instrument viewing angle, since the Jacobian moves to higher altitudes for off-nadir views, as demonstrated by Figure 4.2. For off-nadir views the instrument simply sees emissions from higher up in the atmosphere.

The UTH values calculated in this way and the simulated radiances were used to determine the parameters a and b of Equation (4.1) by a simple linear regression. This was done separately for each instrument viewing angle.

Let $\Delta\mathrm{UTH}$ be the difference between fitted UTH and true UTH:

$$\Delta\mathrm{UTH} = \mathrm{UTH}_{\mathrm{fitted}} - \mathrm{UTH}_{\mathrm{true}} \,, \tag{4.5}$$

then the mean value $\overline{\Delta\mathrm{UTH}}$ of $\Delta\mathrm{UTH}$ is denoted as the retrieval bias

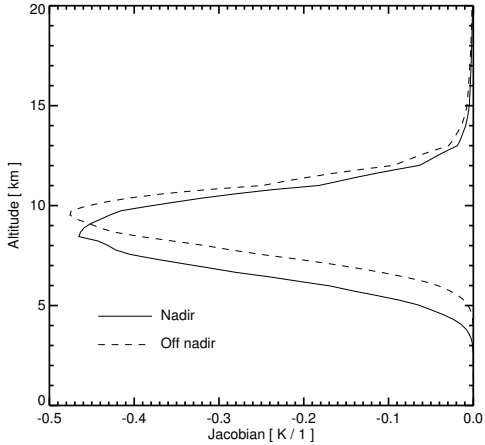

Figure 4.2: AMSU-B Channel 18 midlatitude-summer Jacobians for nadir (solid) and 48.95 ° viewing angle (dashed). The latter is the most off-nadir AMSU-B view. The atmospheric scenario is from Anderson et al. (1986).

and the standard deviation $\sigma_{\Delta\mathrm{UTH}}$ of ΔUTH as the retrieval standard deviation. Similarly, relative retrieval bias and relative retrieval standard deviation are defined based on the relative difference between fitted and true UTH:

$$\Delta\mathrm{UTH}_{\mathrm{rel}} = \frac{\mathrm{UTH}_{\mathrm{fitted}} - \mathrm{UTH}_{\mathrm{true}}}{\mathrm{UTH}_{\mathrm{true}}} \,. \tag{4.6}$$

4.3 Results and Discussion

This section presents and discusses the regression results and their validation. Furthermore, it explores the potential use of these data for supersaturation studies.

4.3.1 Regression Results

Figure 4.3 shows nadir ln(UTH) versus T_B^{18} for the TIGR-3 data set (left) and the ECMWF data set (right). It shows that Equation (4.1) holds very well and that the regression coefficients for the two com-

pletely independent data sets are very close. The coefficients for the TIGR-3 data set are $a = 16.50 \pm 0.19$ and $b = -0.0708 \pm 0.0007\,\mathrm{K}^{-1}$. For the ECMWF data set the coefficients are $a = 16.47 \pm 0.06$ and $b = -0.0702 \pm 0.0002\,\mathrm{K}^{-1}$. These coefficients are different from the ones reported by Greenwald and Christopher (2002), which is probably due to these authors using a different UTH definition. No details are given in the article, but it is likely that they use relative humidity Jacobians, like SB, whereas fractional water vapor VMR Jacobians are used in this study, as described in Section 4.2.2.

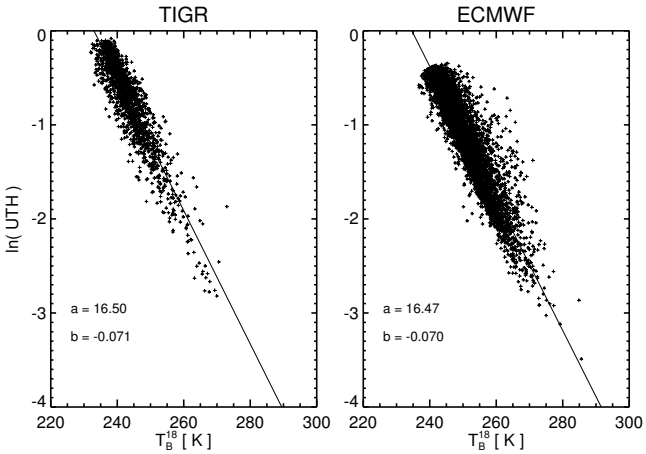

Figure 4.3: Logarithm of nadir UTH versus nadir T_B^{18} for the TIGR-3 data set (left) and the ECMWF data set (right).

The ECMWF parameters have lower errors due to the larger regression data set. To give an impression of the retrieval performance, Figure 4.4 shows fitted UTH versus true UTH for both data sets. No artificial radiometric noise was added, therefore the figure shows the pure regression noise $\sigma_{\mathrm{UTH}}(\mathrm{regr})$. The source of this noise are variations in the vertical structure of the atmosphere, which lead to small deviations from Equation (4.1).

The overall retrieval bias is very small, −1 %RH for the TIGR-3 data set and −0.5 %RH for the ECMWF data set. The overall retrieval standard deviation without radiometric noise is 9 %RH for the TIGR-3

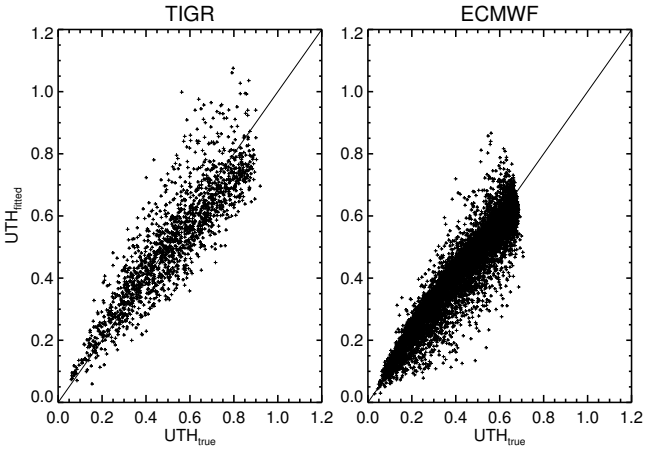

Figure 4.4: Fitted nadir UTH versus true nadir UTH for the TIGR-3 data set (left) and the ECMWF data set (right). No artificial noise was added. Only nadir T_B^{18} were used for the regression. UTH is given in fractional units relative to liquid water.

data set and 5 %RH for the ECMWF data set. With added radiometric noise of 1 K standard deviation, a realistic number for Channel 18, the retrieval standard deviation increases to 10 %RH and 7 %RH, respectively. The bias is not significantly affected by added radiometric noise.

As a safety check, retrieval errors for the ECMWF data set were also calculated for the regression coefficients derived from the TIGR-3 data set. This did not significantly affect the standard deviation, but increased the bias to −5.6 %RH. This shows that there is some hidden a priori information in the training data set that can affect the true retrieval bias. It is planned to investigate this issue in more detail in a dedicated study, using artificially generated training data sets with known statistics.

Other authors, such as Soden and Bretherton (1996) and Greenwald and Christopher (2002) have used a normalized reference pressure in Equation (4.1), so that it becomes

$$\ln(p_0\,\mathrm{UTH}) = a + b\,T_B\ , \tag{4.7}$$

where p_0 is defined as the pressure of the 240 K isotherm divided by 300 hPa. Quite surprisingly, the introduction of p_0 leads to no improvement for the case with ECMWF data without radiometric noise, but, on the contrary, increased the overall retrieval bias to −10.1 %RH and the overall retrieval standard deviation to 9.8 %RH. The reason for a greater error is that the fractional water vapor VMR Jacobian is used to define UTH, which seems to represent the true sampling altitude better than the relative humidity Jacobian used by other authors. To confirm this, the analysis was repeated for UTH based on relative humidity Jacobians. This increased the overall retrieval bias to −1.4 %RH and the overall retrieval standard deviation to 7 %RH, without radiometric noise. However, adding the reference pressure in that case decreased the bias to 1 %RH and the standard deviation did not change significantly. Thus, the retrieval of UTH based on the fractional water vapor VMR Jacobian without reference pressure works better than the more traditional retrieval of UTH based on the relative humidity Jacobian with reference pressure.

The ECMWF data set is so large that one can look at the retrieval performance in more detail. For example, Figure 4.5 displays the bias and the standard deviation (with and without radiometric noise) as a function of $\mathrm{UTH}_{\mathrm{true}}$. The top plot shows the absolute quantities, the bottom plot the relative quantities. The figure shows that both the bias and the standard deviation depend on the UTH value. Positive bias does not exceed 2 %RH for UTH values below 45 %RH, and negative bias does not exceed −4 %RH for UTH values above 45 %RH. Radiometric noise does not affect the bias, only the standard deviation. The standard deviation without radiometric noise $\sigma_{\mathrm{UTH}}(\mathrm{regr})$ increases from 2 %RH at a UTH of 5 %RH to 5 %RH at a UTH of 25 %RH, from where on it stays approximately constant. The effect of radiometric noise scales with the UTH value. One can see this easily from the law of error propagation. Applied to the BT transformation method the law is

$$\begin{aligned} \sigma_{\Delta\mathrm{UTH}}(\mathrm{radiometric}) &= \sqrt{\left(\frac{\partial\,\mathrm{UTH}}{\partial\,T_{\mathrm{B}}}\right)^2 \sigma_{T_{\mathrm{B}}}^2} \\ &= |b|\ \mathrm{UTH}\,\sigma_{T_{\mathrm{B}}}\,, \end{aligned} \tag{4.8}$$

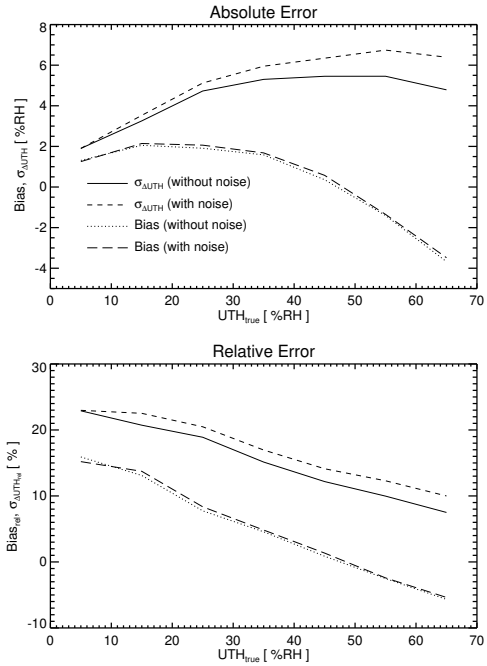

Figure 4.5: Retrieval performance as a function of true UTH for the ECMWF data set. The top plot shows absolute quantities, the bottom plot relative quantities. Displayed are the retrieval standard deviation with and without radiometric noise (dashed and solid), as well as the retrieval bias with and without radiometric noise (long dashed and dotted).

where σ_{T_B} is the radiometric noise.

It is also interesting to study the retrieval performance as a function of latitude and season. Figure 4.6 shows bias and standard deviation (with and without radiometric noise) as a function of latitude for JJA (June-July-August) and DJF (December-January-February). It has to be noted that these are the statistics for the ECMWF regression data set, which are not necessarily the same as for a true climatology. Zonally averaged Jacobian weighted UTH values for this data set (not shown) have maxima of 40–50 %RH in the ITCZ and 50–60 %RH at mid latitudes, and minima of 30–40 %RH in the subtropics. Bearing

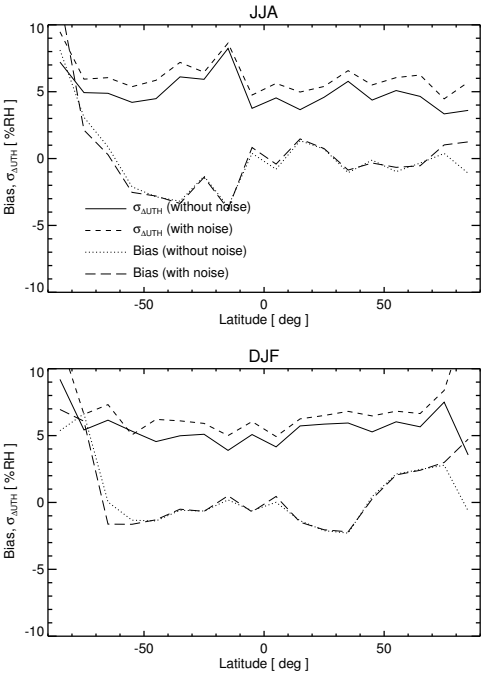

Figure 4.6: Retrieval performance as a function of latitude for the period June to August (top) and December to February (bottom). Displayed are the retrieval standard deviation with and without radiometric noise (dashed and solid), as well as the retrieval bias with and without radiometric noise (long dashed and dotted). Latitude bins of 10° were used for this analysis.

this in mind, it can be seen that the retrieval quality displayed in Figure 4.6 is consistent with Figure 4.5.

Overall, there is very little latitudinal and seasonal dependence, except for a significant bias increase in the polar regions, particularly near the south pole in the southern winter. This can be explained by surface effects due to the extremely dry atmospheric conditions, which apparently are not completely removed by the $T_{\mathrm{B}}^{18} < T_{\mathrm{B}}^{20}$ filter. Furthermore, it should be noted that polar conditions are not well represented in the regression data set, because there are less than 100 polar profiles after applying the surface filter.

Judged by Figure 4.6 there is no need to include latitude depen-

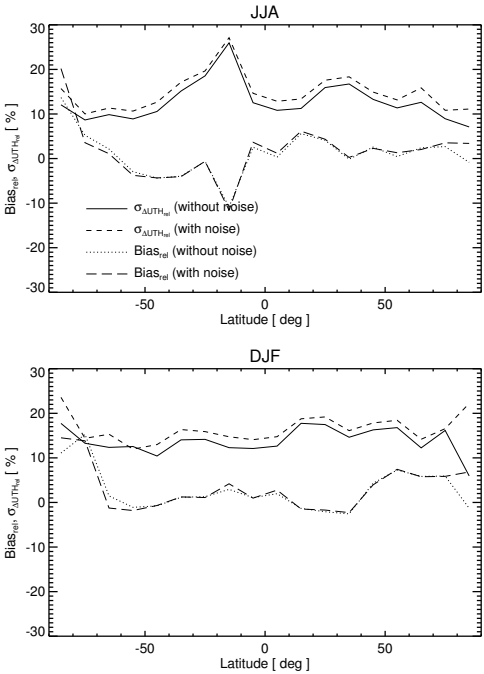

Figure 4.7: Relative retrieval performance as a function of latitude for the period June to August (top) and December to February (bottom). Displayed are the relative retrieval standard deviation with and without radiometric noise (dashed and solid), as well as the relative retrieval bias with and without radiometric noise (long dashed and dotted).

dent parameters in Equation (4.1). One may wonder whether this conclusion also holds for the relative performance, particularly in the subtropical dry zones. Figure 4.7 addresses this question. It shows the same results as Figure 4.6, but for the relative performance parameters, and confirms that the relative retrieval standard deviation increases only slightly in the subtropics.

The discussion so far was only about nadir UTH and nadir T_B^{18}. For off-nadir viewing angles the regression result changes. The solid line in Figure 4.8 shows the dependence of the offset coefficient a on the

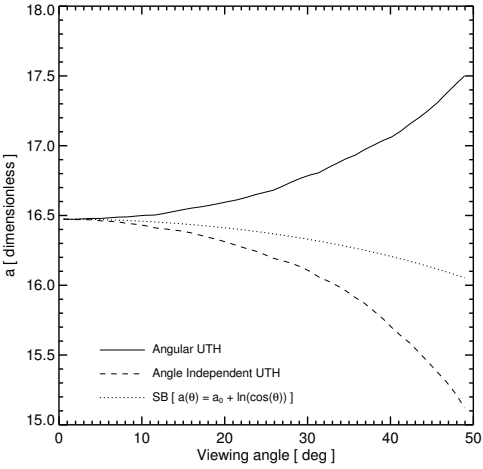

Figure 4.8: The offset parameter a of Equation (4.1) as a function of viewing angle for the ECMWF data set. The solid line is the regression result for an angle dependent UTH, the dashed line is the regression result for an angle independent UTH, and the dotted line is the theoretical angular dependence derived by SB.

viewing angle θ. The original form of Equation (4.1) in SB is

$$\ln\left(\frac{\text{UTH}}{\cos(\theta)}\right) = a + b\,T_{\text{B}} \tag{4.9}$$

or

$$\ln(\text{UTH}) = a + ln(\cos(\theta)) \;+\; b\,T_{\text{B}}\;, \tag{4.10}$$

which would mean that a would have the angular dependence

$$a(\theta) = a_0 + ln(\cos(\theta))\;. \tag{4.11}$$

This curve is also indicated as a dotted line in Figure 4.8. Interestingly, the angular dependence of Equation (4.11) is opposite from the one obtained from the regression. The solution to this puzzle is that SB did not use an angle dependent UTH. If the regression is repeated for $\ln(\text{UTH}(\theta = 0))$ versus T_{B}^{18}, an angular dependence closer to the one derived by SB is obtained, which is displayed as a dashed line in Figure 4.8.

Figure 4.9 shows the result of a similar analysis for the slope parameter b. The b for an angle dependent UTH also behaves opposite to the b for an angle independent UTH. According to the original SB relation b should not have an angular dependence at all, as can be seen from Equation (4.10).

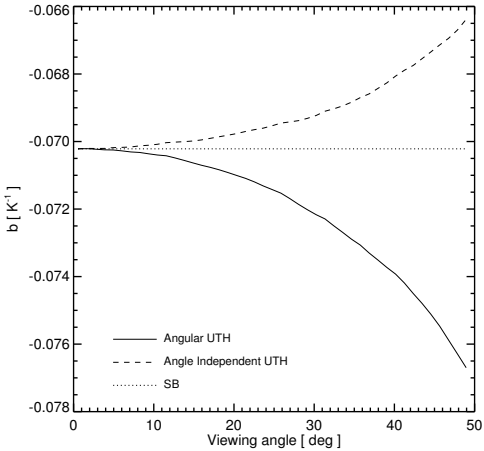

Figure 4.9: The slope parameter b of Equation (4.1) as a function of viewing angle for the ECMWF data set. The solid line is the regression result for an angle dependent UTH, the dashed line is the regression result for an angle independent UTH, and the horizontal dotted line is the theoretical angular dependence derived by SB.

From a user point of view it is preferable to have an angle independent UTH, since this depends only on the atmospheric state and not on the instrument. However, since the instrument is sampling higher altitudes for off-nadir views, angle independent UTH will have higher errors for these views, because the Jacobian used in the UTH definition does not match the actual Jacobian for the off-nadir view. Figure 4.10 shows that indeed the bias and standard deviation for angle independent UTH increase with increasing nadir viewing angle, whereas the bias and standard deviation for angle dependent UTH are approximately constant. Explicit values for the transformation parameters a

and b for the ECMWF data set are given in Table 4.1. It contains the parameters for UTH with respect to liquid water and ice.

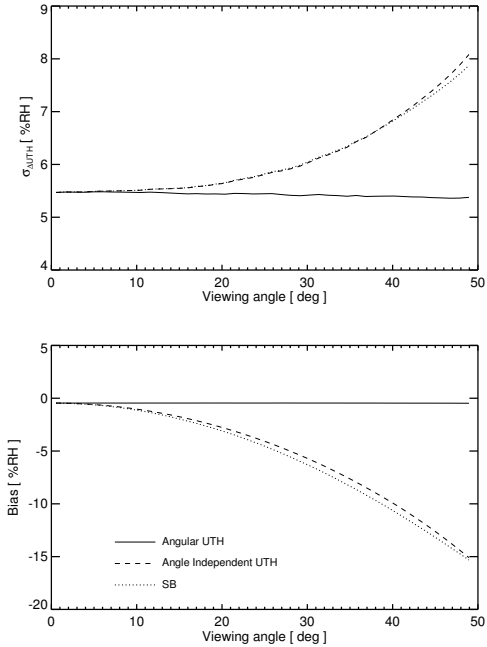

Figure 4.10: UTH retrieval performance for the ECMWF data set as a function of viewing angle. No artificial radiometric noise was added, so this is the pure regression noise. The top panel shows the retrieval error and the bottom panel shows the retrieval bias. The cases shown are: using the regression result for angle dependent UTH (solid), using the regression result for angle independent UTH (dashed), and using the default angular dependence from SB for an angle independent UTH (dotted).

Table 4.1: Transformation parameters derived from the ECMWF data set for each AMSU-B viewing angle for UTH with respect to liquid water (a_w, b_w) and ice (a_i, b_i).

θ [°]	a_w	b_w [K^{-1}]	a_i	b_i [K^{-1}]
0.55	16.474	−0.0702169	18.341	−0.0764737
1.65	16.472	−0.0702106	18.339	−0.0764688
2.75	16.476	−0.0702271	18.342	−0.0764834
3.85	16.479	−0.0702456	18.345	−0.0764992
4.95	16.479	−0.0702506	18.344	−0.0765034
6.05	16.483	−0.0702774	18.348	−0.0765274
7.15	16.488	−0.0703084	18.353	−0.0765550
8.25	16.490	−0.0703243	18.354	−0.0765713
9.35	16.496	−0.0703634	18.359	−0.0766039
10.45	16.501	−0.0703988	18.363	−0.0766340
11.55	16.503	−0.0704219	18.362	−0.0766454
12.65	16.514	−0.0704853	18.371	−0.0766984
13.75	16.527	−0.0705569	18.381	−0.0767557
14.85	16.540	−0.0706315	18.391	−0.0768198
15.95	16.552	−0.0707031	18.401	−0.0768812
17.05	16.561	−0.0707656	18.407	−0.0769315
18.15	16.572	−0.0708374	18.416	−0.0769950
19.25	16.585	−0.0709191	18.426	−0.0770628
20.35	16.599	−0.0710062	18.436	−0.0771351
21.45	16.612	−0.0710919	18.448	−0.0772143
22.55	16.628	−0.0711956	18.462	−0.0773052
23.65	16.649	−0.0713153	18.478	−0.0774066
24.75	16.665	−0.0714210	18.490	−0.0774960
25.85	16.681	−0.0715289	18.503	−0.0775902
26.95	16.709	−0.0716877	18.525	−0.0777226
28.05	16.740	−0.0718609	18.552	−0.0778808
29.15	16.766	−0.0720197	18.575	−0.0780199
30.25	16.789	−0.0721669	18.592	−0.0781414
31.35	16.806	−0.0722922	18.605	−0.0782481
32.45	16.842	−0.0724969	18.637	−0.0784375
33.55	16.874	−0.0726909	18.664	−0.0786102
34.65	16.907	−0.0728922	18.695	−0.0787986
35.75	16.932	−0.0730668	18.715	−0.0789501
36.85	16.972	−0.0733017	18.750	−0.0791631
37.95	17.003	−0.0735100	18.778	−0.0793542
39.05	17.036	−0.0737274	18.805	−0.0795464
40.15	17.063	−0.0739261	18.823	−0.0797062
41.25	17.105	−0.0741909	18.859	−0.0799444
42.35	17.156	−0.0745019	18.901	−0.0802151
43.45	17.201	−0.0747932	18.940	−0.0804762
44.55	17.252	−0.0751160	18.983	−0.0807632
45.65	17.308	−0.0754690	19.031	−0.0810812
46.75	17.375	−0.0758780	19.088	−0.0814447
47.85	17.439	−0.0762869	19.142	−0.0818039
48.95	17.501	−0.0766990	19.195	−0.0821763

4.3.2 Validation

Co-locations of radiosondes and AMSU measurements can be used to validate the retrieved UTH. Two years (2001–2002) of co-locations for the radiosonde station Lindenberg and the NOAA-15 and NOAA-16 satellites were used for this purpose. They are described in detail in BKJ. Co-locations where the measured T_B^{18} was not colder than T_B^{20} were discarded in order to screen out cases with a significant surface contribution, as described in Section 4.2.2. Furthermore, cases with $T_B^{20} < 260\,\mathrm{K}$ were discarded as a rough filter against clouds, as described in BKJ. No other filters were applied. Figure 4.11 shows a scatter plot of retrieved $\mathrm{UTH_{AMSU}}$ versus in-situ $\mathrm{UTH_{sonde}}$. The $\mathrm{UTH_{sonde}}$ was derived by calculating an AMSU-B Jacobian weighted mean of the relative humidity according to Equation (4.4). The standard deviation of the difference between the two is 7 %RH, the standard deviation of the relative difference is 18%. These values are in good agreement with the absolute and relative standard deviation from the ECMWF regression with added radiometric noise, which are 7 %RH and 16%, respectively, for a radiometric noise level of 1 K.

The standard deviations for the validation are expected to be somewhat higher than the ones from the regression, due to the additional noise inevitable in such a comparison. The most important reason for additional noise in the validation is atmospheric inhomogeneity on the 10 km scale. One can estimate this from $\sigma_{50\,\mathrm{km}}$, the standard deviation of the AMSU radiances within a target area of 50 km radius, as discussed in BKJ. The total noise present in the intercomparison between simulated Lindenberg radiosonde radiances and measured AMSU radiances was found in BKJ to have a standard deviation of approximately 1.6 K. Putting this instead of the pure radiometric noise into the error estimate from the regression leads to absolute and relative UTH standard deviations of 8 %RH and 19%, respectively, in close agreement with the standard deviations observed in the validation.

Inspection of Figure 4.11 reveals that the points scatter not perfectly around the diagonal. Rather, $\mathrm{UTH_{AMSU}}$ seems to be higher than $\mathrm{UTH_{sonde}}$ at low UTH and lower than $\mathrm{UTH_{sonde}}$ at high UTH. To quantify this, one can fit a straight line to the data. However, the fit should

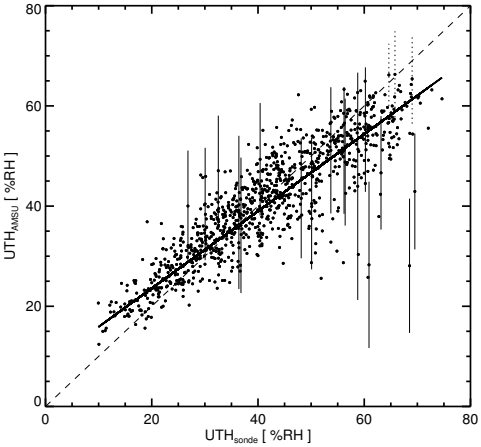

Figure 4.11: $\mathrm{UTH_{AMSU}}$ measured by AMSU versus $\mathrm{UTH_{sonde}}$ measured by radiosonde. Some example error bars are also shown only for highly inhomogeneous (solid vertical lines) and homogeneous (dotted vertical lines) cases to avoid clutter. The straight dashed line is the diagonal, the straight solid line the result of a least-square fit taking into account the varying error bars.

take into account the varying error bars for each co-location. An error model,

$$\sigma_{\Delta\mathrm{UTH}}(\mathrm{inhom}) = |b|\ \mathrm{UTH}\ \ (0.5\,\mathrm{K} + \sigma_{50\mathrm{km}})\ , \tag{4.12}$$

is used in analogy to Equation (4.8), just replacing the radiometric noise by the error model derived in BKJ. This error is a measure for the uncertainty in the co-location. It is important to take it into account because it has a large variability. Figure 4.11 shows some sample error bars of $\sigma_{\Delta\mathrm{UTH}}(\mathrm{inhom})$. Note that this is not an error of the AMSU UTH itself, but a consequence of our inability to do a perfect co-location. The fit result is also shown in Figure 4.11. The parameters obtained are

$$\mathrm{UTH_{AMSU}} = 8.2\,\%\mathrm{RH}\ \ + 0.77\,\mathrm{UTH_{sonde}}\ . \tag{4.13}$$

The non-unity slope can be explained by a combination of three factors. Factor one is that the radiosondes seem to underestimate the

UTH for very dry conditions, as shown in BKJ. Factors two and three are that the BT transformation method overestimates UTH for dry conditions and underestimates UTH for very moist conditions, as shown by Figure 4.5. All three factors act to decrease the slope of the fitted line. Taking this into account one can say that the agreement is quite reasonable. Particularly, there is no evidence for an overestimation of UTH for moist conditions due to cloud contamination.

The reasonable agreement between Lindenberg radiosondes and AMSU UTH gives some confidence that the BT transformation method works well for microwave data. It would be desirable to do this kind of comparison also for other radiosonde stations, in particular for stations in other climate zones. Such comparisons are planned. However, they can be regarded as an investigation of the quality of the radiosonde data, rather than a validation of the BT transformation method, due to the rather poor quality of the global radiosonde data record of the upper troposphere (SPARC, 2000).

4.3.3 Supersaturation

Regions in the upper troposphere where the humidity concentration is supersaturated with respect to ice have received some attention recently (Gierens et al., 1999; Spichtinger et al., 2002; Buehler and Courcoux, 2003). Can the BT transformation method be used to study the frequency of occurrence of supersaturation? Figure 4.12 shows histograms of UTH values, in this case with respect to ice, for the ECMWF data set. The reference to ice instead of liquid water is denoted with a subscript 'i'. UTH_i values above 100 %RH_i are supersaturated. The 'true' UTH_i does not show any supersaturation. This is no surprise, since all profiles were taken from ECMWF analyses, which do not have any supersaturation due to the simple cloud microphysics in the model. That the ECMWF data does not show ice supersaturation can also be seen from the sharp cutoff in UTH_{true} at 70 %RH in the right plot of Figure 4.4, since 70 %RH corresponds approximately to 100 %RH_i for typical upper tropospheric temperatures. (Figure 4.4 shows UTH_{true} values up to 90 %RH for the TIGR-3 data set, so the

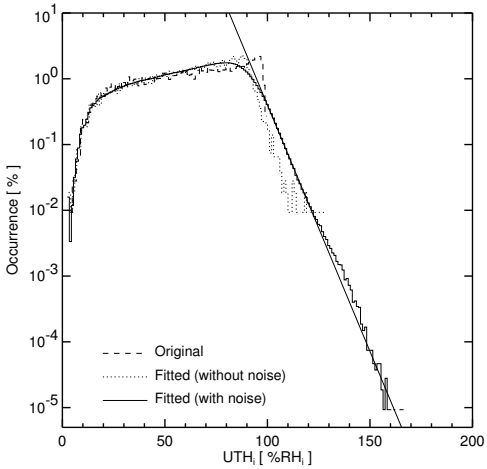

Figure 4.12: Histograms of UTH with respect to ice for the ECMWF data set. Shown are histograms for the true UTH$_i$ (dashed), for the retrieved UTH$_i$ without radiometric noise (dotted), and for the retrieved UTH$_i$ with 1 K radiometric noise (solid). The straight solid line shows an exponential fit to the supersaturated region of the histogram with noise (100 to 130 %RH$_i$). The bin size for the histograms is 1 %RH$_i$.

TIGR-3 data set, which is based on radiosondes, does show ice supersaturation.)

Interestingly, the retrieved UTH$_i$ (dotted curve in Figure 4.12) does show ice supersaturation, due to the regression noise. The apparent ice supersaturation becomes even stronger when realistic radiometric noise of 1 K standard deviation is added (solid curve). For this last curve 1000 different random noise values were added for each ECMWF profile, so the histogram is based on a total of 10^7 UTH$_{\text{fitted}}$ values. This Monte-Carlo-type error analysis method is similar to the one described in detail in Buehler and Courcoux (2003). Although the distribution of the radiometric noise is Gaussian, the supersaturation drop-off is exponential, due to the non-linear mapping by Equation (4.1). Following Buehler and Courcoux (2003) and the earlier study by Spichtinger et al. (2002), one can analyze the frequency of supersaturation quan-

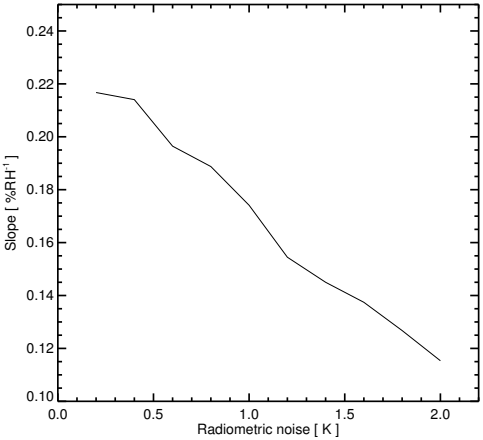

Figure 4.13: The value of the apparent supersaturation drop-off slope B as a function of the assumed radiometric noise standard deviation.

titatively by fitting to the data an exponential of the form

$$p(\mathrm{UTH}_i) = A\, e^{-B\ \mathrm{UTH}_i}\ , \tag{4.14}$$

where $p(\mathrm{UTH}_i)$ is the frequency of occurrence of each supersaturated UTH_i value and A and B are fit coefficients. Such a fit is also displayed in Figure 4.12, the drop-off slope B is $0.17\,\%\mathrm{RH}^{-1}$ for this noise level.

The value of B depends on the assumed radiometric noise level, as demonstrated by Figure 4.13. This figure was generated by repeating the analysis as displayed in Figure 4.12 for different radiometric noise standard deviations in steps of 0.2 K. The higher the radiometric noise, the slower the drop-off, the smaller B. Figure 4.13 can be used to define a detection threshold for true supersaturation: The drop-off slope B for the measured UTH_i must be significantly smaller than the one expected from the radiometric noise.

The slope found by Gierens et al. (2004) from HIRS infrared data is 0.12, whereas the expected slope from an assumed worst case HIRS radiometric noise of 1 K is 0.17, so there would be indeed evidence for ice supersaturation. A devil's advocate would have to postulate a total noise level of 2 K to explain a supersaturation drop-off slope of 0.12 in the absence of real supersaturation. The above arguments assume that

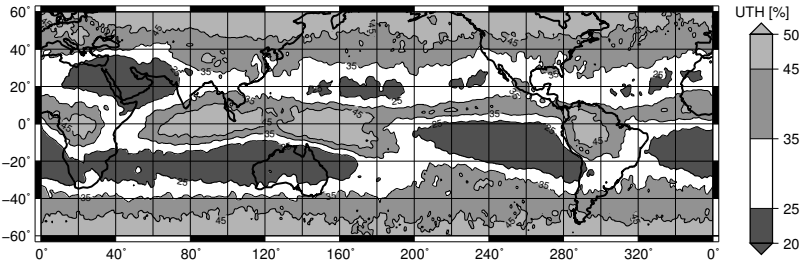

Figure 4.14: A one year (December 2001–November 2002) climatology of UTH derived from AMSU-B Channel 18 brightness temperatures. Data from NOAA-16 were used for this. The brightness temperatures were gridded and averaged for a $1.5° \times 1.5°$ latitude-longitude grid and then transformed to UTH using Equation (4.1). (Figure courtesy of M. Kuvatov.)

our analysis for microwave data is valid also for infrared data. This is of course not strictly true, because the transformation parameters a and b of Equation (4.1) are different. However, the general behavior is expected to be the same. To get the exact numbers, a similar analysis could easily be carried out for infrared data as well.

4.4 UTH Climatology

This section outlines our plans of making a UTH climatology using AMSU-B data. The first step in this direction was to average the AMSU-B data for a specific time period and a latitude-longitude grid. A $1.5° \times 1.5°$ latitude-longitude grid was used for this study. The gridded, averaged brightness temperature was then transformed to UTH using Equation (4.1). As an initial step, the UTH climatology was made just for one year (December 2001–Nov 2002) using AMSU-B data from the NOAA-16 satellite. This is shown in Figure 4.14. Note that UTH here is defined with respect to water.

The UTH map clearly depicts the Hadley circulation patterns with a moist inter tropical convergence zone (ITCZ) and a dry band extending over the subtropics. Moist regions are also observed over the Indo-Pacific warm pool and over monsoonal regions. An 11 year (1981–

1991) climatology of UTH using the HIRS 6.7 μm channel data is shown in Figure 4.15 (Soden and Bretherton, 1996). It can be seen that the two maps show similar features. This indicates that the transformation coefficients given in Table 4.1 are good enough to produce UTH values from AMSU data.

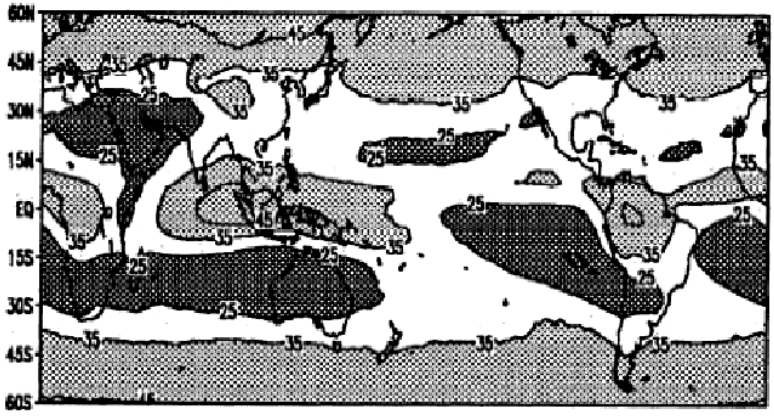

Figure 4.15: 11 years climatology of UTH from HIRS 6.7 μm channel data. (Figure from Soden and Bretherton (1996).)

A noteworthy point is that the climatology using HIRS data was made in such a way that UTH was determined for each day using Equation (4.1) and then averaged over the 11 year period. The transformation coefficients, a and b, used in this case are given in Soden and Bretherton (1996). Where as in the AMSU climatology, brightness temperatures were averaged over one year and then transformed to UTH. One obvious question here is whether these two approaches are equivalent. The results of an attempt to answer this question are given in the next section.

4.4.1 Is UTH of the Mean T_B Equal to the Mean of UTH?

ECMWF reanalysis fields (Kallberg et al., 2004) of temperature and water vapor for one year (December 2001–November 2002) were used to study this problem. The fields are available four times a day (00, 06, 12, and 18 UTC) on a 1.5° × 1.5° latitude-longitude grid and a 60 level vertical grid which ranges from surface to 10 Pa. A fast radiative transfer model, RTTOV-7 (Saunders et al., 1999), was used to generate AMSU-B Channel 18 brightness temperatures from these profiles. Since the atmosphere is transparent in the polar regions and since the ice covered areas of Greenland and Antarctic are elevated, the application of Equation (4.1) to brightness temperature is not valid in those regions (Bates and Jackson, 2001). Therefore our analysis is limited to the latitude band from 60° S to 60° N.

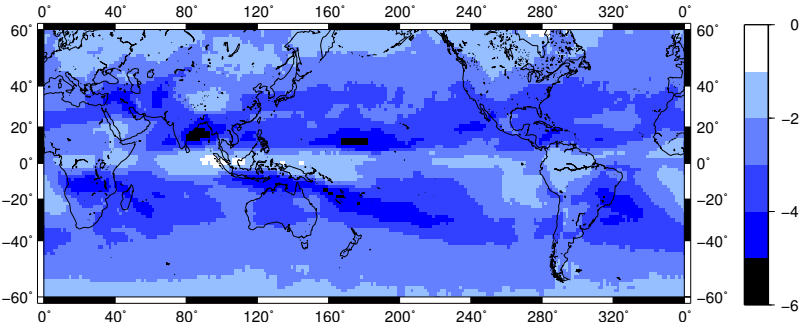

Figure 4.16: Difference between UOM and MOU. Brightness temperatures were simulated using ECMWF profiles for a time period from December 2001 to November 2002. (Figure courtesy of N. Courcoux.)

The UTH climatology is made in two different ways: (1) Brightness temperatures are first averaged and then transformed to UTH using Equation (4.1). Therefore this is the UTH of the mean brightness temperature (UOM). (2) Brightness temperatures are transformed to UTH using Equation (4.1) and the UTH values are then averaged, giving the mean of UTH (MOU). The difference between the two climatologies is

defined as:

$$\begin{aligned} \Delta\text{UTH} &= \text{UTH}(\overline{T_\text{B}}) - \overline{\text{UTH}(T_\text{B})} \\ &= \text{UOM} - \text{MOU}\,, \end{aligned} \tag{4.15}$$

and is shown in Figure 4.16. The difference is negative everywhere on the map and the magnitude of the difference varies from 0 to −6 %RH. There are two main questions to be answered here: (1) Why are the two climatologies different? and (2) Why is the difference always negative? Before answering the questions, it is interesting to note that large differences exist where the variability of the brightness temperature is higher as shown in Figure 4.17. This figure shows the standard deviation of the brightness temperature for the entire time period. One can see a good correlation between the variability of the brightness temperature and the difference in the climatologies.

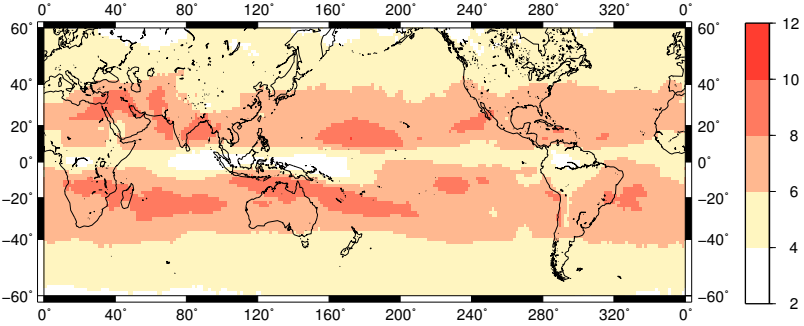

Figure 4.17: The standard deviation of brightness temperature generated using ECMWF profiles for one year (December 2001–November 2002). (Figure courtesy of N. Courcoux.)

4.4.2 A Monte Carlo Approach

In order to study the differences between UOM and MOU, a simple Monte Carlo approach was used. A similar approach was used to study an apparent supersaturation in the upper troposphere due to temperature measurement errors (Buehler and Courcoux, 2003; Buehler and

John, 2005). The Monte Carlo approach enables one to understand the differences quantitatively.

As a first step, AMSU-B Channel 18 brightness temperatures were generated by creating random ensembles of T_B^{18} values representing a Gaussian distribution with a mean at 245 K and standard deviations varying from 1 K to 12 K. Some examples of these brightness temperature distributions are shown in the left panel of Figure 4.18. Each of these random ensembles consists of 10^7 values, in order to make smooth distributions. A mean value of 245 K for Channel 18 brightness temperatures is reported in John and Buehler (2005) for mid-latitude regions. These brightness temperature ensembles can be used to simulate UTH ensembles using Equation (4.1), some examples are shown in the right panel of Figure 4.18.

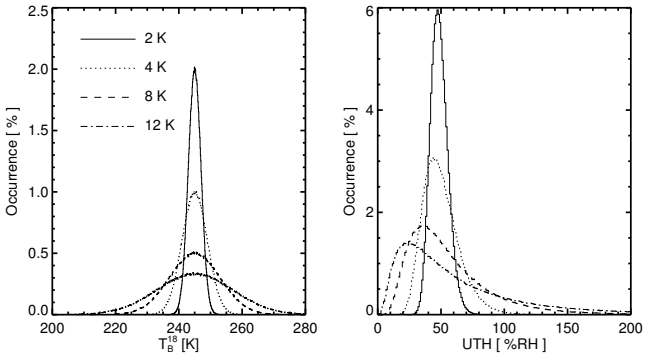

Figure 4.18: Distributions of brightness temperature and UTH. The left panel shows Gaussian distributions of brightness temperatures with a mean of 245 K and four different standard deviations: 2 K (solid line), 4 K (dotted line), 8 K (dashed line), and 12 K (dash-dotted line). The right panel shows UTH distributions for corresponding brightness temperature distributions. Note the log-normal behavior of UTH distributions.

The UTH distributions shown in the right panel of Figure 4.18 do not show a Gaussian behavior, the distributions get more and more right skewed as the standard deviations of the T_B^{18} distributions increases. If Equation (4.1) is closely examined, it is clear that UTH values should behave log-normally, if the T_B^{18} values are normally distributed. Higher

values of UTH occur for colder brightness temperatures. A small decrease in T_B^{18} in the vicinity of the steepest portion of the UTH–T_B^{18} exponential curve will result in a large increase in UTH. As the standard deviation of the T_B^{18} distribution increases, the occurrence of colder brightness temperatures also increases. This results in a large right skewing of the UTH distributions. Note that a log-normal behavior of UTH was reported in Soden and Bretherton (1993). Thus, the means of these distributions are also shifted towards the right, giving a higher value for the mean of UTH.

The reason for the difference between UOM and MOU is the non-Gaussian behavior of the UTH distribution. The differences are always negative due to the right skewed (log-normal) nature of the UTH distribution. It is also clear that the difference will increase if the standard deviation of the T_B^{18} distribution is increased. The solid curve in Figure 4.19 shows the difference as a function of the standard deviation of the T_B^{18} distribution.

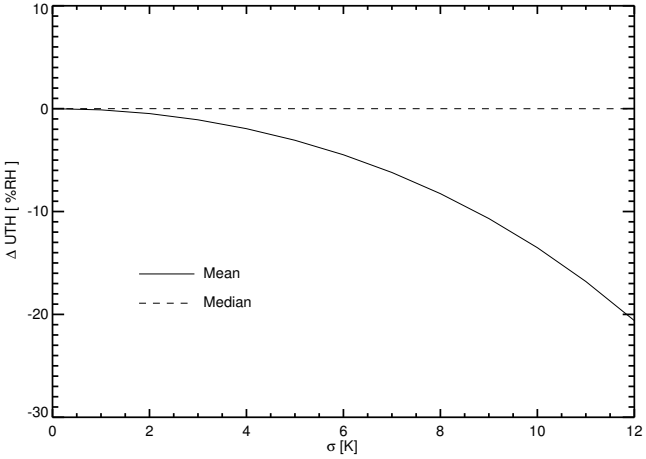

Figure 4.19: The solid line represents the behavior of the difference between UTH of the mean and the mean of UTH and the dashed line represents the difference between UTH of the median and the median of UTH as a function of the standard deviation of the T_B^{18} distribution.

4.4.3 AMSU Data

The differences reach up to −20 %RH for a standard deviation of 12 K. But in the case of ECMWF, as shown in Figure 4.16, the differences were only about −6 %RH for about 12 K standard deviation. This hints at the fact that real AMSU brightness temperatures are not normally distributed as assumed. Real AMSU data have been used to investigate this. Three years (2001–2003) of AMSU data from NOAA-16 satellite were selected for 42 latitude-longitude grid points over Europe. These grid points correspond to some of the radiosonde stations over Europe. The details of the data can be seen in John and Buehler (2005). The distribution of T_B^{18} is shown (solid line) in Figure 4.20.

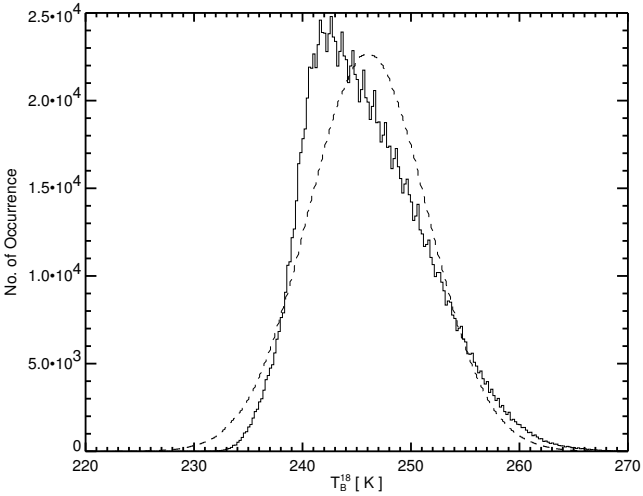

Figure 4.20: Distribution of AMSU-B Channel 18 brightness temperature (solid curve). The data is taken from NOAA-16 satellite for three years (2001–2003). The dashed curve stands for a Gaussian distribution with the same mean and standard deviation of the real data.

There are about 1.5 million data points in the distribution. The T_B^{18} values which are warmer than T_B^{20} (in normal cases, T_B^{18} should be colder than T_B^{20} since Channel 20 is sensitive to the lower troposphere) were discarded as a rough filter against either surface or cloud con-

tamination (Buehler and John, 2005). The mean of this distribution is 246.03 K and the standard deviation is 5.48 K. The minimum brightness temperature is 210.75 K and the maximum is 271.94 K. Note the non-Gaussian nature of the T_B^{18} distribution. A Gaussian distribution (dashed curve) with the same mean and the standard deviation is also shown in Figure 4.20 for a direct comparison. The most important feature is the rare occurrence of very low brightness temperature values in the original T_B^{18} distribution. There are only 117 values which are less 230 K in the original distribution, whereas, there are 2667 values less than 230 K in the Gaussian distribution. The presence of a large number of low brightness temperature values resulted in larger UTH values, thus, ΔUTH was larger when a Gaussian T_B^{18} distribution was assumed. This explains why ΔUTH in Figure 4.16 is smaller than that predicted by the Monte Carlo method.

The brightness temperature values shown in Figure 4.20 correspond to all possible viewing geometries of the AMSU-B instrument. Therefore it is not possible to transform all of them to UTH by a single pair of a and b values in Equation (4.1). Figure 4.21 shows the distributions of T_B^{18} and UTH, only for two viewing angles: the nadir and the maximum off-nadir (48.5°). There are 43048 nadir brightness temperatures and 20650 maximum off-nadir brightness temperatures. The reason of the difference in number for the nadir and the maximum off-nadir viewing angles is that the pixels were selected from a target area of fixed size around each latitude-longitude grid point, but pixel size at the off-nadir viewing angle is more than the double of that at nadir. The mean and the standard deviation of the nadir and off-nadir T_B^{18} distributions are 247.63 and 240.58 K and 5.22 and 4.74 K, respectively. The difference between UOM and MOU is -2.54 %RH for the nadir and -2.41 %RH for the maximum-off nadir viewing angles. Therefore the difference between UOM and MOU can be also observed using the real AMSU-B data. This is also true for the other viewing angles where ΔUTH is about -2.5 %RH. These numbers are consistent with the results from the ECMWF data, for example, over northern mid-latitudes the standard deviation values are about 5 K (see Figure 4.17).

It should be noted that Soden and Bretherton (1993) also reported a log-normal behavior for UTH (see Figure 16 of their article), and a

physical explanation was also given by them making use of a reference model of water vapor transport. Interestingly, we do not find a large log-normal behavior in the UTH distributions, at least over the mid-latitude region. This is an important point for further investigation, but it is beyond the scope of this study.

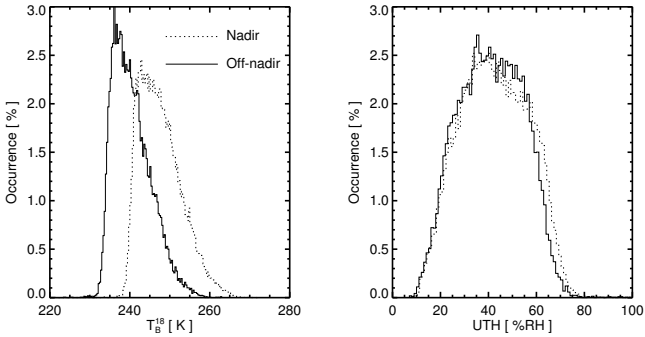

Figure 4.21: Distributions of AMSU-B Channel 18 brightness temperature and the transformed UTH values. Distributions are shown only for the nadir (dotted line) and the maximum off-nadir (solid line) angles to avoid clutter.

4.4.4 Can the Median Do a Better Job?

In the previous sections it was demonstrated that the use of the arithmetic mean to describe the central tendency of non-Gaussian distributions can introduce spurious errors due to the non-resistant nature of the mean. It is well-known that the normal arithmetic mean is not a good parameter to describe the central tendency of a non-Gaussian distribution (Lanzante, 1996). The performance of the simplest robust estimator, the median, as suggested by Lanzante and Gahrs (2000) was tested. The dashed line in Figure 4.19 shows the difference between UTH of the median and the median of UTH versus the standard deviation. In contrast to the difference of UOM and MOU, this is zero and shows no deviation with increase in standard deviation. This is due to the monotonic mapping of T_B^{18} to UTH. Thus the use of median solves the discrepancy of using UOM and MOU.

4.5 Summary and Conclusions

The properties of the BT transformation method applied to microwave data were investigated. The method can be used to retrieve Jacobian weighted upper tropospheric humidity (UTH) in a broad layer centered roughly between 6 and 8 km altitude. Retrieval results are sensitive to the type of Jacobian used to define UTH. It was found that the retrieval of UTH based on the fractional water vapor VMR Jacobian works better than the more traditional retrieval of UTH based on the relative humidity Jacobian, and that the new UTH definition does not need a reference pressure in the regression relation.

The UTH bias is always below 4 %RH, where the largest values are found for high humidity cases. The UTH relative bias is always below 20%, where the largest values are found for low humidity cases. The UTH standard deviation is between 2 and 6.5 %RH in absolute numbers, or between 10 and 27% in relative numbers. The standard deviation is dominated by the regression noise, resulting from vertical structure not accounted for by the simple transformation relation. The part of the UTH error resulting only from radiometric noise scales with the UTH value and has a relative standard deviation of approximately 7% for a radiometric noise level of 1 K. The UTH retrieval performance was shown to be of almost constant quality for all viewing angles and latitudes, except for problems at high latitudes due to surface effects.

A comparison of AMSU UTH and radiosonde UTH for the radiosonde station Lindenberg was used to validate the retrieval method. The agreement is reasonable if known systematic differences between AMSU and radiosonde are taken into account.

Additionally, it was investigated whether the method is suitable to study humidity supersaturation in the upper troposphere. In principle it is, but the regression noise and radiometric noise could lead to apparent supersaturation even if there were no supersaturation. For a radiometer noise level of 1 K the drop-off slope of the apparent supersaturation is $0.17\,\%\mathrm{RH}^{-1}$, for a noise level of 2 K the slope is $0.12\,\%\mathrm{RH}^{-1}$.

A qualitative comparison of UTH climatologies from AMSU data and HIRS data showed a good agreement. A cautionary note on the as-

sumption of Gaussian nature of UTH while deriving the climatology is made. A climatology of UTH can be made in two ways: One is by transforming the averaged brightness temperatures to UTH and the other by averaging the UTH values, obtained by the transformation of each brightness temperature. It is shown by an example using ECMWF reanalysis data that the results of the two methods differ significantly, the difference goes up to 6 %RH. These differences show a dependence on the standard deviation of the brightness temperatures, that is, the differences increases with the standard deviation.

The investigation with the aid of a simple Monte Carlo approach suggested that these differences are due to the log-normal nature of the UTH distribution which is caused by a frequent occurrence of very cold brightness temperatures. Interestingly, the Monte Carlo approach overestimated the differences observed with the ECMWF data. A further investigation with real AMSU-B data showed that this overestimation was due to the assumption of Gaussian distribution for the brightness temperatures in the Monte Carlo method. The differences obtained from the real AMSU data and simulated AMSU data were found to be consistent.

It was demonstrated that the use of a robust estimator, the median, could resolve the difference between the two climatologies. Therefore the use of robust estimators such as the median could prevent introducing spurious errors in climatologies. Note that several studies use the simple arithmetic mean in UTH climatological studies (Soden and Bretherton, 1993, 1996; Bates and Jackson, 2001; Bates et al., 2001), except the study by Lanzante and Gahrs (2000). The study confirms the usefulness of robust statistics in climate applications as suggested by Lanzante (1996). Thus, the use of median or other robust estimators is recommended over the use of the simple arithmetic mean. Although the discussion was only for UTH, the results may be also applicable to other climatological studies.

The main conclusion from this study is that the BT transformation method is very well suited for microwave data. Its particular strength is in climatological applications where the simplicity and the independence of a priori information are key advantages. Further studies applying the method to global and regional data are planned.

5 Comparison of Humidity Measurements by Satellite Microwave Sensors and Radiosondes

Radiosonde measurements are important for a large variety of meteorological and climate applications. For example, Peixoto and Oort (1996) have used them for making global climatologies of water vapor and Seidel et al. (2004) and Christy and Norris (2004) have used them for temperature trend analysis. Another important use of radiosonde data is to be assimilated into numerical weather prediction models (Lorenc et al., 1996). The radiosonde data have also been used for detecting super saturation (Spichtinger et al., 2003), identifying and removing biases from data sets (Lanzante and Gahrs, 2000), and deriving regression parameters (Spencer and Braswell, 1997). Another most important application of the data is their use as initial guess for profile retrievals from satellite data (Chaboureau et al., 1998) and validating satellite retrieval algorithms (Fetzer et al., 2003).

In spite of the fact that there are several studies which question the quality of humidity data from radiosondes (Elliot and Gaffen, 1991; SPARC, 2000), it is inevitable to use radiosonde data to validate satellite retrievals due to unavailability of other better data sets. Recently, there have been several studies which describe the validation of satellite derived upper tropospheric water vapor using radiosonde data, for example, Sohn et al. (2001); Buehler and John (2005); Jimenez et al. (2005); Houshangpour et al. (2005). But care has been taken in all these studies to use quality controlled radiosonde data. This signifies the importance to monitor and correct radiosonde data. Therefore we

were motivated to develop a satellite based tool for monitoring global radiosonde stations.

The synoptic radiosonde data goes back to the nineteen-forties (Elliot and Gaffen, 1991). Records are kept at national meteorological agencies. The data can also be obtained, for example, from the British Atmospheric Data Centre (BADC). The global radiosonde network consists of about 900 radiosonde stations, about two-thirds make observations twice daily and only about 250 stations have at least 10 launches per month reaching 100 hPa. Ideally, each station should launch a radiosonde four times a day at the synoptic observation times 0, 6, 12, and 18 UTC. However, many stations launch sondes irregularly. The quality of the data from the different stations is also believed to vary considerably.

These stations use different types of humidity sensors, which can be mainly classified into three categories: capacitive hygristor, carbon hygristor, and Goldbeater's skin hygrometer. The stations which are selected for the study, which is presented in this chapter launch only Vaisala radiosondes which use capacitive hygristor, except the Russian station Kem which launches Goldbeater's skin type sondes. Vaisala radiosondes use thin film capacitors which contain a polymer film dielectric whose dielectric constant changes with ambient water vapor pressure. There are mainly four versions of Vaisala radiosondes, RS80A, RS80H, RS90, and RS92. The RS80A has a time constant of 100 s at −50 °C and 400 s at −70 °C, thus it will respond to 63% of a step change in humidity over a vertical distance of 0.5 and 2 km, respectively (SPARC, 2000). The RS80H sensor has a smaller size and responds more quickly than RS80A. The RS90 type radiosondes have an improved humidity sensor, which is designed to solve the problem of sensor icing in clouds. The RS92 type radiosondes have an improved reconditioning procedure which removes all contaminants from the humidity sensor surface.

Even though the specified absolute accuracy of the Vaisala humidity sensors is 2 %RH, there exists a significant dry bias in the humidity measurements (Soden and Lanzante, 1996; Soden et al., 2004; Buehler et al., 2004; Turner et al., 2003; Nakamura et al., 2004). The error sources of this dry bias and a number of correction methods are

documented in the literature (Turner et al., 2003; Wang et al., 2002; Leiterer et al., 1997; Roy et al., 2004; Soden et al., 2004). Soden et al. (2004) examined the effect of some of these corrections and found that there still remains a significant dry bias after the corrections. Buehler et al. (2004) also arrived at a similar conclusion about the corrected humidity data.

Another important point is that these corrections are applied mostly to the data from special campaigns and not to the data from the global radiosonde network. There exists severe discontinuities in these data due to instrument and launch procedure changes. The monitoring tool developed in this study allows a continuous observation of the performance of the stations. All stations taken together can also be used to investigate systematic differences between microwave sensors on different satellites.

The basic idea of the study is to compare satellite and radiosonde measured humidity data. However, the satellite measures radiances, not humidity directly. While obtaining radiances from given temperature and humidity profiles is straightforward, obtaining humidity concentrations from radiances is complicated and requires additional assumptions (a classical inverse problem (Rodgers, 2000)). To avoid dealing with the inverse problem, the comparison is done in radiance space rather than state space: A radiative transfer (RT) model is used to generate simulated satellite measurements from the radiosonde data, which can then be compared to the real satellite measurements. This approach has already been used for infrared data, for example by Soden and Lanzante (1996), but has so far not been used for microwave data.

The aims of the study are, firstly, to develop a robust methodology for such a comparison, secondly, to check the mutual consistency of (a) satellite data, (b) radiosonde data, and (c) RT model, and thirdly, to check the mutual consistency and stability of instruments on different satellites. Another aim is to pave the way for a systematic comparison of all stations in the global radiosonde network to satellite data. This will allow an intercomparison and quality control of the different radiosonde stations, assuming that the satellite instrument's properties are stable during a few orbits.

The structure of this chapter is as follows: Section 5.1 presents the development of the comparison methodology and the case study using the Lindenberg radiosonde data, Section 5.2 describes a comparison of the performance of two radiosonde sensors, the Vaisala and Goldbeater's skin sensors, and Section 5.3 outlines a pilot study in which the performance of European radiosonde stations were investigated.

5.1 Development of the Methodology and A Case Study

Microwave humidity data exists from SSM/T2 (Special Sensor Microwave Water Vapor Sounder) on the DMSP satellites, from AMSU-B (Advanced Microwave Sounding Unit) on the NOAA satellites, and from HSB (Humidity Sounder for Brazil) on the Aqua satellite. Information on the available data is summarized in Table 5.1. This study focuses on NOAA-15 and NOAA-16 satellites for the years 2001–2002.

Table 5.1: A summary of currently operating microwave satellite humidity sensors.

Platform Name	Instrument Name	Launch
DMSP F-13	SSM/T2	March 1995
DMSP F-14	SSM/T2	April 1997
NOAA-15	AMSU-B	May 1998
NOAA-16	AMSU-B	September 2000
NOAA-17	AMSU-B	June 2002
Aqua	HSB	May 2002
Aura	EOS-MLS	July 2004

For the development of the methodology and the case study it was decided to focus on the radiosonde data from one station, the reference station Lindenberg of the German Weather Service (DWD). This has the advantages that the properties and quality of the data are well understood, and that high vertical resolution data, which is not in the BADC archive, can be used. The results of this section are already published in Buehler et al. (2004).

The structure of this section is as follows: Section 5.1.1 presents the Lindenberg radiosonde data, focusing on those data properties that are relevant for the comparison. Section 5.1.2 presents the RT model setup, the method of finding matches between the two data sets, and the error model. Section 5.1.3 discusses the results for different instrument channels, different radiosonde qualities, and different satellite instruments, and Section 5.1.4 includes summary and conclusions.

5.1.1 Lindenberg Radiosonde Data

The Meteorological Observatory, Lindenberg (MOL), Germany, located at 52° 22′ N, 14° 12′ E, is one of the reference stations of the DWD. The radiosonde record there goes back to 1905. Recently, strong efforts have been made to improve the calibration of Humicap humidity sensors (Leiterer et al. (1997)), together with the manufacturer Vaisala. Three versions of the same radiosonde data were used in this study, high resolution uncorrected (HRNC), high resolution corrected (HRC), and low resolution corrected (LRC). As mentioned above, another version of the data can also be obtained from the BADC global radiosonde archive.

Version HRNC is data treated by the standard Vaisala processing method and should therefore correspond to high resolution data from other stations using Vaisala RS80 humidity sensors. Version HRC is data corrected to high quality research sondes, which are launched at Lindenberg once a week. The corrections applied are described in detail by Leiterer et al. (1997). There are three corrections: dry bias correction, detection and elimination of data affected by sensor icing, and time lag correction. Over the whole year 2002, the integrated water vapor content between 500 and 200 hPa is 3.33% higher for the corrected data (0.721 $\mathrm{kg\,m^{-2}}$ compared to 0.697 $\mathrm{kg\,m^{-2}}$). The average UTH (average relative humidity between 500 and 200 hPa) is 3.3 %RH higher for the corrected data (35.2 %RH compared to 31.9 %RH). This is demonstrated in Figure 5.1. The figure shows ΔUTH values for HRNC, LRC, and BADC data sets taking HRC as the reference. Note that the BADC data version is not used in this section, but in Section 5.3.

Another interesting feature in the figure is that LRC and BADC data sets behave in a similar way, showing very little wet bias. This suggests that the data obtained from BADC for Lindenberg is the corrected data.

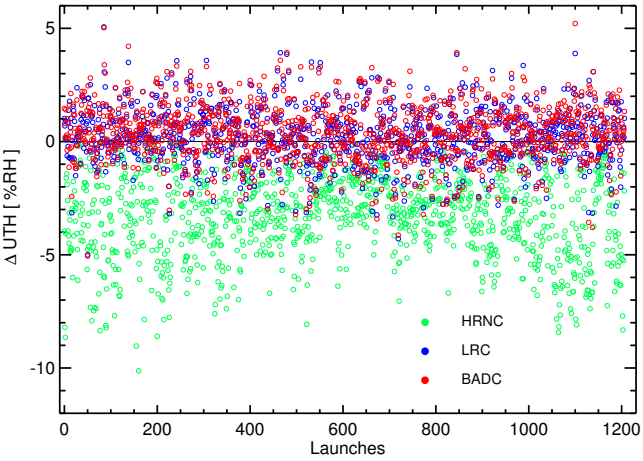

Figure 5.1: Comparison of different versions of radiosonde data from Lindenberg. Three versions of the data, HRNC, HRC, and LRC (see text for the details), are obtained from the station itself and the fourth version is from the radiosonde archive of BADC. The HRC data is taken as the reference. ΔUTH values are shown for HRNC (green), LRC (blue), and BADC (red) for the year 2002.

Version LRC of the data is the low resolution data that is broadcasted in the operational radiosonde network. From the approximately 300 altitude levels of the high resolution data between the surface and 100 hPa, only 30 'significant' levels remain. This procedure leads to a loss of detail, but only to a very small bias of 0.25 %RH. It has to be pointed out that this good agreement between LRC and HRC data can only be achieved if the LRC data is interpolated to a fine grid before calculating column quantities. The interpolation scheme is crucial, the best results are obtained when humidity is interpolated in relative humidity, whereas interpolation of humidity in volume mixing ratio (VMR) leads to a large discrepancy between the two data sets.

It is important to understand these biases since (uncorrected) low resolution data is all that is readily available for most of the radiosonde stations worldwide, which will be affected by a dry bias from the missing sensor correction.

5.1.2 Methodology

Radiative Transfer Setup

The RT model ARTS was used to simulate AMSU radiances based on radiosonde profiles. Five radiance values, one for each AMSU-B channel, were obtained for each radiosonde launch. Radiances were expressed as brightness temperatures in Kelvin, similar to the AMSU data. The program setup for this study was as described in Section 3.3.2.

For the radiative transfer calculation, temperature and relative humidity were interpolated linearly in log pressure onto 1000 pressure levels, evenly spaced in log pressure, between the surface and 100 hPa. The radiative transfer integration step along the line of sight was 5 m. The geometric altitude profile was taken from the radiosonde data.

Required geophysical inputs of the model in this case are humidity and temperature profiles, the surface emissivity, and the surface skin temperature. Humidity and temperature profiles were taken from the radiosonde, the surface emissivity was assumed fix at 0.95, and the skin temperature was assumed to be equal to the lowest radiosonde temperature. The surface emissivity influences mainly the window Channels 16 and 17, under extremely dry conditions also Channel 20. Channels 18 and 19 are not influenced by the surface, which was found by repeating the analysis, as described below, for different surface emissivity values. That exercise also confirmed the choice of 0.95 for the surface emissivity as reasonable for the Lindenberg area.

Radiosondes do not always reach the same altitude. In order to eliminate the influence of the different maximum altitudes, all profiles were cut at 100 hPa, an altitude reached by all but 406 sondes in the 2001–2002 time period. Of course, this cutting introduces both a bias (from the missing dry atmosphere above 100 hPa) and a random error (from temperature and humidity fluctuations above 100 hPa).

Simulations for the ECMWF data set (Chevallier, 2001) were used to assess this. These profiles go up to 10 Pa. The difference between simulations with the full profile and the profile cut at 100 hPa are summarized in Table 5.2. The cutting procedure mainly introduces a bias of approximately −0.033 to 0.090 K, depending on channel, but only a small random error of 0.006 to 0.057 K.

Table 5.2: Difference in mK between simulated brightness temperatures for profiles cut at 100 hPa and full profiles up to 10 hPa (mean and standard deviation). GN: Global profiles, nadir view, GON: Global profiles, most off-nadir view, MN: Midlatitude profiles, nadir view, MON: Midlatitude profiles, most off-nadir view. Midlatitude means that only profiles between 50 and 70° N were used. In most cases, the cut profiles result in slightly warmer brightness temperatures.

Channel	GN	GON	MN	MON
16	1 ± 42	32 ± 74	-30 ± 34	-33 ± 57
17	12 ± 19	32 ± 29	-7 ± 15	0 ± 26
18	81 ± 31	130 ± 57	60 ± 25	90 ± 47
19	27 ± 9	46 ± 16	18 ± 6	31 ± 11
20	20 ± 9	38 ± 14	10 ± 8	23 ± 10

Selecting Matches

Given a radiosonde profile, one can simulate an AMSU measurement. But how to compare this to the real AMSU data? Matching the sonde to an individual AMSU pixel would be over ambitious, if only because the sonde drifts approximately 50 km horizontally during its ascent to 100 hPa. Hence, the approach is to compare the sonde to the average AMSU radiance in a target area, described by a circle of radius 50 km as demonstrated in Figure 5.2), which shows an example of AMSU data from Channel 18. This is an evening overpass of NOAA-15 over the station Lindenberg on 15 May 2001. Normally, 10–30 pixels will be in this target area.

Since the AMSU data in the target area is taken under different satellite viewing angles, the limb effect has to be considered. This is discussed in detail in Section 3.3.1. In order not to introduce any

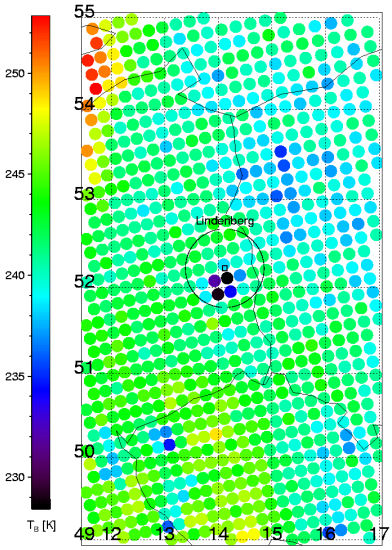

Figure 5.2: An AMSU overpass over station Lindenberg. The circle drawn around the station has a radius of 50 km.

error, simulations were done as many times as the number of pixels in the target area for each radiosonde profile, taking into account the viewing angle of each pixel.

The next problem is the satellite overpass time, which can be up to three hours before or after the radiosonde launch (see Figure 5.3). The displacement of the air mass measured by the sonde during this time is estimated as follows: First the average wind speed and direction between 700 and 300 hPa are calculated from the radiosonde wind data. The layer between these two pressure levels correspond to the altitude range which is most important for the humidity channels.

The average wind vector is then multiplied by the time difference between the satellite overpass and half an hour before the synoptic time. In the ideal case, the sonde should be launched approximately one hour before the synoptic time, so that the synoptic time is representative for the profile as a whole. Therefore, the time difference between overpass and half an hour before the synoptic time is the

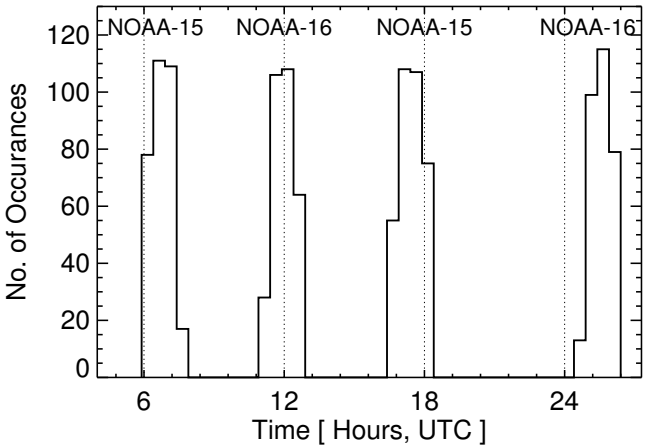

Figure 5.3: Histograms of NOAA satellite overpass times. These are the times when an AMSU-B pixel closer than 25 km to the station occurred. The dotted vertical lines represent synoptic hours.

appropriate one to use. If the displacement calculated in this way is larger than 50 km the data is discarded. This eliminates approximately 35% of the matches.

Error Model

Sources of error for the comparison are: (a) radiometric noise of the AMSU measurement, (b) sampling error due to atmospheric inhomogeneity, (c) radiosonde measurement error in humidity and temperature, (d) RT model error (systematic), and (e) AMSU calibration error.

The concept of the target area can be used to estimate the combined effect of (a) and (b), by calculating $\sigma_{50\mathrm{km}}(i)$, the standard deviation of the brightness temperature of all pixels within the target area. The index i here indicates that this can be calculated for every match. Figure 5.4 shows histograms of this quantity for the year 2002 for both satellites.

If the atmosphere is very homogeneous, $\sigma_{50\mathrm{km}}$ should be determined by the radiometric noise, as expressed by the noise equivalent temperature σ_{RN}, plus a small contribution from the limb effect. This is

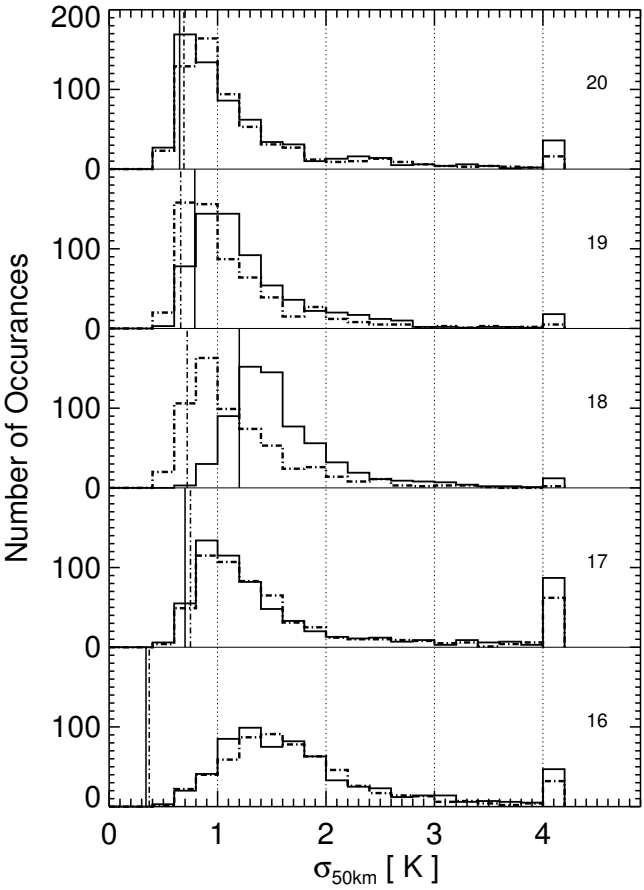

Figure 5.4: Histograms of target area average radiance standard deviation, $\sigma_{50\mathrm{km}}$, for all AMSU-B channels. The channel is indicated in the right part of each figure. The solid line represents NOAA-15 data for 2002, the dash dotted line NOAA-16 data for the same year. The rightmost bin contains all data for which $\sigma_{50\mathrm{km}} > 4\,\mathrm{K}$. The vertical solid and dash dotted lines indicate the mean noise equivalent temperature (σ_{RN}) from the instrument calibration process, also for the same year, which were derived from 10 day median values which are obtained from the Met Office, UK.

confirmed by the good agreement of the σ_{RN} estimated from the AMSU calibration (vertical lines in Figure 5.4) with the left edge of the histograms. Channel 16, and to a lesser degree 17, are exceptions, since for these channels the inhomogeneity of the surface plays a significant role. Figure 5.4 also confirms that the performance of Channel 18 has greatly improved for NOAA-16, compared to NOAA-15. Channel 19 has also slightly improved.

If $\sigma_{50\mathrm{km}}$ is significantly above the radiometric noise, it means that atmospheric inhomogeneities on the 15–50 km scale are present. The $\sigma_{50\mathrm{km}}$ can exceed 4 K, in most cases it will be the dominant error source. This suggests the error model:

$$\sigma(i) = \sqrt{C_0^2 + \sigma_{50\mathrm{km}}^2(i)} \tag{5.1}$$

A χ^2 test for a linear fit of AMSU radiances versus ARTS simulated radiances, in combination with a goodness of fit estimate (Press et al., 1992, Eq. 15.2.12) was used to try this error model for different values of the constant C_0. For this, the matches were divided in different $\sigma_{50\mathrm{km}}$ bins, and χ^2 and probability Q were calculated for each bin. Figure 5.5 shows the results for Channel 19 of NOAA-15 for the full year of 2001.

If $C_0 = 0$, only the cases with rather high $\sigma_{50\mathrm{km}}$ have a reasonably low χ^2, hence a reasonably high probability Q. This confirms that for low inhomogeneity the other error sources contribute significantly.

Plots similar to Figure 5.5 were made for Channels 18–20 for both satellites and years, resulting in a total of 12 plots. To keep the error model simple, a global constant value of $C_0 = 0.5$ K was selected as giving a reasonable probability for all cases. This constant is assumed to account for error sources (c), (d), and (e), and also for that part of the sampling error (b) that is due to inhomogeneities on a smaller scale than resolved by AMSU. This places 0.5 K upper bounds on the RT model error (d) and the AMSU calibration error (e). It also places an upper bound of approximately 5% on the radiosonde humidity error, which can be derived by sensitivity RT calculations. (Here a radiosonde calibration error is meant that is fixed for one launch, but random between different launches.)

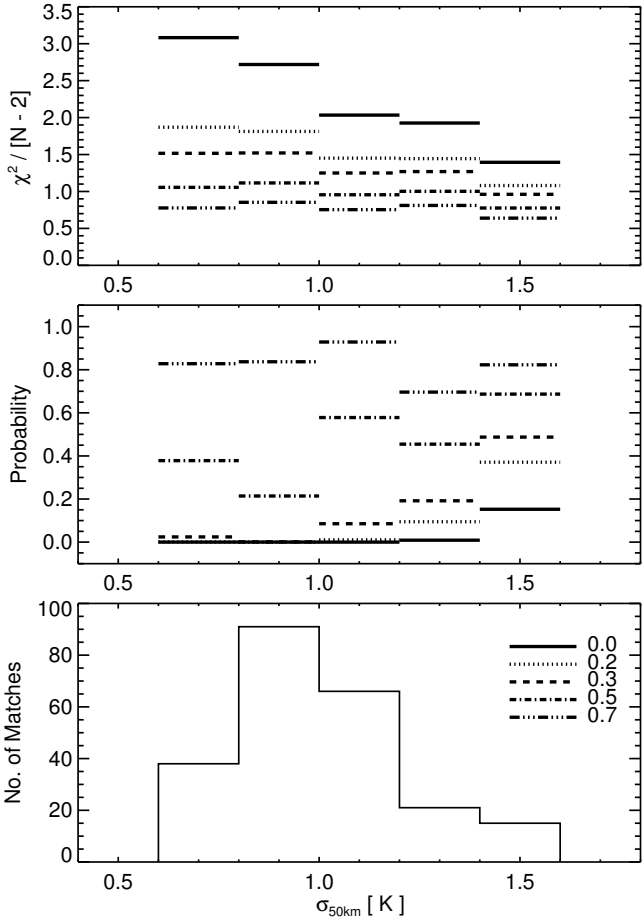

Figure 5.5: Result of χ^2 test for the credibility of the error model. The top plot shows the χ^2 values normalized to $N-2$ for each bin, where N is the number of matches for each bin. The middle plot shows the probability which gives a quantitative measure of the goodness of fit of the model. The bottom plot shows the number of matches in each bin. Line styles used for different C_0 values are shown in the bottom plot.

Cirrus Cloud Filtering

Another issue to be addressed is a possible contamination of the measurement by cirrus cloud scattering. From model calculations by Sreerekha et al. (2002) this is expected to be only significant for strong cirrus clouds. In that case one expects the measured radiances to be colder than the simulated ones, because the cloud scatters radiation out of the line of sight of the instrument. The most sensitive channel for this effect is Channel 20, because its Jacobian peaks below typical cirrus cloud altitudes.

The difference between measured and modeled radiances, D, is defined as:

$$D(i) = T_{\mathrm{B}}^{\mathrm{AMSU}}(i) - T_{\mathrm{B}}^{\mathrm{ARTS}}(i) \tag{5.2}$$

where i is again the index of the match. Figure 5.6 shows a scatter plot of D^{20}, the difference between measured and modeled brightness temperatures for Channel 20, as a function of $T_{\mathrm{B}}^{\text{AMSU-20}}$, the measured radiance in Channel 20. At $T_{\mathrm{B}}^{\text{AMSU-20}}$ below approximately 260 K the measured radiances start to get significantly colder than the modeled ones, which can be interpreted as the cloud signal. Because the present study uses only a clear-sky RT model, all matches with $T_{\mathrm{B}}^{\text{AMSU-20}} < 260\,\mathrm{K}$ are discarded, thus implementing a rough filter against strong ice clouds. Although only Channel 20 is used to define the filter, it is applied to all channels.

The results are not very sensitive to the exact value of the cloud filter threshold. For example, the bias between radiosonde and satellite data for Channel 18 (see next section for exact definition) will change by only 0.2 K when the cloud filter threshold is varied from 255 K to 265 K. Most of this change happens between 260 K and 265 K, because at these high threshold values a significant part of the data is removed by the filter. The slope between modeled and measured radiances (see also next section for definition) is even less affected by the threshold value: It changes only by 0.02 K/ K when the threshold value is varied from 255 K to 265 K.

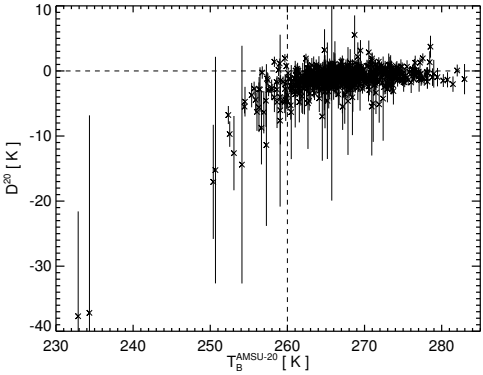

Figure 5.6: Measured minus modeled radiances for Channel 20 (D^{20}) as a function of measured Channel 20 radiance ($T_{\mathrm{B}}^{\text{AMSU-20}}$). Time period: 2001–2002; satellite: NOAA-15. The vertical line at $T_{\mathrm{B}}^{\text{AMSU-20}} = 260\,\mathrm{K}$ indicates the cloud filter threshold. Data with lower $T_{\mathrm{B}}^{\text{AMSU-20}}$ is discarded, not only for Channel 20, but also for the other channels.

Statistics

The mean value $\bar{D}$ of the differences $D(i)$ could be taken to represent the bias between the modeled and the measured radiances. However, it is more appropriate to define a measure of the bias that takes into account the error model as described in the previous section. Hence, we define the bias B as

$$B = \frac{\sum \sigma(i)^{-2} D(i)}{\sum \sigma(i)^{-2}} \tag{5.3}$$

As pointed out in Section 4.3.1, radiance differences scale in proportion to relative errors in relative humidity. In the case of Channel 18, a bias B of 1 K in brightness temperature corresponds to approximately 7% relative error in relative humidity, as shown by Figure 5.7. It is important to note that the sensitivity depends on the temperature profile rather than on the humidity level, therefore the figure shows curves for several different temperature profiles. The sensitivity is displayed for relative changes in relative humidity, using 50 %RH as the reference. The sensitivity is highest for the high lapse rate temperature

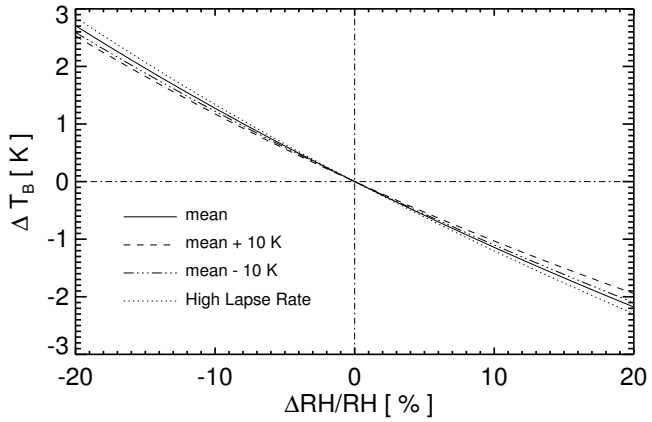

Figure 5.7: Sensitivity of simulated radiance for Channel 18 to relative changes in relative humidity. Four temperature profiles were constructed using the mean Lindenberg temperature profile of 2002: the mean profile itself (solid line), the mean profile plus 10 K at all levels (dashed line), the mean profile minus 10 K at all levels (dash-dotted line), and the mean profile with a higher lapse rate below the tropopause (dotted line). The high lapse rate case had the same tropopause temperature but a 20 K higher surface temperature. All four profiles have 50 %RH at all levels. Each profile was perturbed to a maximum of 20% on either side in 1% steps.

profile. The linear relationship shown in the figure is an independent proof of the validity of Equation (4.1).

The uncertainty in the bias can be estimated from its standard deviation

$$\sigma_B = \sqrt{\frac{1}{\sum \sigma(i)^{-2}}} \tag{5.4}$$

Figure 5.8 suggests that in some channels there may be not only a bias, but also a slope between modeled and measured radiances. Therefore, a straight line was fitted to the data as

$$T_{\mathrm{B}}^{\mathrm{fit}} = a \times T_{\mathrm{B}}^{\mathrm{ARTS}} + b \tag{5.5}$$

The coefficients a and b, as well as their uncertainties (standard deviations) can be easily obtained from a least squares fit, using the error

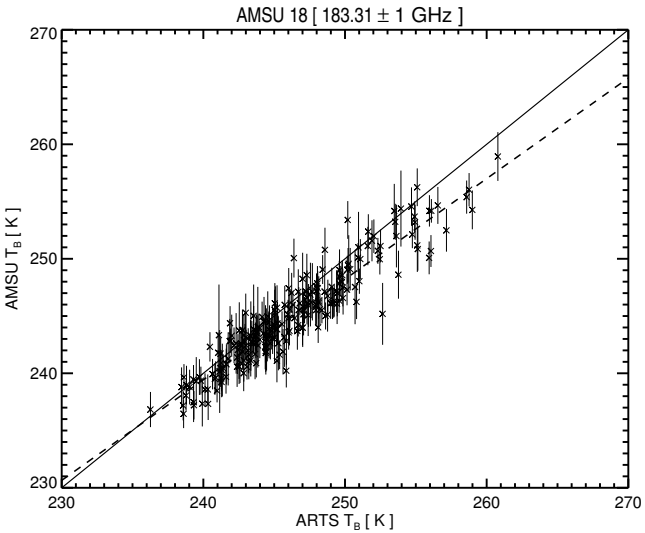

Figure 5.8: Average AMSU radiance for a 50 km radius target area versus ARTS modeled radiance based on radiosonde data for AMSU-B Channel 18. Time period: 2001; satellite: NOAA-16; data set: LRC. Vertical bars indicate the $\sigma(i)$ as defined in Equation (5.1). The dashed line is a linear fit.

model as described above. The result is displayed in Figure 5.8 as a dashed line. The most significant deviation of the slope from unity is found for Channel 18 (Figure 5.8). This finding is persistent for all satellites and time periods, as we shall see below.

As an example of the level of agreement that can be achieved, Figure 5.8 shows scatter plots of AMSU radiance versus ARTS modeled radiance for AMSU-B Channel 18 on NOAA-16 for the year 2001.

5.1.3 Results and Discussion

Comparison of Different Data Versions

Table 5.3 shows comparison results for the three different Lindenberg data versions HRC, HRNC, and LRC, as defined in Section 5.1.1. For simplicity, the comparison is limited to the 2002 time period for the

satellite NOAA-15. Shown are σ_D, bias B, as well as slope a and offset b of the straight line fit, as defined in Section 5.1.2.

Table 5.3: AMSU versus radiosonde simulated radiances for different versions of the radiosonde data. Time period: 2002; satellite: NOAA-15. The first column indicates the instrument channel, the second the radiosonde data version: high resolution corrected (HRC), high resolution not corrected (HRNC), low resolution corrected (LRC, see Section 5.1.1). The third column gives the standard deviation σ_D of the brightness temperature difference D as defined in Section 5.1.2. All other quantities as defined in Section 5.1.2.

Ch.	Data Version	σ_D [K]	B [K]	a [K/K]	b [K]
18	HRC	1.6	-0.43 ± 0.11	0.850 ± 0.024	36.6 ± 5.9
	HRNC	1.6	-1.11 ± 0.11	0.864 ± 0.024	32.4 ± 6.0
	LRC	1.7	-0.32 ± 0.11	0.853 ± 0.024	35.9 ± 5.9
19	HRC	1.9	0.41 ± 0.10	0.908 ± 0.021	24.2 ± 5.4
	HRNC	1.9	0.11 ± 0.10	0.921 ± 0.021	20.6 ± 5.5
	LRC	2.0	0.40 ± 0.10	0.903 ± 0.021	25.4 ± 5.4
20	HRC	1.3	-0.91 ± 0.08	0.983 ± 0.019	3.8 ± 5.2
	HRNC	1.3	-1.03 ± 0.08	0.986 ± 0.019	2.6 ± 5.2
	LRC	1.3	-0.91 ± 0.08	0.973 ± 0.019	6.4 ± 5.1

For the surface Channels 16 and 17 (not shown) there are no significant differences between the data versions, as expected. For the humidity Channels 18–20 there are differences, which increase with sounding altitude (from Channel 20 to 18). For Channel 18 the difference in B between HRC and HRNC data is 0.7 K, while the standard deviation of B is only 0.11 K. The HRC simulated radiances are colder than the HRNC ones, consistent with the fact that the HRC data are more humid than the HRNC data. The observed 0.7 K value of the difference is also roughly consistent with the average 3.3 %RH difference in UTH (9% relative difference) between these two data versions. From Figure 5.7 the expected value for the difference would have been about 1 K, the difference can be explained by the fact that the humidity bias between the two data versions was computed over all radiosonde launches, whereas the brightness temperature bias was computed only over the launches that matched the satellite overpass.

This result confirms that the satellite measurement is sensitive and

accurate enough to distinguish between corrected and uncorrected data. Furthermore, the fact that the largest difference is found for the channel with the highest sounding altitude is consistent with the fact that the radiosonde correction algorithm has its highest impact in the upper troposphere.

For the LRC data, on the other hand, the difference in B to the HRC data is much smaller and not significant compared to the standard deviation of B. This confirms that the vertical resolution of the LRC data is sufficient to accurately predict AMSU radiances, which can be explained by the approximately 3 km width of the AMSU Jacobians (see Figure 3.4). This is a very encouraging result, because it confirms that the wealth of low resolution radiosonde data in the operational archives can be used for future intercomparison studies.

Comparison of Different Satellites and Time Periods

Table 5.4 shows comparison results broken down by satellite (NOAA-15 and NOAA-16) and time period (2001 and 2002). The number of matches in the different cases was: 247 for NOAA-15 in 2001; 290 for NOAA-15 in 2002; 113 for NOAA-16 in 2001, and 154 for NOAA-16 in 2002. The first thing noticeable is that there is a small but significant difference between NOAA-15 and NOAA-16. To get an error estimate for this, the two year study time period was broken down further into sub-periods of three months, yielding eight values each for σ_D, B, a, and b. From these, mean values and standard deviations of the difference between the two satellites were calculated, which are also displayed in Table 5.4.

Thus, significant differences between the two satellites are found for Channels 18 and 19. These are the channels for which instrument performance has improved from NOAA-15 to NOAA-16, however, it is not clear how that translates into a systematic difference, since the variability σ_D of the difference D is dominated by atmospheric inhomogeneity, rather than instrument noise. So, it appears that the calibration has also slightly changed for these channels between the satellite versions.

Table 5.4: AMSU versus radiosonde simulated radiances for different satellites and time periods. The second column indicates the satellite and time period, the satellite is either NOAA-15 or NOAA-16, the time period either the whole year of 2001 or 2002. The radiosonde data version is LRC. All other quantities are as defined in Section 5.1.2.

Ch.	Data set	σ_D [K]	B [K]	a [K/K]	b [K]
Original radiosonde					
18	N15, 2001	1.4	0.10 ± 0.12	0.888 ± 0.025	27.7 ± 6.0
	N15, 2002	1.7	-0.32 ± 0.11	0.853 ± 0.024	35.9 ± 5.9
	N16, 2001	1.6	-0.73 ± 0.14	0.895 ± 0.027	25.3 ± 6.7
	N16, 2002	1.7	-1.15 ± 0.12	0.863 ± 0.027	32.8 ± 6.6
	N15−N16	0.0 ± 0.2	0.99 ± 0.55	-0.020 ± 0.060	5.8 ± 14.9
19	N15, 2001	1.7	0.10 ± 0.10	0.953 ± 0.021	12.3 ± 5.5
	N15, 2002	2.0	0.40 ± 0.10	0.903 ± 0.021	25.4 ± 5.4
	N16, 2001	1.3	-0.66 ± 0.13	0.923 ± 0.026	19.5 ± 6.8
	N16, 2002	1.5	-0.98 ± 0.12	0.926 ± 0.028	18.4 ± 7.3
	N15−N16	0.5 ± 0.2	1.06 ± 0.60	0.009 ± 0.100	-1.3 ± 26.2
20	N15, 2001	1.2	-0.97 ± 0.09	1.037 ± 0.020	-10.9 ± 5.5
	N15, 2002	1.3	-0.91 ± 0.08	0.973 ± 0.019	6.4 ± 5.1
	N16, 2001	1.2	-0.98 ± 0.13	0.959 ± 0.030	10.0 ± 8.0
	N16, 2002	1.4	-1.20 ± 0.12	0.945 ± 0.025	13.6 ± 6.8
	N15−N16	-0.1 ± 0.2	0.09 ± 0.37	0.009 ± 0.133	-2.5 ± 35.4

Possible Explanations for the Slope in Channel 18

The data in Tables 5.3 and 5.4 show that radiosonde humidity data and AMSU radiances are overall in very good agreement, with the notable exception of Channel 18, which has a slope a significantly deviating from unity. The value ranges from $0.853 \pm 0.024\,\mathrm{K/K}$ to $0.895 \pm 0.027\,\mathrm{K/K}$, depending on satellite and year. (Channel 19 also shows a slope, but the deviation from unity is barely significant.) There are three possible explanations for this discrepancy: (1) a systematic error in the RT model, (2) a systematic slope-like error in the AMSU radiances, and (3) a systematic error in the radiosonde data, increasing with lower humidity values.

Possibility 1 can be easily studied by re-processing the data with

Table 5.5: Same as Table 5.4 but radiosonde data increased by 2 %RH at 0 %RH (top block) and radiosonde data increased by 4 %RH at 0 %RH (bottom block).

Ch.	Data set	σ_D [K]	B [K]	a [K/K]	b [K]
Radiosonde +2 %RH at 0 %RH					
18	N15, 2001	1.4	0.57 ± 0.12	0.938 ± 0.026	15.9 ± 6.4
	N15, 2002	1.6	0.18 ± 0.11	0.904 ± 0.026	23.6 ± 6.3
	N16, 2001	1.5	-0.19 ± 0.14	0.957 ± 0.029	10.3 ± 7.1
	N16, 2002	1.6	-0.62 ± 0.12	0.919 ± 0.028	19.3 ± 7.0
19	N15, 2001	1.6	0.35 ± 0.10	0.986 ± 0.022	4.0 ± 5.6
	N15, 2002	1.9	0.68 ± 0.10	0.940 ± 0.022	16.3 ± 5.6
	N16, 2001	1.2	-0.35 ± 0.13	0.964 ± 0.028	9.0 ± 7.1
	N16, 2002	1.4	-0.68 ± 0.12	0.967 ± 0.029	8.0 ± 7.7
20	N15, 2001	1.2	-0.85 ± 0.09	1.055 ± 0.021	-15.7 ± 5.6
	N15, 2002	1.3	-0.79 ± 0.08	0.994 ± 0.020	0.8 ± 5.3
	N16, 2001	1.1	-0.82 ± 0.13	0.979 ± 0.030	4.8 ± 8.2
	N16, 2002	1.4	-1.05 ± 0.12	0.971 ± 0.026	6.7 ± 7.0
Radiosonde +4 %RH at 0 %RH					
18	N15, 2001	1.4	1.06 ± 0.12	0.995 ± 0.028	2.4 ± 6.8
	N15, 2002	1.5	0.69 ± 0.11	0.961 ± 0.027	10.2 ± 6.7
	N16, 2001	1.5	0.37 ± 0.14	1.024 ± 0.031	-5.6 ± 7.6
	N16, 2002	1.5	-0.07 ± 0.12	0.983 ± 0.030	4.2 ± 7.5
19	N15, 2001	1.4	1.06 ± 0.12	0.995 ± 0.028	2.4 ± 6.8
	N15, 2002	1.9	0.98 ± 0.10	0.979 ± 0.023	6.5 ± 5.9
	N16, 2001	1.2	-0.01 ± 0.13	1.008 ± 0.029	-2.2 ± 7.5
	N16, 2002	1.4	-0.36 ± 0.12	1.011 ± 0.031	-3.2 ± 8.0
20	N15, 2001	1.2	-0.71 ± 0.09	1.075 ± 0.021	-20.9 ± 5.7
	N15, 2002	1.3	-0.64 ± 0.08	1.017 ± 0.020	-5.3 ± 5.4
	N16, 2001	1.2	-0.65 ± 0.13	1.000 ± 0.031	-0.5 ± 8.3
	N16, 2002	1.4	-0.89 ± 0.12	0.999 ± 0.027	-0.6 ± 7.2

various perturbed RT model parameters. Likely candidate parameters are (a) the air broadening parameter of the water vapor line, (b) the line intensity, (c) the temperature exponent of the air broadening parameter, and (d) the water vapor continuum. Table 5.6 shows a summary of the results of these simulations. Although the perturbations were chosen quite large (20% for the intensity, 50% for the other parameters), none of the candidate parameters can bring the slope a close to unity. Higher perturbations can not be justified on the basis of current spectroscopic knowledge, and would also destroy the good agreement in the other channels. We can thus rule out possibility 1, the RT algorithm, as a source of the discrepancy, leaving only possibilities 2 and 3.

Table 5.6: NOAA-15, 2001, LRC data, H_2O model default parameters. LW-50% – air broadening parameter scaled by −50%, LI+20% – line intensity scaled by +20%, Tx-50% – temperature exponent of air broadening parameter scaled by −50%, WC+50% – water vapor continuum scaled by +50%.

Ch.	Data Version	σ_D [K]	B [K]	a [K/K]	b [K]
18	LRC	1.4	0.10 ± 0.12	0.888 ± 0.025	27.7 ± 6.0
	LW-50 %	1.6	-0.76 ± 0.12	0.902 ± 0.025	23.4 ± 6.3
	LI+20 %	1.4	1.94 ± 0.12	0.903 ± 0.025	25.6 ± 6.1
	Tx-50 %	1.4	0.16 ± 0.12	0.890 ± 0.025	27.1 ± 6.1
	WC+50 %	1.4	0.15 ± 0.12	0.888 ± 0.025	27.5 ± 6.1
19	LRC	1.7	0.10 ± 0.10	0.953 ± 0.021	12.3 ± 5.5
	LW-50 %	1.9	-3.85 ± 0.10	0.979 ± 0.022	1.8 ± 5.8
	LI+20 %	1.7	1.62 ± 0.10	0.940 ± 0.021	17.0 ± 5.3
	Tx-50 %	1.7	-0.22 ± 0.10	0.958 ± 0.021	10.7 ± 5.5
	WC+50 %	1.7	0.27 ± 0.10	0.951 ± 0.021	12.9 ± 5.4
20	LRC	1.2	-0.97 ± 0.09	1.037 ± 0.020	-10.9 ± 5.5
	LW-50 %	2.0	-3.90 ± 0.09	0.860 ± 0.018	34.1 ± 4.8
	LI+20 %	1.2	0.09 ± 0.09	1.054 ± 0.021	-14.3 ± 5.5
	Tx-50 %	1.2	-1.21 ± 0.09	1.036 ± 0.020	-11.0 ± 5.5
	WC+50 %	1.2	-0.42 ± 0.09	1.051 ± 0.021	-14.1 ± 5.5

Possibility 2, a slope-like error in the AMSU 18 radiances, is possible, but not very likely, given that the slope is remarkably stable between the two different satellites studied, and given also that from the point

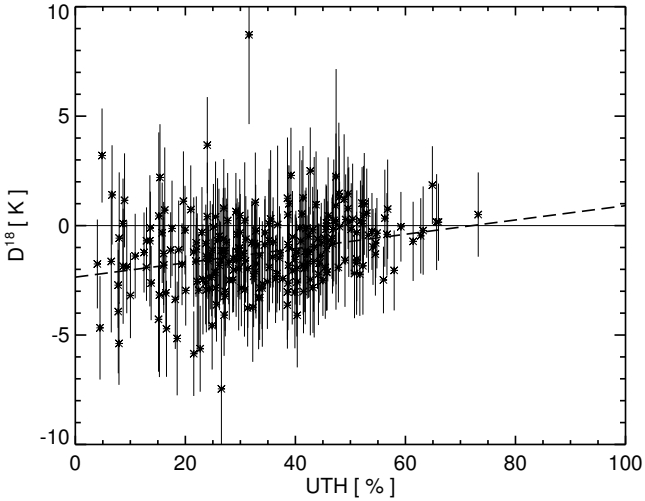

Figure 5.9: Measured minus modeled radiances for Channel 18 (D^{18}) as a function of UTH for the year 2002 and for NOAA-16. The dashed line represents a linear fit between UTH and D^{18}, taking into account the error model described in section 3.3. The fitted line in this case has a slope of 0.033 K/%RH and an offset of −2.4 K. The slope and offset for other years and satellites vary between 0.014 and 0.038 K/%RH and between −0.6 and −2.4 K respectively.

of view of the radiometer this channel is not significantly different from any other channel. What really distinguishes Channel 18 from the other humidity channels is its high atmospheric sounding altitude around 6–10 km, an altitude where radiosondes are most challenged. Thus, the results indicate that even the corrected Lindenberg data may still underestimate the humidity for very dry conditions.

To quantify this underestimation, D^{18} was plotted as a function of UTH (average RH between 500 hPa and 200 hPa), and a straight line was fitted (Figure 5.9). This yields at 0 %RH a brightness temperature difference of −0.6 K to −2.4 K, depending on satellite and year. To compensate this, the true UTH would have to be approximately 2 to 4 %RH where the radiosonde shows 0 %RH, according to Figure 5.7.

To verify this assertion, a simple linear correction was applied to the radiosonde humidity data. The correction was +2 %RH at 0 %RH,

decreasing linearly to 0 %RH at 70 %RH. Then the intercomparison was repeated with the modified radiosonde data. This indeed brings the slope in Channel 18 (and 19) closer to unity, while conserving the good agreement in Channel 20, as shown in the first part of Table 5.5. Repeating the exercise with a larger correction of +4 %RH at 0 %RH (second part of Table 5.5) leads to a slight over-correction with slopes more often above 1 than below. The necessary correction to the radiosonde data therefore seems to be between +2 and +4 %RH at 0 %RH.

Impact of Ozone and Stratosphere

In satellite-radiosonde humidity inter-comparison or validation exercises, as discussed above, for example, the entire stratosphere is normally ignored due to the poor quality of radiosonde humidity data (Soden and Lanzante, 1996; Buehler et al., 2004). The impact of this (cutting profiles at 100 hPa) was found to be less critical as discussed in Section 5.1.2 (see Table 5.2). But in those calculations, the effect of ozone lines (see Section 3.4) was not considered. Table 5.7 gives the statistics of ΔT_B due to the exclusion of the atmosphere above 100 hPa, including the ozone effect. The effect of the entire stratosphere increases the brightness temperature difference for all channels, significantly for Channel 18. The mean ΔT_B for Channel 18 is about -0.30 ± 0.06 K. A similar linear relation between Channel 18 brightness temperature and ΔT_B as seen in Figure 3.8 is obtained here also. The slope and offset of the linear fit are -0.01 K/ K and 2.3 K, respectively, and the correlation is -0.89. The sign of this slope is consistent with that discussed in Section 5.1.3.

Table 5.7: Statistics of ΔT_B in mK for AMSU-B channels calculated using ECMWF profiles.

Ch.	16	17	18	19	20
ΔT_B	-20.2 ± 37.0	-60.5 ± 22.5	-297.0 ± 77.1	-38.7 ± 6.9	-52.9 ± 5.9

Here, it is examined whether the slope can be partly explained by the exclusion of ozone and stratosphere in the comparison. In addi-

tion to the radiosonde data, ozonesonde data were also used for this purpose. While radiosondes are launched 4 times a day, ozonesondes are launched only once per week. Humidity values are reported only up to 100 hPa, but temperature and ozone values are reported up to the maximum height reached by the sondes, which is normally about 30 km (≈10 hPa). However, temperature and ozone values are taken from sonde data only up to 20 hPa, due to quality reasons. Above 100 hPa, a constant value 5 ppm for water vapor volume mixing ratio was used, which is considered as a representative stratospheric value.

Monthly mean climatology data of ozone (TOMS V8 climatology, G. Labow, personal communication, 2004) were used to fill up the altitudes where ozonesondes normally do not reach. The climatology is for each 10° latitude bin and based on recent ozonesonde and satellite data. The data set also contains a temperature climatology and the profiles reach up to 60 km (≈0.2 hPa).

The brightness temperatures of AMSU-B channels are calculated for corresponding instrument viewing angles in two different ways: (a) as discussed in Section 5.1.2, ozone is not included and the profiles are cut at 100 hPa and (b) profiles reaching up to 60 km and including ozone.

The result of this exercise is shown in Figure 5.10. There are only 61 matches left for the 2001–2002 time period due the small number of ozone profiles. As ozonesondes are launched at around 12:00 UTC, only NOAA-16 measurements are used in this comparison. A slope of $-0.011\,\mathrm{K}/\mathrm{K}$ for a linear fit was observed similar to that shown in Figure 3.8. Therefore the impact is not just an offset to the brightness temperature, but it varies from profile to profile. The ΔT_B is smaller for colder brightness temperatures or humid atmospheres and larger for warmer brightness temperatures or drier atmospheres.

The change in the slope is negligible, $0.852\,\mathrm{K}/\mathrm{K}$ when ozone and the entire stratosphere are excluded and $0.863\,\mathrm{K}/\mathrm{K}$ when ozone and stratosphere are included. Therefore only a very small part of the deviation of the slope from unity in the comparison can be explained due to the exclusion of ozone and stratosphere. The calculations were also done using only climatological profiles for ozone and the results are similar to the results obtained using ozonesonde profiles. This

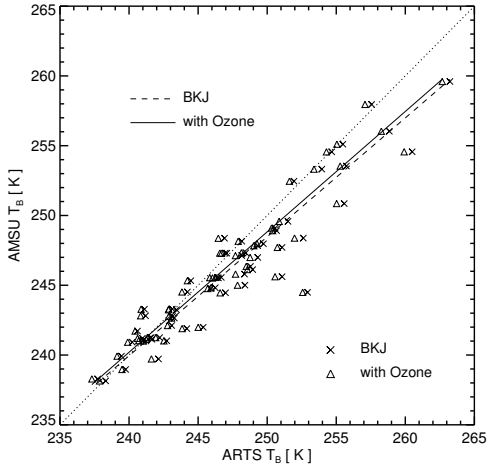

Figure 5.10: Measured versus simulated brightness temperature for AMSU-B Channel 18. The brightness temperatures are simulated in two ways: one as described in Section 5.1.2 (×) and the other one including ozone and the stratosphere in the RT calculations (△). Linear fits are also shown for both cases.

suggests that zonal, monthly mean climatological ozone profiles are sufficient to simulate AMSU-B radiances.

5.1.4 Summary and Conclusions

A robust method to compare radiosonde humidity data to AMSU data was developed, which is planned to be used for future global studies. The new method has some unique features: Firstly, the comparison is done for a target area, allowing an estimation of the atmospheric variability. Secondly, displacement and cloud filters are applied. Thirdly, a complete and consistent error model is used.

The method was validated by a detailed case study, using the high quality Lindenberg radiosonde data and the NOAA-15 and NOAA-16 satellite data for the time period from 2001 to 2002. The study confirmed that low vertical resolution data, as found in operational archives, is sufficient to accurately predict AMSU radiances. However,

it also demonstrated that corrections applied in Lindenberg to the standard Vaisala data processing make a significant difference, particularly in the upper troposphere.

Overall, the AMSU data are in very good agreement with the radiosonde data, with the notable exception of a slope in Channel 18. By re-processing with perturbed RT model parameters, RT model error was ruled out as a possible explanation for the slope, leaving only AMSU data and radiosonde data. Of these two, the latter seem the more likely explanation, which would mean that the corrected Lindenberg radiosonde data has a small residual dry bias at low humidities, giving 0 %RH when the true humidity is still approximately 2–4 %RH.

Furthermore, the impact of the weak ozone lines could not explain the slope in Channel 18. It is also demonstrated that zonal, monthly mean climatological ozone profiles are sufficient to account for the effect of the ozone lines on AMSU-B radiances.

5.2 Comparison of Two Radiosonde Types

Having found that the method of comparing radiosonde and satellite humidity measurements was able to identify the difference between different versions of the Lindenberg radiosonde data, it was decided to apply this method for comparing two different radiosonde sensors with completely different behavior: the Vaisala sensor which suffers a known dry bias and the Goldbeater's skin sensor which suffers a known very large wet bias (Soden and Lanzante, 1996). For the Vaisala radiosonde sensor, no additional calculations have been done since the results of the case study are sufficient for this purpose. Most of the results presented in this section are discussed in John et al. (2003).

Radiosonde data for the Russian station, Kem, located at 64° 95′ N, 34° 65′ E, are obtained from the BADC global radiosonde data archive to represent Goldbeater's skin sensor. One of the main problem with the radiosonde stations which use this sensor is that the availability of the data is limited in the archive either due to missing launches or due to the fact that the sondes do not reach up to 100 hPa. The station Kem was found to have sufficient data for a reasonable comparison.

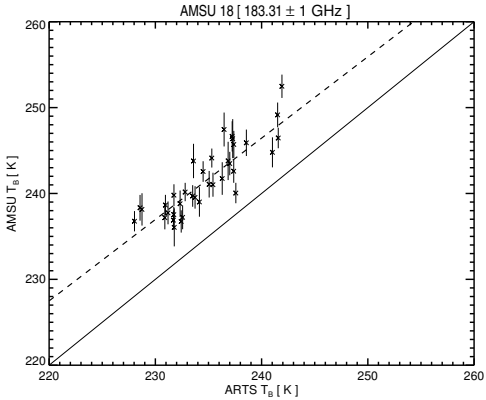

Figure 5.11: Average AMSU radiance for a 50 km radius target area versus ARTS modeled radiance based on radiosonde data for AMSU-B Channel 18 for the station, Kem, Russia, Kem. Time period: 2001; satellite: NOAA-16; data set: BADC. Vertical bars indicate the $\sigma(i)$ as defined in Equation (5.1). The dashed line is a linear fit.

The comparison methodology is the same as discussed in the previous section and the result of the comparison is shown in Figure 5.11 for AMSU-B Channel 18. In all matches, modeled brightness temperatures are less than the measured brightness temperatures. This is because there is a wet bias in the radiosonde data which results in the channels peaking higher in the atmosphere than it should peak. Therefore the modeled brightness temperatures represent a colder atmosphere due to the positive lapse rate in the troposphere.

The bias in this case is 6.7 K which is very large and opposite compared to the HRNC data. This is equivalent to a 40% (relative) wet bias in the upper tropospheric humidity measured by this type of radiosondes. It should be noted that Soden and Lanzante (1996) also reported such a large wet bias for Goldbeater's skin radiosondes. This proves that the method developed to compare AMSU-B and radiosonde humidity measurements can be used to monitor the performance of different radiosonde stations. The results of such a study is presented in the next section.

5.3 A Survey of European Radiosonde Stations

As a pilot study we selected stations from the countries which participate in COST Action 723 (COST is an intergovernmental framework for European Co-operation in the field of Scientific and Technical Research, the details can be seen at http://www.cost723.org). There are 17 countries participating in COST Action 723. Their names, in alphabetical order, are Belgium, Bulgaria, Cyprus, Czech Republic, Denmark, Finland, France, Germany, Greece, Italy, Netherlands, Norway, Poland, Spain, Sweden, Switzerland, and the United Kingdom. Most of the results discussed in this section are described in John and Buehler (2005).

The structure of this section is as follows: Section 5.3.1 presents the radiosonde data, focusing on the properties of the data which are relevant for this study. Section 5.3.2 discusses the results for different stations for different time periods and satellites, and Section 5.3.3 presents the conclusions.

5.3.1 Radiosonde Data

This section describes the radiosonde data, and some basic information on the radiosonde stations such as geographic location and the radiosonde type.

Radiosonde data used in this study are obtained from the British Atmospheric Data Centre (BADC). The radiosonde data archive at BADC consists of global operational radiosonde data. The humidity values are stored in the form of dew point temperatures. For the study, the dew point temperature was converted to actual water vapor pressure using the Sonntag formula (Sonntag, 1994).

Table 5.8 gives the short name, longitude, latitude, radiosonde type, location, and country of each station. The locations of the stations are shown in Figure 5.12. As AMSU-B channels are sensitive up to 100 hPa, the launches which reach at least up to this pressure level are used for the comparison. In order to have enough matches, only those stations which have at least 10 launches per month are included in this study.

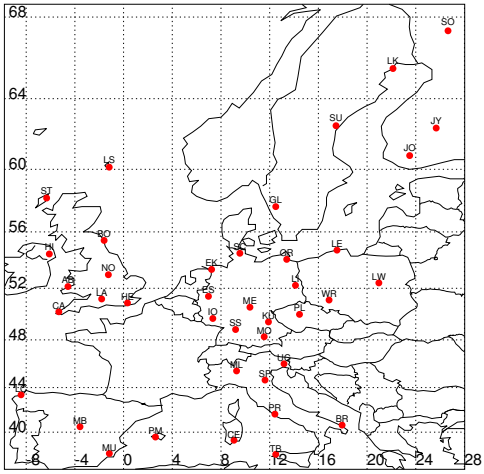

Figure 5.12: The geographical locations of the radiosonde stations used in this study. These stations launch at least 10 sondes per month which reach up to 100 hPa.

It should be noted that some of the countries do not have any station satisfying the above condition. All the selected stations launch Vaisala RS80 or RS90 radiosondes instruments. Out of 40 stations, 15 launch RS90 sondes and 6 use AUTOSONDE facility. The AUTOSONDE (AU) system improves the availability and quality of the data by launching the sondes at a preset time, receiving the radiosonde signals automatically, processing the signal into meteorological messages, and transmitting the messages to the external network.

The BADC archive contains low resolution radiosonde data, i.e., the vertical data levels are only standard and significant pressure levels. The significant levels are added to ensure that a linear interpolation of the profile approximates the real profile. It was found that the properly interpolated low resolution data are sufficient to represent layer averaged quantities such as upper tropospheric humidity (UTH) and to simulate AMSU-B radiance which is sensitive to UTH (Buehler et al., 2004).

5.3.2 Results and Discussion

The methodology here also is the same as discussed before, except that the bias B is calculated using a linear fit between the modeled and the measured brightness temperatures, taking into account the error model:

$$T_{\mathrm{B}}^{\mathrm{fit}} = a \times (T_{\mathrm{B}}^{\mathrm{ARTS}} - 245) + (B + 245). \tag{5.6}$$

The value 245 K was found to be the mean brightness temperature for Channel 18, when data from all stations were combined. Defining B like this reduces its dependence on different atmospheric states. The uncertainties of a and B are calculated as described in Press et al. (1992). In Section 5.1.2 it was found that the fitted line has a non-unity slope value a, mostly between 0.8 and 1.0, depending on the channel, which was attributed mainly to more underestimation of humidity by radiosondes in drier atmospheres than in wetter atmospheres.

This section describes the differences between different radiosonde stations for three years (2001–2003) and differences between satellites for the same time period.

We make use of two quantities to check the quality of data from different stations. They are the bias (B) and the slope (a) as defined in Section 5.1.2. These two quantities are calculated considering the error model, hence the matches with large sampling errors are less weighted. The study focuses on AMSU-B Channel 18 which is sensitive to the upper troposphere (approximately from 500 hPa to 200 hPa).

The relation to translate the quantities a and B which are expressed in radiance units (K) to UTH is:

$$\frac{\Delta \mathrm{UTH}}{\mathrm{UTH}} = \mathrm{const} \times \Delta T_{\mathrm{B}}, \tag{5.7}$$

which yields the relative error in relative humidity for a given absolute error in radiance (Buehler and John, 2005). The constant in the above equation is about -0.07, therefore a 1 K bias in radiance units is equivalent to a 7% relative error in upper tropospheric humidity. The negative value of the constant implies that a positive bias in the radiance is equivalent to a dry bias in the humidity and vice versa.

Table 5.8: Information of the selected radiosonde stations.

Stn.	Lon	Lat	RS Type	Location	Country
PL	14.45	50.02	RS90	Praha-Libus	Czech Rep.
JO	23.50	60.82	RS80	Jokioinen	Finland
JY	25.68	62.40	RS90	Jyvaskyla	Finland
SO	26.65	67.37	RS90	Sodankyla	Finland
EK	7.23	53.38	RS80	Emden-Koenig.	Germany
ES	6.97	51.40	RS80/AU	Essen	Germany
GR	13.40	54.10	RS80	Greifswald	Germany
IO	7.33	49.70	RS80	Idar-Oberstein	Germany
KU	11.90	49.43	RS80	Kuemmersruck	Germany
LI	14.12	52.22	RS80	Lindenberg	Germany
ME	10.38	50.57	RS80	Meiningen	Germany
MO	11.55	48.25	RS80	Muenchen-Ober.	Germany
SC	9.55	54.53	RS80	Schleswig	Germany
SS	9.20	48.83	RS80/AU	Stuttgart-Schnar.	Germany
BR	17.95	40.65	RS90	Brindisi	Italy
CE	9.07	39.25	RS90	Cagliari-Elmas	Italy
ML	9.28	45.43	RS90	Milano-Linate	Italy
PR	12.43	41.65	RS80	Pratica-di-Mare	Italy
SP	11.62	44.65	RS80/AU	S. Pietro Capofiume	Italy
TB	12.50	37.92	RS90	Trapani-birgi	Italy
UC	13.18	46.03	RS90	Udine-Campoformido	Italy
LE	17.53	54.75	RS90	Leba	Poland
LW	20.97	52.40	RS90	Legionowo	Poland
WR	16.88	51.12	RS90	Wroclaw	Poland
LC	−8.42	43.37	RS90	La-Coruna	Spain
MB	−3.58	40.50	RS80/AU	Madrid-Barajas	Spain
MU	−1.17	38.00	RS80	Murcia	Spain
PM	2.62	39.55	RS80/AU	Palma-de-Mallorca	Spain
GL	12.50	57.67	RS90	Goteborg-Landvetter	Sweden
LK	22.13	65.55	RS90	Lulea-Kallax	Sweden
SU	17.45	62.53	RS90	Sundvall-Harnlsand	Sweden
AB	−4.57	52.13	RS80	Aberporth	UK
BO	−1.60	55.42	RS80	Boulmer	UK
CA	−5.32	50.22	RS80	Camborne	UK
HE	0.32	50.90	RS80/AU	Herstmonceux-WE	UK
HI	−6.10	54.48	RS80	Hillsborough-MO	UK
LA	−1.80	51.20	RS80	Larkhill	UK
LS	−1.18	60.13	RS80	Lerwick	UK
NO	−1.25	53.00	RS80	Nottingham	UK
ST	−6.32	58.22	RS80	Stornoway-Airport	UK

Performance of Different Stations

Figure 5.13 shows results of the comparison for Channel 18 on NOAA-15. The NOAA-15 is a morning/evening satellite, therefore it collocates with 0600 and 1800 UTC radiosondes launched over Europe. Only about half of the selected radiosonde stations launch sondes at this time, mainly from Germany, Italy, and the UK.

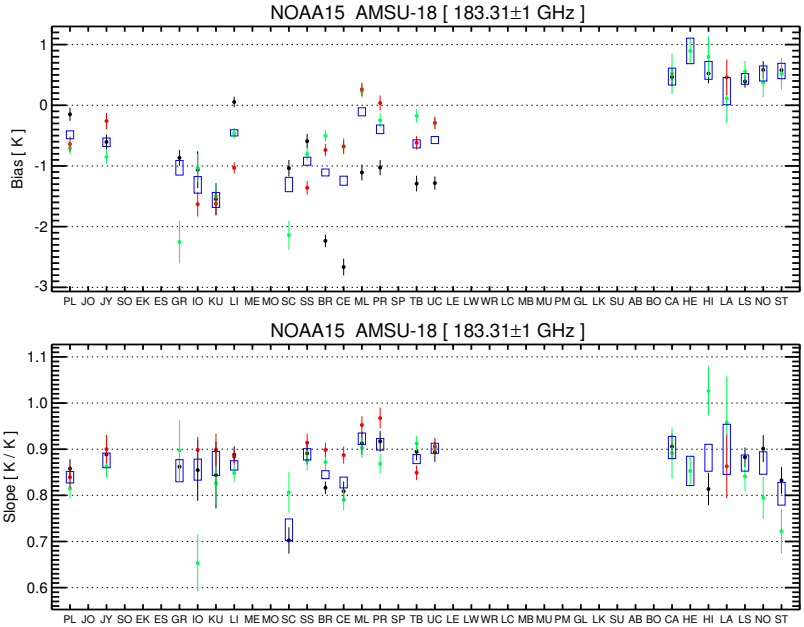

Figure 5.13: Bias (upper panel), slope (lower panel) and their uncertainties of all the stations for Channel 18. The satellite is NOAA-15. The values are shown for different years: 2001 (black), 2002 (green), and 2003 (red). Blue rectangles represent the quantity plus or minus the uncertainty for the whole time period (2001–2003).

One of the noticeable features is that the biases of the Italian stations (BR–UC) improve considerably for the years 2002 and 2003 compared to 2001. There is an improvement of about 2 K for BR and CE and about 1 K for the other stations. This may be due to an instrument change because a similar improvement in one of the UK stations

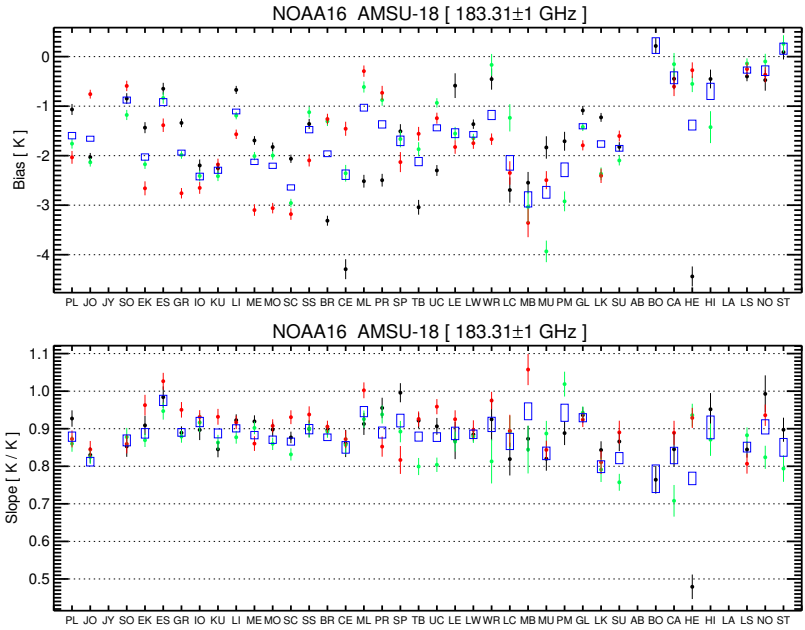

Figure 5.14: Same as Figure 5.13, but the satellite is NOAA-16.

was found as discussed later in this section. However, it is not advisable to use radiosonde data for 2001 from these stations for validating or tuning satellite algorithms.

All the available UK stations show a slight positive bias, an opposite behavior to the stations of other countries. A positive bias refers to a wet bias in the humidity measurements which is not common for Vaisala RS80/90 radiosondes. Moreover, the bias values are consistent through the years and the stations. But these stations show varying values of slope from 0.7 to 1.2, a low value in slope indicates that the underestimation of humidity by the sondes is more at drier conditions than at wetter conditions. Therefore a low value in slope together with a positive bias, as in case of ST in 2001, there is an overestimation of humidity at wetter conditions.

Two German stations GR and SC show a jump in bias between 2001 and 2002, the reason for which is not clear. The bias is -1 K for 2001 and -2 K for 2002. The station LI shows a systematic change in bias

through the years, it is almost 0 K in 2001, −0.5 K in 2002, and −1 K in 2003. Another feature of German stations is that the bias shows maximum value in 2003.

Most of the stations show a consistent slope through the years, though the values are different between the stations. Exceptions are IO, SC, HI, NO, and ST.

Figure 5.14 shows the bias and slope of Channel 18 on the NOAA-16 satellite. NOAA-16 is a mid-night/noon satellite which collocates with the 0000/1200 UTC radiosonde launch over Europe. Most of the selected stations launch sondes at this time.

The three very noticeable stations in this case are CE of Italy, MU of Spain, and HE of UK, which show a bias of about 4 K. In case of CE and HE this happens only in 2001, during the other years there is reasonable agreement with the other stations. HE shows a very different slope which is far away from unity. Other UK stations do not show any large biases.

Station PL shows a similar result as in the case of NOAA-15, that is, the 2001 bias is less than that of 2002 and 2003 biases, which is almost 0.6 K towards the colder side. But there is a shift in bias values between the satellites by about 1 K. This will be investigated in Section 5.3.2 to see whether this is due to the difference between the AMSU-B instruments on the two satellites.

The two Finnish stations, JO and SO, show consistent values for the bias in 2003. The values are consistent also over years for SO, but JO shows almost 1 K difference in bias values for 2001 and 2002. On an average, all the Finnish stations show very good performance in case of both the satellites.

Among the German stations, ES, LI, and SS have the least bias, about 1.0 K. ES and SS use AUTOSONDE systems while LI uses correction procedures as described in Leiterer et al. (1997). A general feature for all the German stations is that the bias is the smallest during 2001 and the largest during 2003. An exception to this is KU for which bias values for all the years is about −2.3 K.

The Italian stations show improvement in bias for 2002 and 2003 compared to 2001. The difference in bias is more than 1 K for most of

the stations. This feature was observed for NOAA-15 also. One exception is SP whose 2001 bias is less than that of 2002 or 2003.

The polish stations (LE–WR) show good agreement with AMSU data, biases are always less than −2 K. As in the case of the German stations, 2003 biases are the largest. For Spanish stations (LC–PM), for most cases 2001 has minimum bias and 2002 has maximum bias. The bias values are greater than about 2.0 K, which corresponds to 15% relative error in UTH, for all the stations. Therefore data from Spanish stations may not give good agreement in satellite validations. The Swedish stations (GL-SU) show comparatively better performance except for LK where 2002 and 2003 biases are about −2.5 K.

In the case of NOAA-16 also the UK stations show a near zero bias except for HE in 2001 and HI in 2002. In case of HE, the shift in bias is due to the instrument change. HE has switched from using Sippican Microsonde II to the Vaisala RS80 (and AUTOSONDE) in November 2001 (The details can be seen at: (http://www.metoffice.com/research/interproj/radiosonde/). It should be noted that the error bar of HI for 2002 is larger compared to the othert UK stations which indicates that the number of matches used for calculating the statistics is less. Therefore a higher bias in this case might be due to an insufficient sample size.

The slope in the case of NOAA-16 is around 0.9 K/ K for most of the stations, but there is a scatter for some of the stations. For example, the slope of some of the UK stations varies from 0.7 to 0.9 K/ K. The case of HE was discussed before and is an exceptional case.

The reason for all these jumps and differences are unclear, nevertheless the features appear to be real. For example, there is no conceivable reason why the satellite instrument should be biased differently over the UK, or why the bias should jump for all stations in Italy. The lack of proper documentation of the instrument change or correction methods at each station makes it difficult to attribute reasons to the observed variability in the performance of the stations.

Figure 5.15 shows a scatter plot of the anomalies of the biases versus anomalies of Channel 18 brightness temperature (T_{B}^{18}) for all the stations and the years for NOAA-16. The anomalies are calcu-

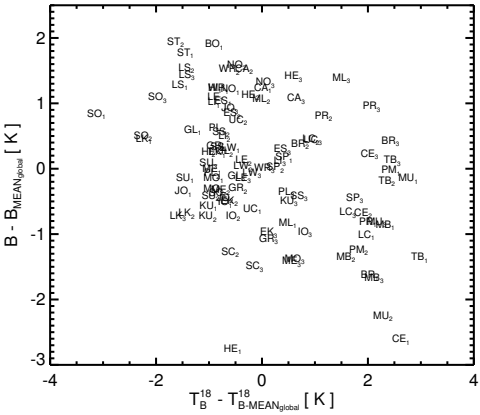

Figure 5.15: Anomaly of bias versus anomaly of Channel 18 brightness temperature for NOAA-16. The anomalies were calculated from the global mean, the mean brightness temperature of Channel 18 of all the stations for the whole time period. Station short names are used as plotting symbols. The subscripts 1–3 represents the years 2001–2003.

lated from the global mean values of the quantities, $T^{18}_{\text{B-MEAN}_{\text{global}}}$ and $\text{BIAS}_{\text{MEAN}_{\text{global}}}$, mean of all the stations for the whole time period. The values of these quantities are 245.55 K and −0.54 K for NOAA-15 and 245.30 K and −1.64 K for NOAA-16. One does not see any particular relation between the two anomalies. Similar results were found for NOAA-15 (not shown). This implies that the bias values are independent of the atmospheric conditions and are due to the differences in radiosonde measurements.

We went one step further to see whether the bias values are really independent of the atmospheric conditions at different stations by calculating the anomalies from the station means. Figure 5.16 shows the result of this and confirms that there is no explicit relationship between the two anomalies. This confirms that the bias values are independent of the atmospheric conditions.

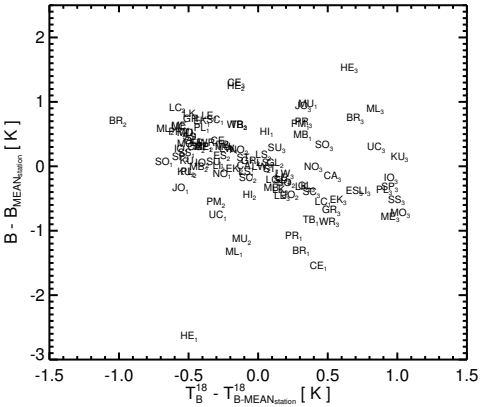

Figure 5.16: Anomaly of bias versus anomaly of Channel 18 brightness temperature for NOAA-16. The anomalies were calculated from the stations means, the mean brightness temperature of Channel 18 of each station station for the whole time period. Station short names are used as plotting symbols. The subscripts 1–3 represents the years 2001–2003.

Performance of Different Satellites

From Figures 5.13 and 5.14 one can notice a systematic difference in bias values between the two satellites, the magnitude of the bias is larger for NOAA-16 than for NOAA-15.

There can be two possible reasons for this. One is a systematic difference in the radiance measurements by the two satellites, the other is a systematic difference in the humidity measurements by radiosondes at different times of the day. To check the first possibility, we selected 10 stations to further study the difference between the satellites. They are PL, KU, LI, SS, BR, CE, ML, PR, TB, and UC. These stations are selected because they launch sondes 4 times a day, therefore have matches with both satellites. These stations have bias values for 2001, 2002, and 2003. The difference in bias, $\Delta B (= B_{\text{NOAA-15}} - B_{\text{NOAA-16}})$, between the satellites per year for each station was calculated. The mean of ΔB is 1.15 ± 0.12 K for 2001, 0.93 ± 0.14 K for 2002, and 0.77 ± 0.09 K for 2003. There is a decrease in ΔB through the years.

The mean of ΔB for the whole time period is 0.95 ± 0.12 K. The stability of ΔB has been verified by putting the 10 stations into two groups and calculating separate mean values, which were found to be consistent with the values given above.

To check the second possibility, we separated the matches by time. Now there are morning matches and evening matches for NOAA-15 and noon matches and mid-night matches for NOAA-16. The statistics of bias for all the stations are shown in Tables 5.9 and 5.10. The difference in bias between morning and evening matches ($B_{\text{moring}} - B_{\text{evening}}$) is from -0.61 to 0.11 K with a mean difference of -0.28 K. This indicates that morning launches have a drier bias than evening launches, but the differences are not very systematic among the stations as shown in Table 5.9. The difference in bias between noon and midnight matches ($B_{\text{noon}} - B_{\text{midnight}}$) is from -0.34 to -3.02 K with a mean difference of -1.41 K, that is, there is a systematic large dry bias in the noon launches. We repeated the analysis by further separating RS80 and RS90 instruments and the results were found similar as given in Table 5.10. It is known that there is a radiation error in radiosonde data which introduces a large dry bias in daytime soundings compared to nighttime sounding. Our analysis shows that the radiation error alone can contribute about 1.5 K or 11% relative error in UTH measurements according to Equation (5.7). Thus, the reason for the difference between biases for NOAA-15 and NOAA-16 is mostly coming from time dependent measurement errors in radiosonde data such as radiation error. Even if there are difference in the radiances measured by the instruments on NOAA-15 and NOAA-16, it may not be visible in this kind of comparisons due to the large errors in the radiosonde data.

Table 5.9: Detailed statistics for bias by separating morning / evening NOAA-15 satellite overpasses for the entire time period (2001–2003).

Stn.	Morning	No.	Evening	No.	Difference
PL	−0.71	152	−0.16	370	−0.55
JO	-	-	-	-	-
JY	−0.82	282	−0.34	170	−0.48
SO	-	-	-	-	-
EK	-	-	-	-	-
ES	-	-	-	-	-
GR	−0.70	24	−0.81	120	0.11
IO	−0.95	124	-	-	-
KU	−1.35	148	-	-	-
LI	−0.49	220	−0.19	620	−0.30
ME	-	-	-	-	-
MO	-	-	-	-	-
SC	−0.87	22	−0.76	124	−0.11
SS	-	-	−0.61	511	-
BR	−0.70	271	−0.32	424	−0.38
CE	−0.56	101	−0.50	327	−0.06
ML	0.11	146	0.02	396	0.09
PR	−0.39	148	0.05	338	−0.44
SP	-	-	-	-	-
TB	−0.45	148	0.07	390	−0.52
UC	−0.62	205	−0.27	492	−0.35
LE	-	-	-	-	-
LW	-	-	-	-	-
WR	-	-	-	-	-
LC	-	-	-	-	-
MB	-	-	-	-	-
MU	-	-	-	-	-
PM	-	-	-	-	-
GL	-	-	-	-	-
LK	-	-	-	-	-
SU	-	-	-	-	-
AB	-	-	-	-	-
BO	-	-	-	-	-
CA	-	-	0.66	85	-
HE	0.52	12	1.13	41	−0.61
HI	-	-	0.51	84	-
LA	0.23	31	-	-	-
LS	0.35	18	0.46	219	−0.11
NO	0.21	16	0.48	104	−0.27
ST	-	-	0.64	120	-
AVE.	−0.42	121.6	0.00	274.2	−0.28
RS80	−0.34	76.3	0.14	215.1	−0.25
RS90	−0.54	186.4	−0.21	367.0	−0.32

Table 5.10: Detailed statistics for bias by separating noon / midnight NOAA-16 satellite overpasses for the entire time period (2001–2003).

Station.	Noon	No.	Midnight	No.	Difference
PL	−1.68	245	0.33	36	−2.01
JO	−1.43	425	−1.09	96	−0.34
JY	-	-	-	-	-
SO	−1.20	241	−0.01	74	−1.19
EK	−1.94	278	0.07	31	−2.01
ES	−1.01	218	0.16	27	−1.17
GR	−1.88	432	−0.63	58	−1.25
IO	−2.33	250	−0.79	42	−1.54
KU	−2.16	293	−0.94	40	−1.22
LI	−1.14	475	0.36	73	−1.50
ME	−1.98	366	−0.95	52	−1.03
MO	−1.98	379	−0.77	72	−1.21
SC	−2.36	400	−1.17	24	−1.19
SS	−1.46	268	−0.13	32	−1.33
BR	−1.97	292	−0.10	98	−1.87
CE	−2.10	106	0.29	40	−2.39
ML	−1.37	204	0.67	61	−2.04
PR	−1.49	202	0.54	63	−2.03
SP	−1.49	124	−0.52	22	−0.97
TB	−1.88	144	0.21	38	−2.09
UC	−1.51	301	0.15	69	−1.66
LE	−1.71	130	−0.03	37	−1.68
LW	−1.66	329	−0.05	69	−1.61
WR	−1.71	97	0.06	52	−1.77
LC	−1.90	31	-	-	-
MB	−3.18	35	−0.16	15	−3.02
MU	−1.81	56	−0.87	25	−0.94
PM	−2.55	43	−0.19	18	−2.36
GL	−1.36	402	−0.81	36	−0.55
LK	−1.87	228	−0.35	39	−1.52
SU	−1.71	320	−0.82	46	−0.89
AB	-	-	-	-	-
BO	−0.59	45	-	-	-
CA	−0.23	60	0.48	12	−0.71
HE	−0.73	116	0.69	21	−1.42
HI	−0.95	37	-	-	-
LA	-	-	-	-	-
LS	−0.46	275	0.39	28	−0.85
NO	−0.44	109	0.64	22	−1.08
ST	−0.17	74	1.44	11	−1.61
AVE.	−1.55	217	−0.11	43.5	−1.47
RS80	−1.47	215.7	−0.16	37.3	−1.37
RS90	−1.69	219.3	−0.04	53.5	−1.64

5.3.3 Summary and Conclusions

The method of comparing satellite and radiosonde humidities developed in Section 5.1.2 was applied to all European radiosonde stations for which data were readily available. The method seems to be useful for monitoring upper tropospheric humidity data from radiosonde stations using microwave satellite data as reference. The stations used in this study launch Vaisala radiosondes which suffer a known dry bias. The results of this study also confirm this dry bias in the radiosonde data. Only the stations from the UK show a near zero or slightly positive bias. There is a large variability in the dry bias among stations and years. There are believed to be several reasons for this such as radiosonde age, difference in calibration and launch procedures (Turner et al., 2003). An apparent difference in bias of about 1 K between NOAA-15 and NOAA-16 was observed. A detailed analysis by separating the matches based on the radiosonde launch time revealed a systematic dry bias in the daytime soundings which was the reason for the difference found between the two satellites. Thus, data from different NOAA satellites were found to be consistent within the limited radiosonde accuracy. This dry bias in the daytime soundings is due to radiation errors and its magnitude is approximately 1.5 K.

6 Summary, Conclusions, and Outlook

This thesis presented the results of several analyses of humidity measurements by microwave humidity sounders and radiosondes. The discussions were mostly focused on the upper troposphere, roughly between 500–200 hPa, due to the importance of this region in the climate system.

The microwave humidity data used in this study are coming from the Advanced Microwave Sounding Unit-B (AMSU-B) instruments onboard the NOAA-15, 16, and 17 satellites. AMSU-B is a five channel microwave radiometer which is designed for measurements of tropospheric humidity. The radiosonde data used in this thesis are from two sources: (1) launches on-board the German research vessel Polarstern of the Alfred Wegener Institute for Polar and Marine Research (AWI) during her 27 expeditions across the poles and (2) routine radiosonde launches at meteorological observatories around the world. The radiative transfer model ARTS was used extensively as a tool for the analysis of these data.

The first chapter introduced the importance of tropospheric water vapor for the Earth's climate and briefly discussed the past and ongoing research activities on this topic. It also gave an overview of the sources of humidity data, examining the merits and demerits on the use of these data sets for upper tropospheric studies.

Chapter 2 examined the variability of the clear-sky outgoing longwave radiation (OLR). At the beginning of this chapter a brief introduction to the modeling of OLR was presented. The main features of the atmospheric data set comprising the radiosonde profiles from Polarstern was also discussed. The sufficient latitudinal and temporal coverage of this data set made it suitable for this study. ARTS

was used to simulate clear-sky OLR fluxes. Based on this study it was found that the global variability in clear-sky OLR is approximately $33\,\mathrm{W\,m^{-2}}$, estimated by the standard deviation of all OLR values calculated from Polarstern radiosondes. This large variability can be explained to a large extent by variations in the effective tropospheric temperature, or in the surface temperature as a proxy. This component of the variability can be removed by making a linear fit of OLR versus surface temperature. The then remaining variability is approximately $8.5\,\mathrm{W\,m^{-2}}$. Of this remaining variability a significant part can be explained by variations in the Total Tropospheric Humidity (TTH). Making a linear fit of the temperature independent OLR variations against the logarithm of TTH reduces the remaining variability to only approximately $3\,\mathrm{W\,m^{-2}}$.

This remaining variability must be due to vertical structure. It was shown that humidity structures on a vertical scale smaller than 4 km contribute a variability of approximately $1\,\mathrm{W\,m^{-2}}$, but no significant bias if the smoothing is done in the right way. The right way to smooth is in relative humidity. If the smoothing is done, for example, in VMR it leads to a substantial bias. This result supports the fact that measurements from sensors with coarse vertical resolution may be used to predict OLR with the correct mean values, but will not be able to fully reproduce the variability due to vertical structure, as almost half of that can come from structures on a scale smaller than 4 km. Therefore measurements by satellite instruments which are sensitive to relative humidity such as AMSU-B or HIRS can be used for climate applications, even though their vertical resolution is low.

Chapter 3 presented the basic radiative transfer (RT) theory, the radiative transfer model ARTS, and the AMSU-B instrument. ARTS is a general purpose RT model which can be used to simulate measurements of any instrument which measures the microwave or thermal infrared radiation. The chapter discussed only a few features of ARTS which are relevant for the simulations of AMSU-B measurements. The details of the AMSU-B instrument like the channel positions, horizontal and vertical resolutions, sensitive altitudes (using the Jacobians), and the features like the limb effect were also discussed in this chapter. The validation of ARTS for AMSU-B measurements by comparing the

simulations with another reference model was also briefly presented in the chapter. The comparison showed a good agreement between the two models.

It was also checked whether the weak ozone lines present in the AMSU-B frequency range have any impact on the measured brightness temperatures. Accurate line-by-line RT calculations were performed using climatological and re-analysis data to check this impact. The results indicated that AMSU-B Channel 18 is the most affected, with brightness temperature differences of about 0.5 K. This is a significant difference, equal to the estimated noise equivalent temperature of this channel on the NOAA-16 satellite (Buehler et al., 2004). The difference was not just an offset, but shows a dependence on the channel brightness temperature, the differences being smaller for colder brightness temperatures and larger for warmer brightness temperatures. Therefore bias correction schemes used in NWP will not be able to successfully eliminate the ozone effect by a constant. Channels 17 and 20 are also marginally affected by the ozone lines. One recommendation of this study was that the ozone lines should be used in RT calculations, thus improving the use of AMSU-B radiances for NWP or climate applications.

Chapter 4 presented a simple method to transform AMSU-B Channel 18 brightness temperature to Upper Tropospheric Humidity (UTH). This method is referred to as brightness temperature transformation method. The method can be used to retrieve Jacobian weighted upper tropospheric humidity (UTH) in a broad layer centered roughly between 6 and 8 km altitude. Retrieval results are sensitive to the type of Jacobian used to define UTH. It was found that the retrieval of UTH based on the fractional water vapor VMR Jacobian works better than the more traditional retrieval of UTH based on the relative humidity Jacobian, and that the new UTH definition does not need a reference pressure in the regression relation.

The UTH bias is always below 4 %RH, where the largest values are found for high humidity cases. The UTH relative bias is always below 20%, where the largest values are found for low humidity cases. The UTH standard deviation is between 2 and 6.5 %RH in absolute numbers, or between 10 and 27% in relative numbers. The standard

deviation is dominated by the regression noise, resulting from vertical structure not accounted for by the simple transformation relation. The part of the UTH error resulting only from radiometric noise scales with the UTH value and has a relative standard deviation of approximately 7% for a radiometric noise level of 1 K. The UTH retrieval performance was shown to be of almost constant quality for all viewing angles and latitudes, except for problems at high latitudes due to surface effects.

A comparison of AMSU UTH and radiosonde UTH for the radiosonde station Lindenberg was used to validate the retrieval method. The agreement is reasonable if known systematic differences between AMSU and radiosonde are taken into account. A qualitative comparison of UTH climatologies from AMSU data and HIRS also showed a good agreement.

The brightness temperature transformation method acts as a tool for interpreting the brightness temperatures in a more intuitive quantity, the relative humidity. A climatology of UTHcan be made in two ways: One is by transforming the averaged brightness temperatures to UTH and the other by averaging the UTH values, obtained by the transformation of each brightness temperature. It is shown by an example using ECMWF reanalysis data that the results of the two methods differ significantly, up to 6 %RH. These differences show a dependence on the standard deviation of the brightness temperatures, that is, the difference increases with the standard deviation.

The investigation with the aid of a simple Monte Carlo approach suggested that these differences are due to the log-normal nature of the UTH distribution due to the occurrence of very cold brightness temperatures. Interestingly, the Monte Carlo approach overestimated the differences compared to those obtained from the ECMWF data. A further investigation with real AMSU-B data showed that this overestimation was due to the assumption of Gaussian distribution for the brightness temperatures in the Monte Carlo method. The differences obtained from the real AMSU data and simulated AMSU data were found to be consistent.

It was demonstrated that the use of a robust estimator, the median, could solve the difference between the two climatologies. As suggested by Lanzante (1996) the use of robust estimators such as the median

could prevent introducing spurious errors in climatologies. Note that several studies use the simple arithmetic mean in UTH climatological studies (Soden and Bretherton, 1993, 1996; Bates and Jackson, 2001; Bates et al., 2001), except the study by Lanzante and Gahrs (2000). A strong recommendation was made for the use of median or other robust estimators over the use of the simple arithmetic mean. Although the discussions were only for UTH, the results may be applicable to the climatological studies in general.

Chapter 5 presented a comparison of humidity measurements by AMSU-B and radiosondes. This chapter has three major sections. The first section outlined the development of the methodology of the comparison and a case study and the second and third sections demonstrated the application of the method to assess the performance of different radiosonde sensors and stations, respectively. A robust method to compare radiosonde humidity data to AMSU data was developed, which is planned to be used for future global studies. The new method has some unique features: Firstly, the comparison is done for a target area, allowing an estimation of the atmospheric variability. Secondly, displacement and cloud filters are applied. Thirdly, a complete and consistent error model is used.

The method was validated by a detailed case study, using the high quality Lindenberg radiosonde data and the NOAA-15 and 16 satellite data for the time period from 2001 to 2002. The study confirmed that low vertical resolution data, as found in operational archives, is sufficient to accurately predict AMSU radiances. However, it also demonstrated that corrections applied in Lindenberg to the standard Vaisala data processing make a significant difference, particularly in the upper troposphere.

Overall, the AMSU data are in very good agreement with the radiosonde data, with the notable exception of a slope in Channel 18. By re-processing with perturbed RT model parameters, RT model error was ruled out as a possible explanation for the slope, leaving only AMSUdata and radiosonde data. Of these two, the latter seem the more likely explanation, which would mean that the corrected Lindenberg radiosonde data has a small residual dry bias at low humidities, giving 0 %RH when the true humidity is still approximately 2–4 %RH.

Furthermore, the impact of the weak ozone lines could not explain the slope in Channel 18. It was also demonstrated that zonal, monthly mean climatological ozone profiles are sufficient to account for the effect of the ozone lines on AMSU-B radiances.

The method was applied to all European radiosonde stations for which data were readily available. The method seems to be useful for monitoring upper tropospheric humidity data from radiosonde stations using microwave satellite data as reference. The stations used in this study launch Vaisala radiosondes which suffer a known dry bias. The results of this study also confirm this dry bias in the radiosonde data. Only the stations from the UK show a near zero or slightly positive bias. There is a large variability in the dry bias among stations and years. There are believed to be several reasons for this such as radiosonde age, difference in calibration and launch procedures (Turner et al., 2003). A systematic difference in bias of about 1 K between NOAA-15 and NOAA-16 was also found, which strongly hints at a systematic difference in brightness temperature measurements of the two satellites.

The results presented in this thesis has paved the way for many interesting future research topics. One topic that is of immediate interest is to create a climatology of UTH based on the long term satellite microwave data available, using the brightness temperature transformation method. A time series of such a data set will be useful to perform trend analysis and also to identify the factors controlling upper tropospheric water vapor. On the other hand, the methodology developed to compare humidity measurements by satellite microwave sounders and radiosondes can be applied to the global radiosonde network. The idea is a long term monitoring of the network using satellite data as benchmark. This method has already been using for the assessment of upper tropospheric humidity in the ECMWF fields. The results from the pilot study of applying the method had shown some inter-satellite differences, this also will be a point for further research.

Acknowledgments

I would like to thank my supervisor Dr. Stefan Alexander Buehler for being an endless source of motivation and energy throughout the course of this work. I gratefully acknowledge his efforts to get me in touch with the subject and programming and for his patience in bearing my dumbness at the early stages of my work. I would like to thank all the former and existing members of the SAT group for providing a good, scientific working environment. Special thanks to Oliver Lemke for his computer and programming related assistance, Mashrab Kuvatov for his valuable contribution to the development of the humidity comparison methodology, Thomas Kuhn for his suggestions and contribution in ARTS and absorption calculations, Arash Houshangpour and Sho Tsujimaru for useful discussions and 'scientific fights', Axel von Engeln and Emmanuel Brocard for discussion and co-operation during the ESA-OLR study, Nathalie Courcoux, Claudia Emde, Mashrab Kuvatov, Christian Melsheimer, and Poornendu Singh for proof-reading different parts of my thesis, and Stefan Buehler and T.R. Sreerekha for proof-reading and giving a lot of constructive comments for the entire thesis. Special thanks to Lothar Meyer-Lerbs for helping me in type setting the thesis.

I also thank Prof. K. Künzi and Prof. J. Notholt for agreeing to review my thesis and for the comments which helped to improve this thesis.

I thank the ARTS community, especially Patrick Eriksson who implemented several routines which are directly related to my work. I acknowledge the co-operation of Carlos Jimenez during the development of the neural net based retrieval of UTH from AMSU data. Thanks also to the British Atmospheric Data Centre (BADC) for giving us access to radiosonde data from stations worldwide. Special thanks to

Lisa Neclos from the Comprehensive Large Array-data Stewardship System (CLASS) of the US National Oceanic and Atmospheric Administration (NOAA) for providing the AMSU data. Thanks to F. Chevallier and N. A. Scott for ECMWF and TIGR-3 data respectively, and to Ulrich Leiterer and Horst Dier from DWD station Lindenberg for their radiosonde data. I also thank Steve English, Nigel Atkinson, Tim Hewison, Roger Saunders, Tony Reale, Brian Soden, and many other scientists who helped me during this work by answering my questions and for providing the pre/re-prints of their articles.

This study was funded by the German Federal Ministry of Education and Research (BMBF), within the AFO2000 project UTH-MOS grant 07ATC04. It is a contribution to COST Action 723 'Data Exploitation and Modeling for the Upper Troposphere and Lower Stratosphere'.

There are many friends who made my journey during the last four years pleasant. Sandip, Lok, Ninad, Aveek, Semeena and Beena are just a few among them. I don't know how to thank Sreerekha for always being a source of encouragement and for her friendship. Regular phone chats with Mathan, Abhilash and Unniannan gave me a lot of enthusiasm in life. I must recall that it is Unniannan who taught me many basic things in physics because of which I could start my Ph.D. study. I also take this opportunity to thank all my teachers for imparting their knowledge. I am especially grateful to Prof. P. V. Joseph who made me enthusiastic about weather and climate.

Finally, but most importantly, I thank my parents and sister for being there as pillars of support and for their wishes and prayers that are sustaining me.

Bibliography

Allan, R. P., Ringer, M. A. and Slingo, A., 2003: Evaluation of moisture in the Hadley Centre climate model using simulations of HIRS water-vapor channel radiances. *Q. J. R. Meteorol. Soc.*, **129**, 3371–3389, doi:10.1256/qj.02.217.

Allan, R. P., Shine, K. P., Slingo, A. and Pamment, J. A., 1999: The dependence of clear-sky outgoing long-wave radiation on surface temperature and relative humidity. *Q. J. R. Meteorol. Soc.*, **125**, 2103–2126, doi:10.1256/smsqj.55 808.

Anderson, G. P., Clough, S. A., Kneizys, F. X., Chetwynd, J. H. and Shettle, E. P., 1986: *AFGL atmospheric constituent profiles (0–120 km)*. Tech. Rep. TR-86-0110, AFGL.

Arrhenius, S., 1896: On the influence of carbonic acid in the air upon the temperature of the ground. *Philos. Mag.*, **41**, 237–276.

Bates, J. J. and Jackson, D. L., 2001: Trends in upper-tropospheric humidity. *Geophys. Res. Lett.*, **28**, 9, 1695–1698.

Bates, J. J., Jackson, D. L., Breon, F.-M. and Bergen, Z. D., 2001: Variability of tropical upper tropospheric humidity 1979–1998. *J. Geophys. Res.*, **106**, D23, 32 271–32 281.

Buehler, S. A. and Courcoux, N., 2003: The impact of temperature errors on perceived humidity supersaturation. *Geophys. Res. Lett.*, **30**, 14, 1759, doi:10.1029/2003GL017 691.

Buehler, S. A., von Engeln, A., Brocard, E., John, V. O., Kuhn, T. and Eriksson, P., 2005a: Recent developments in the line-by-line modeling of outgoing longwave radiation. *J. Quant. Spectrosc. Radiat. Transfer*. Submitted.

Buehler, S. A., Eriksson, P., Haas, W., Koulev, N., Kuhn, T. and Lemke, O., 2003: *ARTS-1-0 User Guide*. University of Bremen.

215 pages, regularly updated versions available at www.sat.uni-bremen.de/arts/.

Buehler, S. A., Eriksson, P., Kuhn, T., von Engeln, A. and Verdes, C., 2005b: ARTS, the Atmospheric Radiative Transfer Simulator. *J. Quant. Spectrosc. Radiat. Transfer*, **91**, 1, 65–93, doi:10.1016/j.jqsrt.2004.05.051.

Buehler, S. A. and John, V. O., 2005: A simple method to relate microwave radiances to upper tropospheric humidity. *J. Geophys. Res.*, **110**, D02 110, doi:10.1029/2004JD005 111.

Buehler, S. A., John, V. O., von Engeln, A., Brocard, E., Kuhn, T. and Eriksson, P., 2005c: Understanding the global variability of clear-sky outgoing longwave radiation. *Q. J. R. Meteorol. Soc.* Submitted.

Buehler, S. A., Kuvatov, M., John, V. O., Leiterer, U. and Dier, H., 2004: Comparison of microwave satellite humidity data and radiosonde profiles: A case study. *J. Geophys. Res.*, **109**, D13 103, doi:10.1029/2004JD004 605.

Burns, B. A., Wu, X. and Diak, G. R., 1997: Effect of precipitation and cloud ice on brightness temperatures in AMSU moisture channels. *IEEE T. Geosci. Remote*, **35**, 6, 1429–1437.

Chaboureau, J.-P., Chedin, A. and Scott, N. A., 1998: Remote sensing of the vertical distribution of atmospheric water vapor from the TOVS observations: Method and validation. *J. Geophys. Res.*, **103**, D8, 8743–8752.

Chamberlin, T. C., 1899: An attempt to frame a working hypothesis of the cause of glacial periods on an atmospheric basis. *J. Geo.*, **7**, 609–621.

Chen, J., Carlson, B. E. and Genio, A. D., 2002: Evidence for strengthening of the tropical general circulation in the 1990s. *Science*, **295**, 838–841.

Chevallier, F., 2001: *Sampled databases of 60-level atmospheric profiles from the ECMWF analysis*. Tech. Rep., ECMWF. EUMETSAT SAF program research report no. 4.

Christy, J. R. and Norris, W. B., 2004: What may we conclude about global tropospheric temperature trends. *Geophys. Res. Lett.*, **31**, L06 211, doi:10.1029/2004GL019 361.

Clough, S. A. and Iacomo, M. J., 1995: Line-by-line calculation of

atmospheric fluxes and cooling rates: Application to carbon dioxide, ozone, methane, nitrous oxide and the halocarbons. *J. Geophys. Res.*, **100**, D8, 16 519–16 535.

Clough, S. A., Iacono, M. J. and Moncet, J.-L., 1992: Line-by-line calculations of atmospheric fluxes and cooling rates: Application to water vapor. *J. Geophys. Res.*, **97**, D14, 15 761–15 785.

Colman, R. A., 2001: On the vertical extent of atmospheric feedbacks. *Clim. Dyn.*, **17**, 391–405.

Edwards, D. P., 1992: *GENLN2: A general line-by-line atmospheric transmittance and radiance model*. Tech. Rep. NCAR/TN367STR, National Center for Atmospheric Research, Boulder, Colorado, Boulder, Colorado.

Elliot, W. P. and Gaffen, D. J., 1991: On the utility of radiosonde humidity archives for climate studies. *Bull. Amer. Met. Soc.*, **72**, 1507–1520.

Ellsaesser, H. W., 1984: The climate effect of CO_2: A different view. *Atmos. Env.*, **18**, 431–434.

Emde, C., Buehler, S. A., Davis, C., Eriksson, P., Sreerekha, T. R. and Teichmann, C., 2004: A polarized discrete ordinate scattering model for simulations of limb and nadir longwave measurements in 1D/3D spherical atmospheres. *J. Geophys. Res.*, **109**, D24, D24 207, doi:10.1029/2004JD005 140.

Engelen, R. J. and Stephens, G. L., 1998: Comparison between TOVS/HIRS and SSM/T-2 derived upper tropospheric humidity. *Bull. Amer. Met. Soc.*, **79**, 12, 2748–2751.

Engelen, R. J. and Stephens, G. L., 1999: Characterization of water-vapor retrievals from TOVS/HIRS and SSM/T-2 measuremets. *Q. J. R. Meteorol. Soc.*, **125**, 331–351.

von Engeln, A., Brocard, E., Buehler, S. A., Eriksson, P., John, V. O. and Kuhn, T., 2004a: *ACE+ climate impact study: Radiation part, executive summary*. Tech. Rep., ESTEC Contract No 17479/03/NL/FF.

von Engeln, A., Brocard, E., Buehler, S. A., Eriksson, P., John, V. O. and Kuhn, T., 2004b: *ACE+ climate impact study: Radiation part, final report*. Tech. Rep., ESTEC Contract No 17479/03/NL/FF.

Escoffier, C., Bates, J. J., Chedin, A., Rossow, W. B. and Schmetz,

J., 2001: Comparison of upper tropospheric humidity retrievels from TOVS and Meteosat. *J. Geophys. Res.*, **106**, 5227–5238.

Fetzer, E., McMillin, L. M., Tobin, D., Aumann, H. H., Gunson, M. R., McMillan, W. W., Hagan, D. E., Hofstadter, M. D., Yoe, J., Whiteman, D. N., Barnes, J. E., Bennartz, R., Vomel, H., Walden, V., Newchurch, M., Minnet, P. J., Atlas, R., Schmidlin, F., Olsen, E. T., Goldberg, M. D., Zhou, S., Ding, H., Smith, W. L. and Revercomb, H., 2003: AIRS/AMSU/HSB validation. *IEEE T. Geosci. Remote*, **41**, 2, 418–431.

Forster, P. M. F. and Collins, M., 2004: Quantifying the water vapor feedback associated with post-Pinatubo global cooling. *Clim. Dyn.*, **23**, 207–214, doi:10.1007/s00 382–004–0431–z.

Garand, L. et al., 2001: Radiance and Jacobian intercomparison of radiative transfer models applied to HIRS and AMSU channels. *J. Geophys. Res.*, **106**, D20, 24 017–24 031.

Gierens, K., Kohlhep, R., Spichtinger, P. and Schroedter-Homscheidt, M., 2004: Ice supersaturation as seen from TOVS. *Atmos. Chem. Phys.*, **4**, 539–547.

Gierens, K., Schumann, U., Helten, M., Smit, H. and Marenco, A., 1999: A distribution law for relative humidity in the upper troposphere and lower stratosphere derived from three years of MOZAIC measurements. *Ann. Geophys.*, **17**, 1218–1226.

Greenwald, T. J. and Christopher, S. A., 2002: Effect of cold clouds on satellite measurements near 183 GHz. *J. Geophys. Res.*, **107**, D13, doi:10.1029/2000JD000258.

Harries, J. E., 1996: The greenhouse Earth: A view from space. *Q. J. R. Meteorol. Soc.*, **122**, 799–818.

Harries, J. E., 1997: Atmospheric radiation and atmospheric humidity. *Q. J. R. Meteorol. Soc.*, **123**, 2173–2186.

Hartmann, D. L., 2002: Tropical surprises. *Science*, **295**, 811–812.

Held, I. M. and Soden, B. J., 2000: Water vapor feedback and global warming. *Annu. Rev. Energy Environ.*, **25**, 441–475.

Houshangpour, A., John, V. O. and Buehler, S. A., 2005: Retrieval of upper tropospheric water vapor and upper tropospheric humidity from AMSU radiances. *Atmos. Chem. Phys.*, **5**, 2019–2028.

Inamdar, A. K., Ramanathan, V. and Loeb, N. G., 2004: Satellite

observations of the water vapor greenhouse effect and column longwave cooling rates: Relative roles of the continuum and vibration-rotation to pure rotation bands. *J. Geophys. Res.*, **109**, D06 104, doi:10.1029/2003JD003 980.

Jackson, D. L. and Bates, J. J., 2001: Upper tropospheric humidity algorithm assessment. *J. Geophys. Res.*, **106**, D23, 32 259–32 270.

Janssen, M. A., 1993: An introduction to the passive microwave remote sensing of atmospheres. In *Atmospheric remote sensing by microwave radiometry*, Janssen, M. A., ed., John Wiley & Sons, Inc., 1–35.

Jimenez, C., Eriksson, P., John, V. O. and Buehler, S. A., 2005: A practical demonstration on AMSU retrieval precision for upper tropospheric humidity by a non-linear multi-channel regression method. *Atmos. Chem. Phys.*, **5**, 451–459.

John, V. O. and Buehler, S. A., 2004a: The impact of ozone lines on AMSU-B radiances. *Geophys. Res. Lett.*, **31**, L21 108, doi:10.1029/2004GL021 214.

John, V. O. and Buehler, S. A., 2004b: Scaling of microwave radiances to layer averaged relative humidity. In *IASTA bulletin, International conference on: aerosols, clouds, and climate.*, vol. 16. ISSN 0971-4510.

John, V. O. and Buehler, S. A., 2005: Comparison of microwave satellite humidity data and radiosonde profiles: A Survey of European stations. *Atmos. Chem. Phys.*, **5**, 1843–1853.

John, V. O., Buehler, S. A. and Courcoux, N., 2005: A cautionary note on the use of Gaussian statistics in satellite based UTH climatologies. *IEEE Geosci. Remote Sens. Lett.* In press.

John, V. O., Buehler, S. A. and Kuvatov, M., 2003: Comparison of AMSU-B brightness temperature with simulated brightness temperature using global radiosonde data. In *Thirteenth International TOVS Study Conference (ITSC - XIII), St. Adele, Montreal, Canada.*

John, V. O., Kuvatov, M. and Buehler, S. A., 2002: ARTS - A new radiative transfer model for AMSU. In *Twelfth International TOVS Study Conference (ITSC - XII), Lorne, Australia.*

Kallberg, P., A.Simmons, Uppala, S. and Fuentes, M., 2004: *The ERA-*

40 Archive. Tech. Rep., ECMWF. ERA-40 Project Report Series No. 17.

Koenig-Langlo, G. and Marx, B., 1997: *Climate and Environmental Database Systems*, chap. 11: The Meteorological Information System at the Alfred Wegener Institute. Kluwer Academic Publisher.

Kuhn, T., 2004: *Atmospheric absorption models for the millimeter wave range*. Ph.D. thesis, University of Bremen.

Kuvatov, M., 2002: *Comparison of simulated radiances from radiosonde data and microwave sounding data for the validation of the forward model for water vapor retrieval*. Master's thesis, Postgraduate Programme Environmental Physics (PEP), University of Bremen.

Lanzante, J. R., 1996: Resistant, robust and non-parametric techniques for the analysis of climate data: theory and examples, including applications to historical radiosonde station data. *Int. J. Climatol.*, **16**, 1197–1226.

Lanzante, J. R. and Gahrs, G. E., 2000: The clear-sky bias of TOVS upper-tropospheric humidity. *J. Clim.*, **13**, 4034–4041.

Leiterer, U., Dier, H. and Naebert, T., 1997: Improvements in radiosonde humidity profiles using RS80/RS90 radiosondes of Vaisala. *Beitr. Phys. Atm.*, **70**, 4, 319–336.

Lesht, B. M. and Richardson, S. J., 2002: The Vaisala RS-80H radiosonde dry-bias correction redux. In *Twelfth ARM science team meeting proceedings, St. Petersburg, Florida, April 8-12*.

Liebe, H. J., 1989: MPM – an atmospheric millimeter–wave propagation model. *Int. J. Inf. Millim. Waves*, **10**, 6, 631–650.

Lindzen, R. S., 1990: Some coolness concerning global warming. *Bull. Amer. Met. Soc.*, **71**, 288–299.

Lorenc, A. C., Barker, D., Bell, R. S., Macpherson, B. and Maycock, A. J., 1996: On the use of radiosonde humidity observations in midlatitude NWP. *Meteorol. Atmos. Phys.*, **60**, 3–17.

Manabe, S. and Wetherald, R. T., 1967: Thermal equilibrium of the atmosphere with a given distribution of relative humidity. *J. Atmos. Sci.*, **24**, 241–259.

Melsheimer, C., Verdes, C., Buehler, S. A., Emde, C., Eriksson, P., Feist, D. G., Ichizawa, S., John, V. O., Kasai, Y., Kopp, G., Koulev,

N., Kuhn, T., Lemke, O., Ochiai, S., Schreier, F., Sreerekha, T. R., Suzuki, M., Takahashi, C., Tsujimaru, S. and Urban, J., 2005: Intercomparison of General Purpose Clear sky atmospheric radiative transfer models for the millimeter/submillimeter spectral range. *Radio Sci.*, RS1007, doi:10.1029/2004RS003 110.

Minschwaner, K. and Dessler, A., 2004: Water vapor feedback in the tropical upper troposphere: Model results and observations. *J. Clim.*, **17**, 1272–1282.

Mo, T., 1996: Prelaunch calibration of the Advanced Microwave Sounding Unit-A for NOAA-K. *IEEE Trans. Micr. Theory Techni.*, **44**, 1460–1469.

Nakamura, H., Seko, H. and Shoji, Y., 2004: Dry biases of humidity measurements from the Vaisala RS80-A and Meisi RS2-91 radiosondes and from ground based GPS. *J. Meteorol. Soc. Japan*, **82**, 277–299.

Peixoto, J. P. and Oort, A. H., 1996: The climatology of relative humidity in the atmosphere. *J. Clim.*, **9**, 3443–3463.

Petty, G. W., 2004: *A First Course in Atmospheric Radiation*. Sundog Publishing, Madison, Wisconsin. ISBN 0-9729033-0-5.

Pickett, H. M., Poynter, R. L. and Cohen, E. A., 1992: *Submillimeter, Millimeter, and Microwave Spectral Line Catalogue*. Tech. Rep. JPL Publication 80–23, Rev. 3, Jet Propulsion Laboratory.

Press, W. H., Teukolsky, S. A., Vetterling, W. T. and Flannery, B. P., 1992: *Numerical Recipes in C*. 2 edn., Cambridge University Press.

Ridgway, W. L., Harshvardhan and Arking, A., 1991: Computation of atmospheric cooling rates by exact and approximate methods. *J. Geophys. Res.*, **96**, D5, 8969–8984.

Rodgers, C. D., 2000: *Inverse methods for atmospheric sounding: theory and practise*, vol. 2 of *Series on atmospheric, oceanic and planetary physics*. 1 edn., World Scientific Publ.

Rosenkranz, P. W., 1993: Absorption of microwaves by atmospheric gases. In *Atmospheric remote sensing by microwave radiometry*, Janssen, M. A., ed., John Wiley & Sons, Inc., ISBN 0-471-62891-3, 37–90, URL ftp://mesa.mit.edu/phil/lbl_rt.

Rosenkranz, P. W., 1995: A rapid atmospheric transmittance algo-

rithm for microwave sounding channels. *IEEE T. Geosci. Remote*, **33**, 1135–1140.

Rosenkranz, P. W., 1998: Water vapor microwave continuum absorption: A comparison of measurements and models. *Radio Sci.*, **33**, 4, 919–928. (correction in 34, 1025, 1999), ftp://mesa.mit.edu/phil/lbl_rt.

Rosenkranz, P. W., 2001: Retrieval of temperature and moisture profiles from AMSU-A and AMSU-B measurements. *IEEE T. Geosci. Remote*, **39**, 11, 2429–2435.

Ross, R. J. and Gaffen, D. J., 1998: Comment on "Widespread tropical drying from 1979 to 1995" by Schroeder and McGuirk. *Geophys. Res. Lett.*, **25**, 4357–4358.

Rothman, L. S., Barbe, A., Benner, D. C., Brown, L. R., Camy-Peyret, C., Carleer, M. R., Chance, K., Clerbaux, C., Dana, V., Devi, V. M., Fayt, A., Flaud, J.-M., Gamache, R. R., Goldman, A., Jacquemart, D., Jucks, K. W., Lafferty, W. J., Mandin, J.-Y., Massie, S. T., Nemtchinov, V., Newnham, D. A., Perrin, A., Rinsland, C. P., Schroeder, J., Smith, K. M., Smith, M. A. H., Tang, K., Toth, R. A., Auwera, J. V., Varanasi, P. and Yoshino, K., 2003: The HITRAN molecular spectroscopic database: Edition of 2000 including updates of 2001. *J. Quant. Spectrosc. Radiat. Transfer*, **82**. HITRAN special issue.

Roy, B., Halverson, J. B. and Wang, J., 2004: The influence of radiosonde age on TRMM field campaign soundings humidity correction. *J. Atmos. Ocean Technol.*, **21**, 470–480.

Salby, M. L., 1996: *Fundamentals of Atmospheric Physics*, vol. 61 of *International Geophysics Series*. Academic Press.

Saunders, R., Marticardi, M. and Brunel, P., 1999: An improved radiative transfer model for assimilation of satellite radiance observations. *Q. J. R. Meteorol. Soc.*, **125**, 1407–1425.

Saunders, R. W., Hewison, T. J., Stringer, S. J. and Atkinson, N. C., 1995: The radiometric characterization of AMSU-B. *IEEE T. Microw. Theory*, **43**, 4, 760–771.

Seidel, D. J., 2002: Water vapor: distribution and trends. In *Encyclopedia of Global Environmental Change*, John Wiley & Sons, Ltd.

Seidel, D. J., Angell, J. K., Christy, J., Free, M., Klein, S. A., Lanzante,

J. R., Mears, C., Parker, D., Shabel, M., Spencer, R., Sterin, A., Thorne, P. and Wentz, F., 2004: Uncertainty in signals of large-scale climate variations in radiosonde and satellite upper-air temperature datasets. *J. Clim.*, **17**, 2225–2240.

Shine, K. P. and Sinha, A., 1991: Sensitivity of the Earth's climate to height-dependent changes in the water vapour mixing ratio. *Nature*, **354**, 382–384.

Sinha, A. and Allen, M. R., 1994: Climate sensitivity and tropical moisture distribution. *J. Geophys. Res.*, **99**, D2, 3707–3716.

Sinha, A. and Harries, J. E., 1995: Water vapor and greenhouse trapping - The role of far-infrared absorption. *J. Geophys. Res.*, **22**, 2147–2150.

Soden, B. J., 1998: Tracking upper tropospheric water vapor radiances: A satellite perspective. *J. Geophys. Res.*, **103**, D14, 17 069–17 081.

Soden, B. J., 2004: The impact of tropical convection and cirrus on upper tropospheric humidity: A Lagrangian analysis of satellite measurements. *Geophys. Res. Lett.*, **31**, 20, L20 104, doi:10.1029/2004 GL020 980.

Soden, B. J. and Bretherton, F. P., 1993: Upper tropospheric relative humidity from the GOES 6.7 μm channel: Method and climatology for July 1987. *J. Geophys. Res.*, **98**, D9, 16 669–16 688.

Soden, B. J. and Bretherton, F. P., 1996: Interpretation of TOVS water vapor radiances in terms of layer-average relative humidities: Method and climatology for the upper, middle, and lower troposphere. *J. Geophys. Res.*, **101**, D5, 9333–9343.

Soden, B. J. and Lanzante, J. R., 1996: An assessment of satellite and radiosonde climatologies of upper-tropospheric water vapor. *J. Clim.*, **9**, 6, 1235–1250.

Soden, B. J., Turner, D. D., Lesht, B. M. and Miloshevich, L. M., 2004: An analysis of satellite, radiosonde, and lidar observations of upper tropospheric water vapor from the Atmospheric Radiation Measurement Program. *J. Geophys. Res.*, **109**, D04 105, doi:10.1029/2003JD003 828.

Soden, B. J., Wetherald, R. T., Stenchikov, G. L. and Robock, A.,

2002: Global cooling after the eruption of Mount Pinatubo: A test of climate feedback by water vapor. *Science*, **296**, 727–730.

Sohn, B. J., Chung, E.-S., Schmetz, J. and Smith, E. A., 2001: Estimating upper-tropospheric water vapor from SSM/T-2 satellite measurements. *J. Appl. Meteorol.*, **42**, 488–504.

Sonntag, D., 1994: Advancements in the field of hygrometry. *Meteorol. Z.*, **3**, 51–66.

Spangenberg, D. A., Mace, G. G., Ackerman, T. P., Seaman, N. L. and Soden, B. J., 1997: Evaluation of model-simulated upper tropospheric humidity using 6.7 µm satellite observations. *J. Geophys. Res.*, **102**, D22, 25 737–25 749.

SPARC, 2000: *Assessment of Upper Tropospheric and Stratospheric Water Vapour*, chap. Conclusions. WCRP-113,WMO/TD-No.1043: World Climate Research Programme, 261–264.

Spencer, R. W. and Braswell, W. D., 1997: How Dry is the Tropical Free Troposphere? Implications for Global Warming Theory. *Bull. Amer. Met. Soc.*, **78**, 6, 1097–1106.

Spichtinger, P., Gierens, K., Leiterer, U. and Dier, H., 2003: Ice supersaturated regions over the station Lindenberg, Germany. *Meteorol. Z.*, **12**, 143–156.

Spichtinger, P., Gierens, K. and Read, W., 2002: The statistical distribution law of relative humidity in the global tropopause region. *Meteorol. Z.*, **11**, 83–88.

Sreerekha, T. R., 2005: *Impact of Clouds on Microwave remote Sensing*. Ph.D. thesis, University of Bremen.

Sreerekha, T. R., Buehler, S. A. and Emde, C., 2002: A simple new radiative transfer model for simulating the effect of cirrus clouds in the microwave spectral region. *J. Quant. Spectrosc. Radiat. Transfer*, **75**, 611–624.

Stocker, T., Clarke, G., Treut, J. L., , Lindsen, R., Meleshko, V., Mugara, R. K., Palmer, T., Pierhhumbert, R., Sellers, P. and Trenberth, K. E., 2001: *IPCC Third Assessment Report - Climate Change 2001: The Scientific Basis*, chap. Physical climate processes and feedbacks. WMO.

Tian, B., Soden, B. J. and Wu, X., 2004: Diurnal cycle of convection, clouds, and water vapor in the tropical upper troposphere: Satellite

versus a general circulation model. *J. Geophys. Res.*, **109**, D10101, doi:10.1029/2003JD004117.

Turner, D. D., Lesht, B. M., Clough, S. A., Liljegren, J. C., Revercomb, H. E. and Tobin, D. C., 2003: Dry bias and variability in Vaisala RS80-H radiosondes: The ARM experience. *J. Atmos. Ocean Technol.*, **20**, 117–132.

Wang, J., Cole, H. L., Carlson, D. J., Miller, E. R., Beierle, K., Paukkunen, A. and Laine, T. K., 2002: Corrections of humidity measurement errors from the Vaisala RS80 radiosonde application to TOGA COARE data. *J. Atmos. Ocean Technol.*, **19**, 981–1002.

Wielicki, B. A., Wong, T., Allan, R. P., Slingo, A., Kiehl, J. T., Soden, B. J., Gordon, C. T., Miller, A. J., Yang, S., Robertson, D. A. R. F., Susskind, J. and Jacobowitz, H., 2002: Evidence for large decadal variability in the tropical mean radiative energy budget. *Science*, **295**, 841–844.

Wilheit, T. T., 1990: An algorith for retrieving water vapor profiles in clear and cloudy atmospheres from 183-GHz radiometric measurements: Simulation studies. *J. Appl. Meteorol.*, **29**, 508–515.